AD-A040 672 PENNSYLVANIA STATE UNIV UNIVERSITY PARK APPLIED RESE--ETC F/G 13/7
THREE DIMENSIONAL INVISCID EFFECTS AND LIMITATIONS OF CASCADE T--ETC(U)
APR 74 A TAMURA N00017-73-C-1418
UNCLASSIFIED TM-74-78 NL

1 OF 2
AD A040672

(2)

(6) THREE DIMENSIONAL INVISCID EFFECTS AND LIMITATIONS OF CASCADE THEORY IN AXIAL FLOW TURBOMACHINERY.

(10) A. Tamura

(9) Master's thesis,

(11) 18 Apr 74

(12) 154 p.

(14) Technical Memorandum
~~File No.~~ TM-74-78
April 18, 1974
(15) ~~Contract No.~~ N00017-73-C-1418

Copy No. 5



The Pennsylvania State University
Institute for Science and Engineering
APPLIED RESEARCH LABORATORY
Post Office Box 30
State College, PA 16801



NAVY DEPARTMENT

NAVAL ORDNANCE SYSTEMS COMMAND



1473

391 007

GB

# ACKNOWLEDGMENTS

The author wishes to express sincere appreciation to his advisor, Dr. B. Lakshminarayana, for his help and counsel during the investigation. The work was sponsored by the Applied Research Laboratory of The Pennsylvania State University which operates under contract with the Naval Ordnance Systems Command. Dr. M. T. Pigott is to be credited for encouraging such a basic research which is so vital in understanding the complex flow phenomena in turbomachinery.

# TABLE OF CONTENTS

TABLE OF CONTENTS (continued)

Page



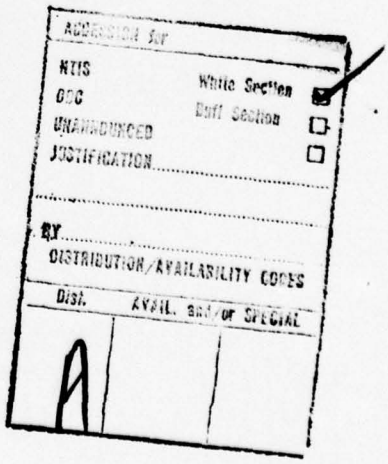

# LIST OF TABLES

# LIST OF FIGURES

LIST OF FIGURES (continued)

LIST OF FIGURES (continued)

LIST OF FIGURES (continued)

LIST OF FIGURES (continued)

LIST OF FIGURES (continued)

# NOMENCLATURE

| | |
|---|---|
| $\nu$ | Hub-to-tip ratio |
| $R_t$ | Radius of the outer casing wall |
| $R_h$ | Radius of the hub |
| $\theta$ | Angular coordinate in a cylindrical coordinate system (rad) |
| $\theta_{i,j}$ | Tangential coordinate of the j-th singular point on i-th blade |
| $\eta$ | Nondimensional radial coordinate normalized by $R_t$ in a cylindrical coordinate system |
| $\eta_{mid}$ | Mid radius = $(1 + \nu)/2$ |
| $\zeta$ | Nondimensional axial coordinate normalized by $R_t$ in a cylindrical coordinate system |
| $\zeta_j$ | Nondimensional axial coordinate of the j-th singular point |
| $\Gamma_j$ | Nondimensional strength of the j-th radial vortex line normalized by $R_t \cdot W_{\zeta m}$ |
| $Q_j(\eta)$ | Nondimensional strength of the j-th radial source line normalized by $R_t \cdot W_{\zeta m}$ |
| $\sigma$ | Strength of the split vortex line |
| $\mu$ | Strength of the split source line |
| $\delta$ | Split vortex and source line distributed over $\lvert\theta\rvert \leq \delta/2$ |
| $\Phi_v$ | Nondimensional velocity potential due to a single radial vortex line or series of radial vortex lines of constant strength normalized by $R_t \cdot W_{\zeta m}$ |
| $\Phi_s$ | Nondimensional velocity potential due to a single radial source line or series of radial source lines of variable strength normalized by $R_t \cdot W_{\zeta m}$ |
| $u_{v\theta}, u_{v\zeta}, u_{v\eta}$ | Nondimensional tangential, radial and axial velocity components due to a single radial vortex line or series of radial vortex lines of constant strength |

NOMENCLATURE (continued)

| | |
|---|---|
| $u_{s\theta}, u_{s\eta}, u_{s\zeta}$ | Nondimensional tangential, radial and axial velocity components due to a single radial source line or series of radial source lines of variable strength |
| $\vec{i}, \vec{j}, \vec{k}$ | Unit vector in $\theta$, $\eta$ and $\zeta$ directions |
| $\vec{u}_v$ | Induced velocity vector due to a series of radial vortex lines of constant strength |
| $\vec{u}_s$ | Induced velocity vector due to a series of radial source lines of variable strength |
| $\vec{W}$ | Three-dimensional cascade mean velocity vector |
| $W_\theta, W_\eta, W_\zeta$ | Tangential, radial and axial components of $\vec{W}$ |
| $W_{\zeta m}$ | $= (W_\zeta)_\eta = 1+\nu/2$ |
| $W_{\theta m}$ | $= (W_\theta)_\eta = 1+\nu/2$ |
| $\alpha_m$ | Cascade mean flow angle |
| $(\alpha_m)_m$ | $= (\alpha_m)_\eta = 1+\nu/2$ |
| $\alpha_i$ | Cascade inlet flow angle |
| $(\alpha_i)_m$ | $= (\alpha_i)_\eta = 1+\nu/2$ |
| $\vec{V}$ | Resultant velocity vector |
| $V_\theta, V_\eta, V_\zeta$ | Tangential, radial and axial components of $\vec{V}$ |
| JVS | Number of singular points per blade |
| NB | Number of blades |
| p | Order of the polynomial for strength of the source Q(j,p) |
| $\lambda$ | Stagger angle |
| $(\lambda)_m$ | $= (\lambda)_\eta = 1+\nu/2$ |
| s | Spacing of the blade row |
| c | Chord length of the blade |
| c/s | Solidity of the blade row |
| $C_p$ | Pressure coefficient |

NOMENCLATURE (continued)

| | |
|---|---|
| $K_{mn}$ | n-th eigen value referred to m-th order Bessel function |
| $J_m(K_{mn}\eta)$ | The first kind Bessel function of m-th order |
| $Y_m(K_{mn}\eta)$ | The second kind Bessel function of m-th order |
| $Z_m(K_{mn},\eta)$ | $= J_m(K_{mn}\eta) \cdot Y_m'(K_{mn}) - J_m'(K_{mn}) \cdot Y_m(K_{mn}\eta)$ |
| $F_v(K_{mn},\nu)$ | $= \int_\nu^1 \eta Z_m(K_{mn}\eta)\, d\eta / \int_\nu^1 \eta\, Z_m^{\,2}(K_{mn}\eta)\, d\eta$ |
| $F_s(K_{mn},\nu,j)$ | $= \int_\nu^1 Q_j(\eta) Z_m(K_{mn}\eta)\, d\eta / \int_\nu^1 \eta Z_m^{\,2}(K_{mn}\eta)\, d\eta$ |

SUBSCRIPTS

| | |
|---|---|
| m | Refer to m-th order Bessel function |
| n | Refer to n-th eigen value for each order of the Bessel function |
| i | Refer to i-th blade |
| j | Refer to j-th singular point for any blade |
| v | Refer to the vortex system |
| s | Refer to the source system |
| $(\,)_m$ | Refer to mid radius |

# CHAPTER I

# INTRODUCTION

## 1.1 Statement of the Problem

Axial-flow-propeller pumps, inducers, or blowers consist of a few blades of high solidity (chord length-to-spacing ratio). The chord length of these blades is comparable to the hub diameter, and the blades usually overlap. As a result of these characteristics and the low hub-to-tip ratio usually encountered in practice, the flow field through such an impeller is three-dimensional. In order to solve this kind of flow field, two-dimensional unrolled potential flow theory (which is two-dimensional potential flow theory adapted to a cylindrical coordinate system) or streamline curvature methods are available. The two-dimensional unrolled solution gives tangential and axial velocity components only. Furthermore, there is no interference effect between each radius, especially hub and tip, since the two-dimensional unrolled solution is applied to each radius independently. Alternatively, the streamline curvature method, which is the most powerful method in the analysis of turbomachinery, is essentially the theory for axisymmetric flow. Thus, it is not suitable for evaluating the local three-dimensional flow field because of the few number of blades. The streamline curvature method is very powerful for obtaining the correlation of inlet and exit flow when the flow field is axisymmetric. To solve the three-dimensional direct problem in turbomachinery (that is, to determine the flow field around a given blade profile) by the relaxation method will be extremely time consuming since the boundary shape is

complicated. Therefore, no proper method exists for the design or analysis of the three-dimensional flow through such an impeller.

## 1.2 Review of Previous Investigation

The basic analysis of the three-dimensional potential flow field in axial flow turbomachinery carried out by Meyer (1) was an extension of Ackeret's idea for two-dimensional potential flow around a cascade. The theoretical model was made up of ring and line vortices to replace the blades and boundary wall.

Tyson (2) showed that the discrepancy between the three-dimensional and the two-dimensional unrolled solutions is large for a radial vortex line spanning an annulus. A single radial vortex line of constant strength spans an annulus bounded by a hub and outer casing wall. The whole flow field except the radial vortex line is irrotational. The basic equation reduces to Laplace's equation and solved with the following boundary conditions (see Figures 1 and 2):

(a) Radial velocity at hub and outer casing wall must vanish.

(b) Axial and radial velocity must vanish at $\zeta = \pm \infty$.

(c) Tangential velocity at $\zeta = \pm \infty$ must be $\pm\Gamma/4\pi\eta$ to satisfy irrotationality.

(d) Boundary conditions were specified by

$$\frac{1}{\eta}\left(\frac{\partial \Phi_v}{\partial \theta}\right)_{\zeta \to \pm o} = \begin{cases} \pm \dfrac{\gamma}{2\eta}, & -\dfrac{\delta}{2} \leq \theta \leq \dfrac{\delta}{2} \\ o, & \dfrac{\delta}{2} < \theta < 2\pi - \dfrac{\delta}{2} \end{cases}$$

The numerical results obtained by Tyson showed 100% difference between the three-dimensional and two-dimensional unrolled solutions in both tangential and axial velocity components at hub and outer casing wall for hub-to-tip ratio $\nu = 0.6$, but they coincided with the two-dimensional solution at mid-radius. However, Etter, Van Dyke and the present author obtained different results. The same calculations showed that the discrepancy between two-dimensional unrolled solution and the three-dimensional solution is less than those calculated by Tyson.

Rossow (3) developed the three-dimensional potential theory for a single radial vortex line of constant strength and a single radial source line of constant strength spanning an annulus. The analysis for the radial vortex line was essentially the same as that of Tyson's, but the results were given in terms of Lommel's function. A solution for a radial source line of constant strength was developed similar to that of the radial vortex.

Etter and Van Dyke (4) calculated the three-dimensional flow field due to a radial vortex line in a cylindrical annulus based on Tyson's analysis. Eigen values and related functions for hub-to-tip ratios $\nu = 0.6$, $0.7$ and $0.8$ were obtained for Bessel functions of orders $m = 1$ to 40, the number of eigen values for each fixed value of m is $n = 1$ to 6. The velocity distribution due to a single radial vortex line of constant strength was different from Tyson's (2), but coincident with the author's results. Example calculations were made for a four-bladed cascade using 6 vortex lines per blade for hub-to-tip ratio $\nu = 0.7$. The discrepancies between the two-dimensional solution and three-dimensional solution were quite small for the mean tangential velocity distribution.

## 1.3 Method and Means of Investigation

The problem is to develop a theory for predicting the three-dimensional potential flow in axial flow turbomachinery. The general objective of the investigation will be to obtain a reliable understanding of the three-dimensional potential flow through axial flow turbomachinery.

The calculation of the three-dimensional potential flow through an impeller is based on the method of distributed singularities. The blades are replaced by a series of line vortices and line sources which have their axes along the radial direction and are arranged along the blade camber surface. The basic perturbed velocity fields due to a single radial vortex line of constant strength and a single radial source line of variable strength along the radial direction were computed from a modified theory based on Tyson's and Rossow's formulations. Since the resultant perturbed flow fields are solutions of the linear Laplace equation and the boundary conditions are homogeneous, these solutions may be superimposed for a series of radial vortex lines and source lines located at arbitrary points. The perturbed flow field due to a single radial vortex line of constant strength was compared with Tyson's and Etter's results for hub-to-tip ratio $\nu = 0.6$. The results are coincident with Etter's but different from Tyson's. The perturbed flow field due to a single radial source line of constant strength shows good agreement with the two-dimensional solution at the mid radius. Eigen values and related functions were calculated for Bessel functions of orders from 0 to 100, the number of eigen values for each order of Bessel function $n = 20$, hub-to-tip ratio $\nu = 0.3, 0.6$. The number of eigen values and the order of the Bessel functions required to obtain enough accuracy increase greatly in the vicinity of the

singular points. Also, for smaller hub-to-tip ratios, more eigen values are required. A computer program to obtain the three-dimensional flow field for an arbitrary number of blades, number of singular points per blade, and singular point locations was developed. Examples exhibiting the interference effects due to hub-to-tip ratio, stagger angle, and number of the blades were carried out. The effects of the radial variation of the strength of the radial source line were also examined.

# CHAPTER II

# THE BASIC THEORY

## 2.1 The Three-Dimensional Flow Field Due to a Single Radial Vortex Line of Constant Strength Spanning an Annulus

In order to carry out a potential flow analysis, the following basic assumptions were made: the flow is inviscid, incompressible and has no heat transfer. A single radial vortex line of constant strength $\Gamma$ spans the annulus region between the hub and outer casing wall (see Figure 1). The theoretical work reported in this section is due to Tyson (2). The whole flow field is irrotational except for the vortex line. The irrotational and continuity conditions are reduced to a Laplace equation in terms of the velocity potential $\Phi_v$ and $\theta$, $\eta$, $\zeta$ (see Figure 1),

$$\nabla^2 \Phi_v = \frac{1}{\eta} \frac{\partial}{\partial \eta} \left(\eta \frac{\partial \Phi_v}{\partial \eta}\right) + \frac{1}{\eta^2} \frac{\partial^2 \Phi_v}{\partial \theta^2} + \frac{\partial^2 \Phi_v}{\partial \zeta^2} = 0 \quad . \tag{1}$$

The boundary conditions are:

a) The axial velocity should vanish at $\zeta = \pm \infty$

$$\left(\frac{\partial \Phi_v}{\partial \zeta}\right)_{\zeta \to \pm\infty} = 0 \tag{2}$$

b) The radial velocity should vanish at hub and outer casing wall.

$$\left(\frac{\partial \Phi_v}{\partial \eta}\right)_{\eta = \nu, 1} = 0 \tag{3}$$

c) The radial velocity should vanish at $\zeta = \pm\infty$.

$$\left(\frac{\partial \Phi_v}{\partial \eta}\right)_{\zeta \to \pm\infty} = 0 \tag{4}$$

d) At plus and minus infinity, the distribution of the tangential velocity must be irrotational. Furthermore, the total magnitude of the circulation must be equal to the strength of the radial vortex line. For convenience, let the magnitude of the circulation around the hub on either side of the vortex line be $\Gamma/2$. These boundary conditions are the same as those of Tyson (Reference 2) but the definition of the positive direction of rotation of the vortex is based on the right-hand screw rule. The corresponding boundary condition of Reference (3) appears different from the above expression, but both are quite true. The only difference is that the initial value of the circulation upstream due to the vortex line is taken to be $-\Gamma/2$ here and zero in Reference 3. The present objective is to determine the perturbed flow field. The above difference of initial circulation may easily be taken into consideration by adjusting the mean flow condition which will be superposed on the above perturbed flow. Circulation about the $\zeta$ axis is $-\Gamma/2$ at $\zeta = +\infty$ and $\Gamma/2$ at $\zeta = -\infty$; then, the tangential velocity at $\zeta = \pm\infty$ is given by the following equations:

$$\frac{1}{\eta}\left(\frac{\partial \Phi_v}{\partial \theta}\right)_{\zeta \to +\infty} = -\frac{\Gamma}{4\pi\eta} \tag{5}$$

and

$$\frac{1}{\eta}\left(\frac{\partial \Phi_v}{\partial \theta}\right)_{\zeta \to -\infty} = \frac{\Gamma}{4\pi\eta} \tag{6}$$

e) The boundary conditions must be specified in the vicinity of the vortex line. The behavior of the tangential velocity close to the singular point ($\zeta$ = 0-plane) is represented by the following expression;

$$\frac{1}{\eta}\left(\frac{\partial \Phi_v}{\partial \theta}\right)_{\zeta \to \pm o} = \begin{cases} \mp \dfrac{\sigma}{2\eta} , & -\dfrac{\gamma}{2} < \theta < \dfrac{\delta}{2} \\ o , & \dfrac{\delta}{2} < \theta < 2\pi - \dfrac{\delta}{2} \end{cases} \quad . \tag{7}$$

Detailed derivation of the specification of the boundary conditions is given in Appendix A. The solution of the Laplace equation is given by the following expression:

$$\Phi_v = \sum_{m=o}^{\infty} (A_m \cos m\theta + B_m \sin m\theta) \sum_{n=1}^{\infty} (C \cdot e^{-K\zeta} + D \cdot e^{K\zeta})(aJ_m(K\eta) + b\, Y_m(K\eta)), \tag{8}$$

where a,b, $A_m$, $B_m$, C, D, K are constants which must be determined, m, n are integer numbers and $J_m$, $Y_m$ are the first and second kind of m-th order Bessel functions. From boundary condition (a), D = 0 when $\zeta > 0$, and C = 0 when $\zeta < 0$. Without loss of generality, C and D can be taken as unity. Using boundary condition (b), substitution of Equation (8) into Equation (3) gives the following conditions:

$$a\, J_m'(K\nu) + b\, Y_m'(K\nu) = 0 \tag{9}$$

and

$$a\, J_m'(K) + b\, Y_m'(K) = 0 \tag{10}$$

where

$$J_m'(K\eta) = \frac{\partial J_m(K\eta)}{\partial \eta} \quad , \quad Y_m'(K\eta) = \frac{\partial Y_m(K\eta)}{\partial \eta} \quad .$$

Combining Equations (9) and (10),

$$\frac{J_m'(K_{mn})}{Y_m'(K_{mn})} = \frac{J_m'(K_{mn}\nu)}{Y_m'(K_{mn}\nu)} \quad . \tag{11}$$

Equation (11) is a relationship between the hub-to-tip ratio $\nu$ and the eigen value $K_{mn}$, where the subscript m refers to the m-th order Bessel function and n is the n-th eigen value for each m, (m = 1,2,3,..., n = 1, 2,3,.... ). Introducing a new expression $Z_m(K_{mn}\eta)$, the last term of Equation (8) is given by the equation,

$$a\, J_m(K_{mn}\eta) + b\, Y_m(K_{mn}\eta) = \frac{a}{Y_m'(K_{mn})}\, Z_m(K_{mn}\eta) , \qquad (12)$$

where

$$Z_m(K_{mn}\eta) = J_m(K_{mn}\eta) \cdot Y_m'(K_{mn}) - J_m'(K_{mn}) \cdot Y_m(K_{mn}\eta). \qquad (13)$$

Therefore, Equation (8) is reduced to the following expression:

$$\Phi_v = \sum_{m=o}^{\infty} (A_m \cos m\theta + B_m \sin m\theta) \sum_{n=1}^{\infty} \exp(\mp K_{mn}\zeta) \frac{a}{Y_m'(K_{mn}\eta)} Z_m(K_{mn}\eta). \qquad (14)$$

The relation $A_m$, $B_m$, and a are determined by the orthogonal characteristics of the trigonometric functions and Bessel function. In order to apply the boundary condition (e), differentiate $\Phi_v$ with respect to $\theta$ and equate it with Equation (7),

$$\left[\frac{1}{\eta} \sum_{m=o}^{\infty} m\,(-A_m \sin m\theta + B_m (\cos m\theta) \sum_{n=1}^{\infty} \frac{a}{Y_m'(K_{mn})} Z_m(K_{mn}\eta)\right]_{\zeta \to \pm o}$$

$$= \begin{cases} \mp \dfrac{\gamma}{2\eta} , & -\dfrac{\delta}{2} < \theta < \dfrac{\delta}{2} \\ o , & \dfrac{\delta}{2} < \theta < 2\pi - \dfrac{\delta}{2} \end{cases} \qquad (15)$$

Multiply both sides by $(\cos m\theta + i \sin m\theta) \cdot \eta^2 Z_m(K_{mn}\eta)$, then integrate from $-\pi$ to $\pi$, and from $\nu$ to 1 for $\eta$:

$$m\pi(B_m - iA_m) \frac{a}{Y_m'(K_{mn})} \int_\nu^1 \eta Z_m^2(K_{mn}\eta)\, d\eta = \mp \frac{\gamma}{m} \sin \frac{m\delta}{2} \int_\nu^1 \eta Z_m(K_{mn}\eta)\, d\eta . \tag{16}$$

Taking the limit $\delta \to 0$, and holding $\delta\gamma = \Gamma$ constant, then,

$$m\pi(B_m - iA_m) \frac{a}{Y_m'(K_{mn})} \int_\nu^1 \eta Z_m^2(K_{mn}\eta)\, d\eta = \mp \frac{\Gamma}{2} \int_\nu^1 \eta Z_m(K_{mn}\eta)\, d\eta . \tag{17}$$

From the imaginary part,

$$A_m = 0 . \tag{18}$$

From the real part,

$$B_m = \frac{\Gamma}{2m\pi} \qquad \text{and} \qquad \frac{a}{Y_m'(K_{mn})} = \frac{\int_\nu^1 \eta Z_m(K_{mn}\eta)\, d\eta}{\int_\nu^1 \eta Z_m^2(K_{mn}\eta)\, d\eta} , \tag{19}$$

where $m = 1, 2, 3, \ldots$ .

Taking into consideration the boundary condition (b), the solution of Laplace Equation (1) is given by Equation (20):

$$\Phi_v = \mp \frac{\Gamma}{4\pi} \left(\theta + 2 \sum_{m=1}^{\infty} \frac{\sin m\theta}{m} \sum_{n=1}^{\infty} \exp(\mp K_{mn}\zeta)\, F_v(K_{mn}, \nu)\, Z_m(K_{mn}\eta)\right), \tag{20}$$

where

$$F_v(K_{mn}, \nu) = \frac{\int_\nu^1 \eta\, Z_m(K_{mn}\eta)\, d\eta}{\int_\nu^1 \eta\, Z_m^2(K_{mn}\eta)\, d\eta} . \tag{21}$$

Therefore, the tangential, radial, and axial velocity components are given by the following expressions:

$$u_{v\theta} = \mp \frac{\Gamma}{4\pi\eta} \left(1 + 2 \sum_{m=1}^{\infty} \cos m\theta \sum_{n=1}^{\infty} \exp(\mp K_{mn}\zeta) \cdot F_v(K_{mn},\nu) \cdot Z_m(K_{mn}\eta)\right), \tag{22}$$

$$u_{v\eta} = \mp \frac{\Gamma}{2\pi} \sum_{m=1}^{\infty} \frac{\sin m\theta}{m} \sum_{n=1}^{\infty} \exp(\mp K_{mn}\zeta) \cdot F_v(K_{mn},\nu) \cdot \frac{\partial Z_m(K_{mn}\eta)}{\partial \eta} \tag{23}$$

and

$$u_{v\zeta} = \pm \frac{\Gamma}{2\pi} \sum_{m=1}^{\infty} \frac{\sin m\theta}{m} \sum_{n=1}^{\infty} K_{mn} \exp(\mp K_{mn}\zeta) \cdot F_v(K_{mn},\nu) \cdot Z_m(K_{mn}\eta) , \tag{24}$$

where the upper and lower signs refer to $+\zeta$ and $-\zeta$ directions respectively.

## 2.2 The Three-Dimensional Flow Field Due to a Single Radial Source Line of Variable Strength Spanning an Annulus

The basic assumptions regarding the flow field (irrotational, inviscid, no heat transfer, and incompressible) are the same as those listed in the previous section. This section is based on Rossow's analysis (Reference 3). The mathematical model of a single radial source line is similar to that of a single radial vortex line except that the radial source line may have a variable strength along the radial direction. In the case of a single radial vortex line, if the strength of the vortex varies in the radial direction, there will be vortices shed according to Helmholtz's law. The flow field is no longer irrotational, but the flow field due to a variable strength radial source line is still irrotational. A single radial source line of variable strength $Q(\eta)$ spans the annulus region between the hub and

outer casing wall (see Figure 1). As in the previous section, the whole flow field is irrotational, and the velocity potential exists, satisfying the Laplace equation. Let the velocity potential due to a single radial source line be $\Phi_s$. Therefore,

$$\frac{1}{\eta}\frac{\partial}{\partial\eta}\left(\eta\frac{\partial\Phi_s}{\partial\eta}\right) + \frac{1}{\eta^2}\frac{\partial^2\Phi_s}{\partial\theta^2} + \frac{\partial^2\Phi_s}{\partial\zeta^2} = 0 \quad . \tag{25}$$

The boundary conditions are:

a) One-half of the mass flow due to a single radial source line goes to $\zeta = +\infty$ and the other half goes to $\zeta = -\infty$. Therefore, from the continuity relationship,

$$\pm\int_{\nu}^{1} Q(\eta)\, d\eta/2 = \left(\frac{\partial\Phi_s}{\partial\zeta}\right)_{\zeta\to\pm\infty} \cdot \pi\,(1-\nu^2) \quad . \tag{26}$$

b) The radial velocity should vanish at hub and outer casing wall,

$$\left(\frac{\partial\Phi_s}{\partial\eta}\right)_{\eta=1,\nu} = 0 \quad . \tag{27}$$

c) The radial velocity should vanish at $\zeta = \pm\infty$,

$$\left(\frac{\partial\Phi_s}{\partial\eta}\right)_{\zeta\to\pm\infty} = 0 \quad . \tag{28}$$

d) The tangential velocity should vanish at $\zeta = \pm\infty$,

$$\frac{1}{\eta}\left(\frac{\partial\Phi_s}{\partial\theta}\right)_{\zeta\to\pm\infty} = 0 \quad . \tag{29}$$

e) The specification of the condition at points close to the single radial source line ($\zeta$ = 0-plane) is given by Equation (30). The detailed derivation is given in Appendix A.

$$\left(\frac{\partial \Phi_s}{\partial \zeta}\right)_{\zeta \to \pm o} = \begin{cases} o \quad , & \frac{\delta}{2} < \theta < 2\pi - \frac{\delta}{2} \\ \mp \frac{\mu(\eta)}{2\eta} \, , & -\frac{\delta}{2} < \theta < \frac{\delta}{2} \end{cases} \quad , \tag{30}$$

where the upper and lower signs refer to $\zeta > 0$ and $\zeta < 0$ respectively. The solution of the Laplace equation under the given boundary conditions is given by the following equation, which is similar to those given in the previous section:

$$\Phi_s = \frac{1}{4\pi} \left( \pm \frac{2}{1-\nu^2} \int_\nu^1 Q(\eta) \, d\eta - \sum_{n=2}^{\infty} \exp(\mp K_{on}\zeta) \cdot \frac{F_s(K_{on},\nu)}{K_{on}} \cdot Z_o(K_{on}\eta) \right.$$

$$\left. -2 \sum_{m=1}^{\infty} \cos m\theta \sum_{n=1}^{\infty} \exp(\mp K_{mn}\zeta) \cdot \frac{F_s(K_{mn},\nu)}{K_{mn}} \cdot Z_m(K_{mn}\eta) \right) \quad , \tag{31}$$

where

$$F_s(K_{mn},\nu) = \frac{\int_\nu^1 Q(\eta) Z_m(K_{mn}\eta) \, d\eta}{\int_\nu^1 \eta \, Z_m^2(K_{mn}\eta) \, d\eta} \quad . \tag{32}$$

The tangential, radial and axial velocity components due to a single radial source line are given by the following expressions,

$$u_{s\theta} = \frac{1}{2\pi\eta} \sum_{m=1}^{\infty} m \sin m\theta \sum_{n=1}^{\infty} \exp(\mp K_{mn}\zeta) \frac{F_s(K_{mn},\nu)}{K_{mn}} \cdot Z_m(K_{mn}\eta) \, , \tag{33}$$

$$u_{s\eta} = -\frac{1}{4\pi}\left(\sum_{n=2}^{\infty} \exp\left(\mp K_{on}\zeta\right) \frac{F_s(K_{on},\nu)}{K_{mn}} \frac{\partial}{\partial\eta} Z_o\left(K_{on}\eta\right) + \right.$$

$$\left. + 2 \sum_{m=1}^{\infty} \cos m\theta \sum_{n=1}^{\infty} \exp\left(\mp K_{mn}\zeta\right) \frac{F_s(K_{mn},\nu)}{K_{mn}} \frac{\partial}{\partial\eta} Z_m(K_{mn}\eta)\right) \qquad (34)$$

and

$$u_{s\zeta} = \frac{1}{4\pi}\left(\pm \frac{2}{1-\nu^2} \int_{\nu}^{1} Q(\eta)\, d\eta \pm \sum_{n=2}^{\infty} \exp\left(\mp K_{on}\zeta\right) F_s(K_{on},\nu) \cdot Z_o(K_{on}\eta) + \right.$$

$$\left. \pm 2 \sum_{m=1}^{\infty} \cos m\theta \sum_{n=1}^{\infty} \exp\left(\mp K_{mn}\zeta\right) F_s\left(K_{mn},\nu\right) \cdot Z_m(K_{mn}\eta)\right) \qquad (35)$$

# CHAPTER III

# APPLICATION OF THE BASIC THEORY

## 3.1 Superposed Flow Field Due to a Series of Radial Vortex and Source Lines Replacing the Blade Row in Axial Turbomachinery

In the preceding paragraph, the three-dimensional perturbed flow field due to a single radial vortex and source line were discussed. These basic solutions will be used to construct a three-dimensional theory to evaluate the potential flow field in a turbomachinery blade row. In general, the three-dimensional flow field around a blade row can be calculated by means of superposition of the three-dimensional cascade mean flow and perturbed flow field. The three-dimensional perturbed flow field is constructed by the superposition of the flow fields due to a series of radial vortex lines of constant strength and source lines of variable strength by which the blades are replaced. This is valid for a free vortex type blade row with any arbitrary blade thickness. The three-dimensional cascade mean flow is similar to the two-dimensional flow, but varying along the radial direction. Also, strictly speaking, the distribution of the cascade mean velocities must be irrotational. Let $\vec{W}$ be a three-dimensional cascade mean velocity observed from the coordinate system fixed to the blade and $W_\theta$, $W_\eta$ and $W_\zeta$ are the components in the $\theta$, $\eta$, $\zeta$ directions respectively. Then, for a free vortex blade row,

$$\eta \cdot W_\theta = \text{constant}, \tag{36}$$

$$W_\eta = 0 \tag{37}$$

and

$$W_\zeta = \text{constant} . \tag{38}$$

However, if the three-dimensional perturbed flow field is small compared to the three-dimensional cascade mean velocity, it seems that the restriction on the cascade mean velocity given by Equation (36) to (38) is not compulsarily needed. All the solutions for the three-dimensional perturbed flow field are solutions of the linear Laplace equation and the boundary conditions are homogeneous. Therefore, mathematically, the method of superposition is valid. Hence, the resultant three-dimensional flow field around a blade row will be determined by the superposition of the three-dimensional cascade mean flow and the perturbed flow due to both radial vortex lines and source lines of known magnitude. Let $\Phi_v$ be the superposed three-dimensional perturbed velocity potential due to a series of radial vortex lines (of constant strength) replacing a row of equally spaced blades (Figure 3)

$$\Phi_v = \mp \sum_{j=1}^{JVS} \frac{\Gamma_j}{4\pi} \sum_{i=1}^{NB} (\theta - \theta_{ij} + 2 \sum_{m=1}^{\infty} \frac{\sin m(\theta - \theta_{ij})}{m} \cdot$$

$$\cdot \sum_{n=1}^{\infty} \exp (\mp K_{mn}(\zeta - \zeta_j)) \cdot F_v(K_{mn},\nu) \cdot Z_m(K_{mn}\eta)) \ , \qquad (39)$$

where NB is the number of blades, $\theta_{ij}$ is the angular coordinate for j-th radial vortex line of the i-th blade, $\zeta_j$ is the axial coordinate of the j-th radial vortex line for any blade, and $\Gamma_j$ is the strength of the j-th vortex line for any blade. Since the blades are equally spaced and have the profile, the distribution of the vortex lines is the same for each blade. Then, the angular coordinate corresponding to j-th vortex line of i-th blade $\theta_{i,j}$ is periodic. Hence,

$$\theta_{ij} = \theta_{1j} + \frac{2\pi}{NB} (i - 1) \ . \qquad (40)$$

Using Equation (40), the summation with respect to i will be eliminated mathematically, and also the summation with respect to m remains only when m is a multiple of the number of the blade NB. Detailed derivation is given in Appendix B. Therefore, Equation (39) is rewritten as follows, neglecting constant terms. For simplicity, let

$$k = \ell \cdot NB \quad . \tag{41}$$

Then,

$$\Phi_v = \pm \frac{NB}{4\pi} \sum_{j=1}^{JVS} \Gamma_j \left(\theta + 2 \sum_{\ell=1}^{\infty} \frac{\sin k\,(\theta - \theta_{1,j})}{k}\right) \cdot$$

$$\cdot \sum_{n=1}^{\infty} \exp\left(\mp K_{kn}\,(\zeta - \zeta_j)\right) \cdot F_v(K_{kn},\nu)\; Z_k(K_{kn}\eta)\Big) \quad . \tag{42}$$

A closed form of the series expression for the other summation has not been found so far, but characteristics of the series expression with respect to the Bessel function is given in Appendix C. The corresponding three-dimensional perturbed flow field due to a series of radial vortex lines of constant strength replacing an equally spaced blade row of NB-blades is given by the following expressions,

$$u_{v\theta} = \mp \frac{NB}{4\pi\eta} \sum_{j=1}^{JVS} \Gamma_j \left(1 + 2 \sum_{\ell=1}^{\infty} \cos k\,(\theta - \theta_{1j})\right) \cdot$$

$$\sum_{n=1}^{\infty} \exp\left(\mp K_{kn}(\zeta - \zeta_j)\right) \cdot F_v(K_{kn},\nu)\; Z_k(K_{kn}\eta)\Big) \quad , \tag{43}$$

$$u_{v\eta} = \mp \frac{NB}{2\pi} \sum_{j=1}^{JVS} \Gamma_j \sum_{\ell=1}^{\infty} \frac{\sin k\,(\theta - \theta_{ij})}{k} \sum_{n=1}^{\infty} \exp\,(\mp K_{kn}(\zeta - \zeta_j))\cdot$$

$$\cdot\, F_v(K_{kn},\nu)\, \frac{\partial Z_k(K_{kn}\eta)}{\partial \eta} \qquad (44)$$

and

$$u_{v\zeta} = \frac{NB}{2\pi} \sum_{j=1}^{JVS} \Gamma_j \sum_{\ell=1}^{\infty} \frac{\sin k\,(\theta - \theta_{1j})}{k} \sum_{n=1}^{\infty} K_{kn} \exp(\pm K_{kn}\,(\zeta - \zeta_j))\cdot$$

$$\cdot\, F_v\,(K_{kn},\nu) \cdot Z_k\,(K_{kn}\eta)\ , \qquad (45)$$

where $u_{v\theta}$, $u_{v\eta}$, $u_{v\zeta}$ are velocity components in the directions $\theta$, $\eta$, and $\zeta$ respectively, and the upper and lower signs refer to $\zeta - \zeta_j > 0$ and $\zeta - \zeta_j < 0$. These expressions are similar to Equations (33) to (35) valid for a single element, except for the fact that one of the summations is over k, which is always a multiple of NB in each of m. It is clear that the analysis given in Appendix B greatly reduces computation time.

Similarly, the superposed three-dimensional perturbed velocity potential due to a series of radial source lines of variable strength replacing the equally spaced blade row of NB-blades is given by Equation (46):

$$\Phi_s = \frac{1}{4\pi} \sum_{j=1}^{JVS} \sum_{j=1}^{NB} \left( \pm \frac{2(\zeta - \zeta_j)}{1 - \nu^2} \int_{\nu}^{1} Q_j(\eta)\, d\eta - \right.$$

$$- \sum_{n=2}^{\infty} \exp\left(\mp K_{on}(\zeta - \zeta_j)\right) \frac{F_s(K_{on},\nu,j)}{K_{on}} Z_o(K_{on}\eta)$$

$$\left. - 2 \sum_{m=1}^{\infty} \cos m(\theta - \theta_{ij}) \sum_{n=1}^{\infty} \exp\left(\mp K_{mn}(\zeta - \zeta_j)\right) \frac{F_s(K_{mn},\nu,j)}{K_{mn}} Z_m(K_{mn}\eta) \right). \tag{46}$$

Taking advantage of the characteristics of the equally spaced blade row, as shown in Appendix B, the summation with respect to i is eliminated. Also, the summation with respect to m remains only when m is a multiple of the blade number NB, then,

$$\Phi_s = \frac{NB}{4\pi} \sum_{j=1}^{JVS} \left( \pm \frac{2(\zeta-\zeta_j)}{1 - \nu^2} \int_{\nu}^{1} Q_j(\eta)\, d\eta - \right.$$

$$- \sum_{n=2}^{\infty} \exp\left(\mp K_{on}(\zeta - \zeta_j)\right) \frac{F_s(K_{on},\nu,j)}{K_{on}} Z_o(K_{on}\eta)$$

$$\left. - 2 \sum_{\ell=1}^{\infty} \cos k(\theta - \theta_{1j}) \sum_{n=1}^{\infty} \exp\left(\mp K_{kn}(\zeta - \zeta_j)\right) \frac{F_s(K_{kn},\nu,j)}{K_{kn}} Z_k(K_{kn}\eta) \right). \tag{47}$$

Again, a closed form of the series expression for the other summation has not been found so far. The corresponding three-dimensional perturbed flow field due to a series of radial source lines of variable strength replacing the equally spaced blade row of NB-blades is given by the following Equations. The upper and lower signs refer to $\zeta - \zeta_j > 0$ and $\zeta - \zeta_j < 0$ respectively.

$$u_{s\theta} = \mp \frac{NB}{2\pi\eta} \sum_{j=1}^{JVS} \sum_{\ell=1}^{\infty} k \sin k\,(\theta - \theta_{1j})$$

$$\sum_{n=1}^{\infty} \exp\,(\mp K_{kn}(\zeta - \zeta_j)) \quad \frac{F_s(K_{kn},\nu,j)}{K_{kn}} \quad Z_k\,(K_{kn}\eta)\ , \tag{48}$$

$$u_{s\eta} = -\frac{NB}{4\pi} \sum_{j=1}^{JVS} \Bigg( \sum_{n=2}^{\infty} \exp(\mp K_{on}(\zeta-\zeta_j)) \quad \frac{F_s(K_{on},\nu,j)}{K_{on}} \quad \frac{\partial Z_o(K_{on}\eta)}{\partial\eta} \quad +$$

$$+ 2 \sum_{\ell=1}^{\infty} \cos k\,(\theta-\theta_{1j}) \sum_{n=1}^{\infty} \exp\,(\mp K_{kn}(\zeta-\zeta_j)) \quad \frac{F_s(K_{kn},\nu,j)}{K_{kn}} \quad \frac{\partial Z_k(K_{kn}\eta)}{\partial\eta} \Bigg) \tag{49}$$

and

$$u_{s\zeta} = \frac{NB}{4\pi} \sum_{j=1}^{JVS} \Bigg( \pm \frac{2}{1-\nu^2} \int_{\nu}^{1} Q_j(\eta)\, d\eta \pm$$

$$\sum_{n=2}^{\infty} \exp\,(\mp K_{on}(\zeta-\zeta_j)) \quad F_s(K_{on},\nu,j) \quad Z_o(K_{on}\eta)$$

$$\pm \quad 2 \sum_{\ell=1}^{\infty} \cos k(\theta-\theta_{1j}) \sum_{n=1}^{\infty} \exp\,(\mp K_{kn}(\zeta-\zeta_j)) \quad F_s(K_{kn},\nu,j) \quad Z_k(K_{kn}\eta)) \Bigg), \tag{50}$$

where $u_{s\theta}$, $u_{s\eta}$, $u_{s\zeta}$ are velocity components in the directions $\theta$, $\eta$, and $\zeta$ respectively, and $k = \ell$ NB.

## 3.2 Direct Problem in Axial Turbomachinery

The direct problem in turbomachinery is to determine the flow field around a given blade profile. The objective of this section is to provide a theoretical formula for the solution of the three-dimensional direct problem in axial turbomachinery. In the distributed

singularity method, the strength of the distributed vortices and sources, and the cascade mean velocity are not known, but the configuration of the blade, inlet flow angle, stagger angle and spacing are given. Therefore, the strength of the singularities must be determined for the given blade geometry, spacing, stagger angle and inlet flow angle. The present method is valid only for a free vortex type blade row with approximately radial elements. Such a blade row will be replaced by a series of radial vortex lines of constant strength and a series of radial source lines of variable strength. Furthermore, the resultant flow field should be irrotational with respect to the coordinate system in which the blade row is fixed. All the flow quantities are measured with reference to this coordinate system. The velocities are normalized by the axial component of the three-dimensional cascade mean velocity $(W_{\zeta m})$ at mid radius between hub and outer casing wall.

The blade system can be represented by:

a) The blade system has NB blades and each blade is replaced by JVS radial vortex lines and source lines respectively.

b) Each vortex line is radial and of constant strength along the radial direction, and the strength of the j-th vortex line for each blade is given by $\Gamma_j$.

c) Each source line is radial and of variable strength along the radial direction. The strength of the j-th source line for each blade is represented by a p-th order polynomial given,

$$Q_j(\eta) = A_{j,0} + A_{j,1}\ \eta + - - - - - - + A_{j,p}\ \eta^p \ . \tag{51}$$

d) For convenience, the j-th vortex line and j-th source line are placed at the same location.

Similar to the two-dimensional solution of the direct problem by the distributed singularity method, the flow field due to a series of vortex and source lines must satisfy the kinematic condition, the closure condition for the source distribution, and the Kutta condition. First, a detailed discussion of the resultant velocity and the cascade mean velocity in the three-dimensional flow is made. Let $\vec{V}$ be a nondimensional resultant velocity vector; then,

$$\vec{V} = \vec{u}_v + \vec{u}_s + \vec{W} \quad , \tag{52}$$

where $\vec{u}_v$, $\vec{u}_s$ are the perturbed velocities due to a series of radial vortex lines and a series of radial source lines respectively, and $\vec{W}$ is the cascade mean velocity. Let i, j, k be unit vectors in the $\theta$, $\eta$, $\zeta$ directions respectively. Then,

$$\vec{u}_v = \vec{i} \cdot u_{v\theta} + \vec{j} \cdot u_{v\eta} + \vec{k} \cdot u_{v\zeta} \quad , \tag{53}$$

$$\vec{u}_s = \vec{i} \cdot u_{s\theta} + \vec{j} \cdot u_{s\eta} + \vec{k} \cdot u_{s\zeta} \tag{54}$$

and

$$\vec{W} = \vec{i} \cdot W_\theta + \vec{j} \cdot W_\eta + \vec{k} \cdot W_\zeta \quad , \tag{55}$$

where $u_{v\theta}$, $u_{v\eta}$, $u_{v\zeta}$ are the $\theta$, $\eta$, $\zeta$ components of $\vec{u}_v$. Similarly, $u_{s\theta}$, $u_{s\eta}$, $u_{s\zeta}$ are the $\theta$, $\eta$, $\zeta$ components of $\vec{u}_s$, and $W_\theta$, $W_\eta$, $W_\zeta$ are the $\theta$, $\eta$, $\zeta$ components of $\vec{W}$. As described in Section (3.1), the cascade mean velocity in the three-dimensional case has only tangential and axial components, and must satisfy the relation given by Equation (36), (37), and (38) in Section (3.1). Therefore, the tangential component of the cascade mean velocity at radius $\eta$ is given by the following equation:

$$W_\theta = \frac{\eta_m}{\eta} \quad W_{\theta m} \quad , \tag{56}$$

where $\eta_m = 1+\nu/2$, and $W_{\theta m}$ is the tangential component of the cascade mean velocity at mid radius between hub and outer casing wall. The axial component of the cascade mean velocity $W_\zeta$ must be constant everywhere, and the radial component $W_\eta$ must be zero everywhere. Then,

$$W_\zeta = W_{\zeta m} = 1 \tag{57}$$

and

$$W_\eta = 0 \ , \tag{58}$$

where $W_{\zeta m}$ is the axial component of the cascade mean velocity at mid radius. On each cylindrical surface of radius $\eta$, we can define the cascade mean flow angle as similar to the cascade mean velocity. Let $(\alpha_i)_m$, $(\Delta V_\theta)_m$ and $(\alpha_m)_m$ be respectively the cascade inlet flow angle at mid radius, the tangential velocity change at the exit at the mid radius and the cascade mean flow angle at the mid radius. Similar to the two-dimensional cascade theory,

$$\tan (\alpha_i)_m = \frac{W_{\theta m} + (\Delta V_\theta)_m}{W_{\zeta m}}$$

$$= \tan (\alpha_m)_m + \frac{(\Delta V_\theta)_m}{W_{\zeta m}} \ , \tag{59}$$

and also

$$2 \cdot s \cdot (\Delta V_\theta)_m = - \Gamma_t \ , \tag{60}$$

where s is the spacing and $\Gamma_t$ is the circulation along a circuit on the cylindrical surface at mid radius $\eta_m = 1+\nu/2$ (see Figure 2 and Figure 4),

$$s = 2\pi\eta_m / NB \tag{61}$$

and

$$\Gamma_t = \sum_{j=1}^{JVS} \Gamma_j \ . \tag{62}$$

Therefore, substituting Equation (60) into (59), we get

$$\tan (\alpha_m)_m = \tan (\alpha_i)_m + \Gamma_t/2 \cdot s \cdot W_{\zeta m} \quad . \tag{63}$$

In Equation (63), $(\alpha_i)_m$ is given and $W_{\zeta m} = 1$ since all the velocities are normalized by this velocity component. Then, $\tan (\alpha_m)_m$ is simply the linear equation of $\Gamma_t$. From the velocity triangle (see Figure 4), we get

$$W_{\theta m} = W_{\zeta m} \cdot \tan (\alpha_m)_m$$

$$= \tan (\alpha_m)_m \quad . \tag{64}$$

Then, Equation (56) is rewritten as

$$W_\theta = 1+\nu/2\eta \cdot \tan (\alpha_m)_m \tag{65}$$

and also from the definition,

$$W_\eta = 0 \tag{66}$$

and

$$W_\zeta = W_{\zeta m} = 1 \quad . \tag{67}$$

Then, the components of the cascade mean velocity at any radius are represented in terms of the cascade mean flow angle at mid radius (Equations (65), (66), and (67)). Therefore, the components of the resultant velocity vector $\vec{V}$ given in Equation (52) are rewritten as

$$V_\theta = u_{v\theta} + u_{s\theta} + 1+\nu/2\eta \quad \tan (\alpha_m)_m \quad , \tag{68}$$

$$V_\eta = u_{v\eta} + u_{s\eta} \tag{69}$$

and

$$V_\zeta = u_{v\zeta} + u_{s\zeta} + 1 \quad . \tag{70}$$

For representing the blade surface, it is convenient to define two planes such that one is flat and perpendicular to the axial axis $\zeta$ and the other is a cylindrical plane of radius $\eta$. These are designated as the $\zeta$-constant-plane and the $\eta$-constant-plane respectively. As shown in Figure 5a and 5b, let $\alpha$ be the angle between the $\zeta$-direction and the line $\overline{AB}$ tangential to the blade surface at point P on the $\eta$ constant plane, and $\beta$ be the angle between the radial line and the tangential line $\overline{CD}$ at a point P on the $\zeta$- constant plane. The components of the unit normal vector $\vec{n}$ at a point P on the blade surface are $n_\theta$, $n_\eta$ and $n_\zeta$ in $\theta$, $\eta$ and $\zeta$ directions respectively. Then,

$$\vec{n} = \vec{i} \cdot n_\theta + \vec{j} \cdot n_\eta + \vec{k} \cdot n_\zeta \quad , \tag{71}$$

where

$$n_\theta = \cos \beta \cos \alpha \, , \tag{72}$$

$$n_\eta = \sin \beta \cos \alpha \, , \tag{73}$$

and

$$n_\zeta = \cos \beta \sin \alpha \quad . \tag{74}$$

Kinematic Condition:

The kinematic condition is that the resultant velocity vector must be perpendicular to the vector $\vec{n}$. Then,

$$\vec{n} \cdot \vec{V} = 0 \quad . \tag{75}$$

Substituting Equations (68) to (74) into (75), the kinematic condition is then given by Equation:

$$\cos\beta\cos\alpha\,(u_{v\theta} + u_{s\theta} + 1+\nu/2\eta\,\tan\,(\alpha_m)_m)$$

$$+ \sin\beta\cos\alpha\cdot(u_{v\eta} + u_{s\eta}) + \cos\beta\sin\alpha\cdot(u_{v\zeta} + u_{s\zeta} + 1) = 0, \tag{76}$$

where $\alpha$, $\beta$ are given by the blade geometry, and $u_{v\theta}$, $u_{v\eta}$, and $u_{v\zeta}$ include $\Gamma_1$ to $\Gamma_{JVS}$ as unknown linear constants to be determined. Also, $u_{s\theta}$, $u_{s\eta}$, and $u_{s\zeta}$ include $A_{1,1}$, $A_{1,2}$, $A_{1,3}$ . . . . . , $A_{1,p}$, $A_{2,1}$, $A_{2,2}$, . . . . . , $A_{2,p}$, . . . . . , $A_{JVS,1}$, $A_{JVS,2}$, . . . . . , $A_{JVS,p}$ as linear constants to be determined. The term $\tan\,(\alpha_m)_m$ includes $\Gamma_1$, $\Gamma_2$, . . . . , $\Gamma_{JVS}$ as linear constants given in Equation (63).

Closure Condition:

The total source strength replacing the blade row must be zero, i.e.,

$$\sum_{j=1}^{JVS} \int_{\nu}^{1} Q_j(\eta)\,d\eta = \sum_{j=1}^{JVS} \int_{\nu}^{1} \left(\sum_{\ell=0}^{p} A_{j,\ell}\eta^{\ell}\right) d\eta = 0 \tag{77}$$

which can be simplified to

$$\sum_{j=1}^{JVS} \sum_{\ell=0}^{p} A_{j,\ell}\,\frac{1-\nu^{\ell+1}}{1+\ell} = 0 \tag{78}$$

Kutta Condition:

In potential flow theory, the circulation around a given blade profile is not unique without the Kutta condition even if the kinematic condition is satisfied. Therefore, to apply potential flow theory to the actual flow around a blade profile, a restriction on the distribution of the vortices is required based on the Kutta-Joukowski hypothesis.

The Kutta-Joukowski hypothesis states that the velocity must be finite at the trailing edge. In the distributed singularity method, the strength of the vortices at the trailing edge must vanish to satisfy the Kutta-Joukowski condition. In the three-dimensional direct problem, the intersections of the blade and $\eta$-constant plane gives a three-dimensional contour. However, the radial component of the resultant velocity is always normal to the plane of this contour. Then, this contour is specified by only the axial and tangential components of the resultant velocity and the vortex lines are all radial; then the circulation around these contours at any radius is always equal to $\Gamma_t$, and the three-dimensional Kutta-Joukowski condition is reduced to that for each contour at each radius. In Figure 6, let points A and B be very close to the trailing edge T on the $\eta$-constant plane. $\vec{V}_A$, $\vec{V}_b$ are the projections of the resultant velocity $\vec{V}$ on the $\eta$-constant plane at points A and B respectively. $V_{A\zeta}$ and $V_{A\theta}$ are axial and tangential components of $\vec{V}_A$. Similarly, $V_{B\zeta}$ and $V_{B\theta}$ are axial and tangential components of $\vec{V}_B$. Then, the Kutta-Joukowski condition is that $\vec{V}_A$ and $\vec{V}_B$ should be of the same magnitude and go towards T for a sharp trailing edge. Then,

$$V_{A\zeta} \cos \varepsilon + V_{A\theta} \sin \varepsilon = V_{B\zeta} \cos \omega + V_{B\theta} \sin \omega \quad , \tag{79}$$

where $\varepsilon$ and $\omega$ are given from the blade geometry. Equation (79) includes $\Gamma_j$ and $A_{j,\ell}$ (j=1 to JVS, and $\ell$=0 to p) as linear constants. Now, the kinematic condition, closure condition, and the Kutta-Joukowski condition are linear first order equations concerned with the unknown constants $\Gamma_j$ and $A_{j,\ell}$ (j=1 to JVS, and $\ell$=0 to p). The number of unknowns is JVS $\cdot$ (p + 2). Therefore, if JVS $\cdot$ (p + 2) - p blade

points are given for the kinematic condition, together with one closure condition and the (p + 1) Kutta-Joukowski condition for (p + 1) $\eta$-constant-plane, the equations become simultaneous first order equations with JVS • (p + 2)-unknowns. Hence, the strength of the vortex lines and source lines can be determined by solving the simultaneous equations. The velocity components are determined by Equations (52) to (55) using Equations (43) to (45) and (48) to (50). Also, the pressure coefficients are given by the following expressions:

$$(C_p)_W = 1 - \frac{|\vec{V}|^2}{|\vec{W}|^2} \tag{80}$$

and

$$(C_p)_{W_m} = 1 - \frac{|\vec{V}|^2}{|\vec{W}|^2} \quad , \tag{81}$$

where $(C_p)_W$ and $(C_p)_{W_m}$ are the pressure coefficients with respect to the cascade mean velocity at radius $\eta$ and the cascade mean velocity at mid radius respectively.

# CHAPTER IV

# NUMERICAL TECHNIQUE AND SOLUTIONS

## 4.1 Determining of Eigen Values and Related Functions

The three-dimensional flow field due to radial vortex lines and source lines given in Equations (22) to (24), (33) to (35), (43) to (45) and (48) to (50) includes an infinite number of eigen values $K_{m,n}$ and related functions $F_v(K_{m,n},\nu)$, $F_s(K_{m,n},\nu,j)$, $Z_m(K_{m,n}\eta)$ and $\partial/\partial\eta\ Z_m(K_{m,n}\eta)$. These eigen values are determined by Equation (11), and are the same both in the radial vortex system and radial source line system since the boundary condition with respect to the radial velocity at the hub and the outer casing wall is the same. However, the eigen values related to the 0-th order Bessel function has meaning only for the source system. The first three eigen values for each order of Bessel function were found step by step and other approximate eigen values were found by extrapolation. All eigen values are improved to obtain higher accuracy by successive iteration up to $10^{-9}$. The eigen values were obtained for Bessel functions of order m = 0 to 100, and the number of eigen values n = 1 to 20 for each order m for hub-to-tip ratios $\nu$ = 0.3 and 0.6 (see Figure 7, 8). The eigen values in Reference (4) are combined with the present $K_{m,n}$ by the following expression:

$$\mu_{m,n} = \nu \cdot K_{m,n} \quad .$$

Now, the related functions $F_v(K_{m,n},\nu)$ and $F_s(K_{m,n},\nu,j)$ are again given by

$$F_v(K_{mn},\nu) = \frac{\int_\nu^1 \eta Z_m(K_{mn}\eta)\, d\eta}{\int_\nu^1 \eta Z_m^{\,2}(K_{mn}\eta)\, d\eta} \qquad (82)$$

$$F_s(K_{m,n},\nu,j) = \frac{\int_\nu^1 Q_j(\eta)\ Z_m(K_{m,n}\eta)\ d\eta}{\int_\nu^1 \eta \cdot Z_m{}^2(K_{m,n}\eta)\ d\eta} \quad , \tag{83}$$

where $Q_j(\eta)$ is the p-th order polynomial given in Equation (51). Then, the numerators of Equations (82) and (83) were resolved into $\int_\nu^1 \eta^p Z_m(K_{m,n}\eta)\ d\eta$ (p = 0 to 3) and calculated by the Gaussion quadrature formula to order 29 for each eigen value (Reference 5), which is a more accurate numerical integral formula than the trapezoidal or Simpson's formula for the same number of points. The denominators of Equations (82) and (83) were calculated by integral formula for Bessel function for each eigen value. Calculation of $Z_m(K_{m,n}\eta)$ and $\partial/\partial\eta$ $Z_m(K_{m,n}\eta)$ is very time consuming. Therefore, nine radial coordinates are selected from the values calculated by the Gaussian quadrature abscissae and $\eta = \nu, 1$. The radial coordinates for which all related functions and necessary Bessel functions are prepared are given in Tables 1, 2, and 3.

Table 1. Radial Coordinates Used for Computation.

| k | 1 | 2 | 3 | 4 | 5 | 6 | 7 | 8 | 9 |
|---|---|---|---|---|---|---|---|---|---|
| $\eta_k$ | $\nu$ | $f(x_7)$ | $f(x_{10})$ | $f(x_{13})$ | $(1+\nu)/2$ | $f(x_{17})$ | $f(x_{20})$ | $f(x_{23})$ | 1.0 |

where

$$f(x_i) = ((1+\nu+(1-\nu)\cdot x_i)/2.0 \tag{84}$$

and

$$x_7 = -x_{23} = -0.7524629$$

$$x_{10} = -x_{20} = -0.5075930 \qquad (85)$$

$$x_{13} = -x_{17} = -0.2113523$$

These correspond to the i-th Gaussion abscissa of order 29. The values for $\nu = 0.6$ and $0.3$ are tabulated in Table 2 and 3 respectively.

Table 2. Radial Coordinates Used for Computation ($\nu = 0.6$).

| k | 1 | 2 | 3 | 4 | 5 | 6 | 7 | 8 | 9 |
|---|---|---|---|---|---|---|---|---|---|
| $\eta_k$ | 0.60000 | 0.64951 | 0.69848 | 0.75773 | 0.80000 | 0.84227 | 0.90152 | 0.95049 | 1.00000 |

Table 3. Radial Coordinates Used for Computation ($\nu = 0.3$).

| k | 1 | 2 | 3 | 4 | 5 | 6 | 7 | 8 | 9 |
|---|---|---|---|---|---|---|---|---|---|
| $\eta_k$ | 0.30000 | 0.38664 | 0.47234 | 0.57603 | 0.65000 | 0.72397 | 0.82766 | 0.91336 | 1.00000 |

The values $Z_m(K_{m,n}\eta)$ for the above mentioned radial coordinates are already calculated in the process of evaluating the numerical integral $\int_\nu^1 \eta^p Z_m(K_{m,n}\eta)\, d\eta$ and also the values of $\partial/\partial\eta \; Z_m(K_{m,n}\eta)$ were calculated by known values using the recurrence formula for the Bessel function. To avoid duplicate calculation of the Bessel function in the main program, all eigen values and related functions were stored on a magnetic tape for m = 0 to 100, n = 1 to 20, $\nu = 0.3$ and $0.6$ for the radial coordinates given in Tables 2 and 3. Then, the computer program for the three-dimensional potential flow field due to an arbitrary series of radial vortex lines of constant strength and a series of

radial source lines of variable strength can be used for hub-to-tip ratios $\nu = 0.3$ and $0.6$ (see Reference 6). Furthermore, if the eigen values and related functions are obtained in a similar manner for any other hub-to-tip ratio, the above computer program is valid for that hub-to-tip ratio as well. The computer programs for the determination of the eigen values and related Bessel functions are given in Reference 6.

## 4.2 Numerical Calculation of the Three-Dimensional Perturbed Flow Field

### 4.2.1 Convergency of the Solution of the Three-Dimensional Perturbed Flow Field

The three-dimensional perturbed flow field due to a series of radial vortex lines of constant strength and a series of radial source lines of variable strength given by Equations (43) to (45) and (48) to (50) include an infinite number of summations with respect to m and n. In order to examine the convergency of the series expressions, a single radial vortex line of strength unity located at $\zeta = 0$, $\theta = 0^{o}$ and a single radial source line of strength unity located at the same point were examined for $\nu = 0.6$ separately. The contributions of m and n to the convergency of the tangential velocity at $\zeta = 0.05$, $0.1$, $0.2$ and $\theta = 30^{o}$ for $\eta = 0.8$ due to a single radial vortex line are shown in Figure 9. The corresponding graphs for a single radial source line are plotted in Figure 10. It is clear that the convergency of the series expression strongly depends on m, not on n. For hub-to-tip ratio $\nu = 0.6$, the required order of Bessel function m is approximately $m > 60$ for $|\zeta| < 0.1$, $m > 20$ for $|\zeta| > 0.2$ and $n = 6$ is enough in any case. Therefore, these results suggest that the summation based on

only n = 1 for each m will give a good result for large $|\zeta|$ if m is taken large enough. However, the convergency becomes poor at points close to the singular point $|\zeta|<0.05$ for $\nu = 0.6$ even if m is taken up to 100. This situation is more severe in the case of smaller hub-to-tip ratio. It seems the smaller the hub-to-tip ratio is, the more the eigen values are required. Mathematically, the three-dimensional tangential velocity components due to a vortex line and the axial velocity component due to a source line located at $\zeta = 0$ and $\theta = 0^{o}$ must vanish at $\zeta = 0$ for any $\theta$ except $\theta = 0^{o}$ for any hub-to-tip ratio. Therefore, taking advantage of these characteristics of the series expression, some improvement to avoid the above difficulties can be made by further analytical considerations described in Appendix D. This approach will be pursued later.

### 4.2.2 Three Dimensional Perturbed Flow Field Due to a Single Radial Vortex Line of Strength Unity and Its Comparison with the Two-Dimensional Solution

The three-dimensional perturbed velocity components due to a single radial vortex line of strength unity located at $\zeta_1 = 0$ and $\theta_{1,1} = 0^{o}$ were calculated by Equations (43) to (45) for hub-to-tip ratios $\nu = 0.6$ and 0.3. The tangential velocity component at the hub due to a single radial vortex line is compared with the two-dimensional values in Figure 11 for $\nu = 0.6$ and Figure 25 for $\nu = 0.3$. The values in the poor convergency region have been excluded. The discrepancy between the three-dimensional and two-dimensional solutions is large for small $\theta$ and the maximum difference is about 25% of two-dimensional values for $\nu = 0.6$. The qualitative characteristics of the three-dimensional

tangential velocity component are very similar to those of two-dimensional values, and at $\zeta = 0$, $\zeta \to \pm \infty$, the velocities have the same limiting values mathematically (see Appendix D). The effects of the hub-to-tip ratio $\nu$ on the tangential velocity component is significant and the maximum difference from the two-dimensional solution is about 30% in the small $\theta$ region for $\nu = 0.3$ (see Figure 25). However, accurate three-dimensional values at points close to the singular points could not be obtained due to the poor convergency of the series expression as mentioned in Section 4.2.1.

The tangential velocity components at the mid radius and tip due to a single radial vortex line of strength unity are shown in Figures 12 and 13 for hub-to-tip ratio $\nu = 0.6$, and corresponding graphs for $\nu = 0.3$ are shown in Figures 26 and 27. At mid radius (Figure 12), the discrepancies between the three-dimensional and two-dimensional solutions vanish when the hub-to-tip ratio $\nu = 0.6$, but very small differences were found for $\nu = 0.3$ (see Figure 26). For both $\nu = 0.6$ and 0.3, the three-dimensional tangential velocity components at the hub for small $\theta$ are greater than the two-dimensional values, while those at the tip for small $\theta$ are smaller than the two-dimensional values (in absolute values). These three-dimensional inviscid effects may partially account for the higher (than the two-dimensional values) lift coefficients measured at the root and lower lift coefficients measured at the tip of a pump rotor by Oshima et al. (Reference 7).

The axial velocity components at the hub, mid radius and tip due to a single radial vortex line of unit strength are shown in Figures 14, 15, and 16 respectively, for hub-to-tip ratio $\nu = 0.6$. Corresponding graphs for $\nu = 0.3$ are shown in Figures 28, 29, and 30 respectively.

Similar to the tangential velocity components, the discrepancy between the three-dimensional and two-dimensional axial velocity components vanish at mid radius for $\nu = 0.6$ (see Figure 15), and very small differences were found at mid radius for $\nu = 0.3$ (see Figure 29). Also, the three-dimensional axial velocity components at the hub for small $\zeta$ ($< 0.2$) are smaller than two-dimensional values (see Figures 14 and 28) for both hub-to-tip ratio $\nu = 0.6$ and $0.3$. The magnitude of the discrepancy between the three-dimensional and two-dimensional axial velocity components for small $\zeta$ region are 10 to 15% for $\nu = 0.6$. However, for $\nu = 0.3$, for the small $\zeta$ region, the numerical results of the three-dimensional axial velocity components are poor. Thus, the discrepancy is not clear, but a larger discrepancy than that for $\nu = 0.6$ may be expected.

The radial velocity components at the mid radius due to a single radial vortex line of strength unity are shown in Figure 17 for $\nu = 0.6$ in Figure 31 for $\nu = 0.3$. The radial velocity components vanish at the hub and the outer casing wall. The typical radial velocity distributions are shown at the mid radius. However, the mid radius is not necessarily the point of maximum radial velocity. The maximum radial velocity usually occurs at a smaller radial coordinate than mid radius. From the comparison of the radial velocity components at mid radius for $\nu = 0.6$ and $\nu = 0.3$, the value for $\nu = 0.3$ is about 3 or 4 times larger than that for $\nu = 0.6$. From analytical considerations, it can be shown that the radial velocity components must vanish at $\zeta = 0$ for all $\theta$ except $\theta = 0^{\circ}$. The graphs do not show the small $\zeta$ region due to the lack of convergency of the series expression.

It is clear from the plots shown in Figures 11 to 17 and Figures 25 to 31 that the effects of the three-dimensionality are amplified at small hub-to-tip ratio ($\nu$). The order of the magnitude of the radial velocity components is almost 10% of the tangential and axial velocity components for hub-to-tip ratio $\nu = 0.6$, but for $\nu = 0.3$, it is more than 15%. With regard to tangential and axial velocity components, the discrepancy between two-dimensional and three-dimensional solutions is opposite in relative magnitude at the hub and tip locations for any hub-to-tip ratio. This discrepancy increases with decrease in hub-to-tip ratio. Finally, the three-dimensional numerical results were compared with References (2) and (4). The present numerical results for $\nu = 0.6$ are coincident with the results of Reference (4), but different from the results of Reference (2). However, no other numerical results are available for a small hub-to-tip ratio such as $\nu = 0.3$ for comparison.

### 4.2.3 Three-Dimensional Perturbed Flow Field Due to a Single Radial Source Line of Strength Unity and Its Comparison with the Two-Dimensional Solution

Numerical calculation of the three-dimensional flow field due to a radial source line has not been reported earlier. Even though the flow field around the blades depends mainly on the vortex distribution, the three-dimensional effects due to a source line (representing the thickness) can be of the same order as the three-dimensional effects due to a vortex line. This is especially true when there is appreciable radial variation in blade thickness. The three-dimensional perturbed velocity components due to a single radial source line of strength unity located at $\zeta_1 = 0$ and $\theta_{1,1} = 0^{\circ}$ were calculated from Equations (48), (49) and (50) for the hub-to-tip ratios $\nu = 0.6$ and 0.3. The

computer program can be used for the determination of the three-dimensional flow field due to a series of radial source lines of variable strength represented by the third-order polynomials, but only the case of constant strength (= 1.0) is shown in Figures 18 to 24 and Figures 32 to 38 together with two-dimensional solutions. The effects of the variable strength of the radial source lines will be shown in Section (4.3.4).

The tangential velocity components at the hub, mid radius and tip due to a single radial source line of strength unity are shown in Figures 18, 19, and 20 for a hub-to-tip ratio $\nu = 0.6$, and Figures 32, 33, and 34 for $\nu = 0.3$. Consider the two-dimensional flow field due to a vortex of strength unity and a source of strength unity. The magnitude of the two-dimensional tangential velocity components due to a vortex is the same as the two-dimensional axial velocity components due to a source except for the difference of sign. Similarly, the two-dimensional axial velocity components due to a vortex are the same magnitude as the two-dimensional tangential velocity components due to a source. The relative characteristics of the three-dimensional perturbed flow fields due to a single radial vortex line of strength unity and those due to a single radial source line of strength unity are very similar to the relative characteristics of the two-dimensional case as mentioned above. Hence, the three-dimensional tangential velocity components at the hub due to a single radial source line (see Figure 18) are quite similar to the axial velocity components at the hub due to a single radial vortex line (see Figure 14). However, the discrepancy between two-dimensional and three-dimensional solutions are opposite in relative magnitude. The tangential velocity at the hub due to a source

line is larger than the two-dimensional value (see Figure 18), but the axial velocity at the hub due to a vortex line is smaller than the two-dimensional value (see Figure 14). Similarly, the tangential velocity components at the mid radius (see Figure 19) and the tip (see Figure 20) due to a source line are very similar to the axial velocity components at mid radius (see Figure 15) and the tip (see Figure 16) due to a vortex line. It is clear from Figure 19 that the tangential velocity components at the mid radius due to a source line are the same as the two-dimensional values as in the case of a vortex (see Figure 15). The tangential velocity components at the tip due to a source line shown in Figure 20 are smaller than the two-dimensional values; however, in the corresponding graph of Figure 16, the axial velocity due to a vortex line is larger than that of the two-dimensional value. Comparing the tangential velocity components at the hub and at the tip due to a source line we find that at the hub the three-dimensional values are larger than the corresponding two-dimensional values while at the tip they are smaller than the two-dimensional values. The above discussion for the three-dimensional tangential velocity components due to a source line for the hub-to-tip ratio $\nu = 0.6$ is qualitatively valid for the case of the hub-to-tip ratio $\nu = 0.3$. Specifically, Figures 32, 33, and 34 are similar to Figures 28, 29, and 30 respectively, and the characteristics of the three-dimensional tangential velocity components relative to the two-dimensional values for $\nu = 0.3$ due to a source line are the same as those for hub-to-tip ratio $\nu = 0.6$. The relative behavior of the tangential velocity for $\nu = 0.3$ due to a source line at the hub and tip is also quite similar to that for $\nu = 0.6$. However, the magnitude of the discrepancy between the three-dimensional tangential velocity

components due to a source line and those for the two-dimensional case is amplified at small hub-to-tip ratio ($\nu$). At mid radius, the tangential velocity components for $\nu = 0.3$ due to a source line are slightly different from the two-dimensional values.

The axial velocity components at the hub, mid radius and tip due to a single radial source line of strength unity are shown in Figures 21, 22, and 23 for hub-to-tip ratio $\nu = 0.6$, and in Figures 35, 36, and 37 for $\nu = 0.3$ respectively. The axial velocity at the hub due to a source line for $\nu = 0.6$ shown in Figure 21 is similar to the tangential velocity at the hub due to a vortex line except for the difference of sign. In the same way, Figures 22 and 23 are similar to Figures 12 and 13 respectively. The axial velocity at mid radius due to a source line shown in Figure 22 is the same as the tangential velocity due to a vortex line, and the discrepancies between the three-dimensional and two-dimensional values vanish. The relative behavior of the axial velocity due to a source line at the hub and tip is such that, in the small $\zeta$ region, the three-dimensional axial velocity components at the hub are smaller than those for the two-dimensional case, but at the tip the three-dimensional values are larger than the two-dimensional values (see Figures 21 and 23). For the case of the small hub-to-tip ratio $\nu = 0.3$, the earlier comments are still valid, but the discrepancies between the three-dimensional axial velocity components due to a source line and the corresponding two-dimensional values are amplified by the small hub-to-tip ratio (see Figures 35, 36, and 37). Then, axial velocity at the mid radius for $\nu = 0.3$ due to a source line is slightly different from the two-dimensional axial velocity component. This may be partly due to poor convergency of series expressions, but the remaining part of the

discrepancies may be due to essential characteristics of small hub-to-tip ratio since mid radius is not necessarily the point of the same velocity as two-dimensional theory. The closed form of the tangential and radial velocity component due to a single radial source line of strength unity is not known so far, but the axial velocity component due to a source line vanishes at $\zeta = 0$ for any $\theta$ except $\theta = 0^{o}$, similar to the two-dimensional analysis. However, the limiting value at $\zeta \to \pm\infty$ is different from the two-dimensional solution since at $\zeta \to \pm\infty$, $(u_{s\zeta})_{3d} = \pm 1/(2\pi(1+\nu))$ in the three-dimensional case and $(u_{s\zeta})_{2d} = \pm 1/(4\pi\eta)$ in two-dimensional flow. Therefore, these limiting values are identical only for the mid radius ($\eta = (1+\nu)/2$), as shown in Figures 35, 36, and 37.

The radial velocity components at the typical radial coordinate $\eta = (1+\nu)/2$ due to a single radial source line of strength unity are shown in Figure 24 for $\nu = 0.6$ and in Figure 38 for $\nu = 0.3$, respectively. The order of magnitude of the radial velocity components is about 10% to 15% of the corresponding three-dimensional tangential and axial velocity components for $\nu = 0.6$ and 0.3, respectively. The behavior of the radial velocity components due to a source line are completely different from those due to a vortex line.

## 4.3 Numerical Solution of Turbomachinery Flow

### 4.3.1 Lifting Line Model

The purpose of this section is to merely point out the extent of three-dimensional effects due to hub-to-tip ratio and the number of the blades NB.

NB radial vortex lines of strength unity are located at $\zeta = 0$-plane spaced equally along the circumference. The coordinate of the i-th

radial vortex line is given by $\zeta = 0$, $\theta = 360^{o}/NB\ (i-1)$. The calculated tangential velocity distributions are given in Figures 39 and 40, for $\theta = 2^{o}$ and $9^{o}$ representing regions very close to and far away from the vortex lines. These two angular locations are smaller than the angle of the one spacing for any NB, but in the case of NB = 20, $\theta = 9^{o}$ represents the mid passage. The tangential velocity $u_{v\theta_{3d}}$ has the maximum absolute value with the maximum difference from two-dimensional solution at $\theta = 0^{o}$. In Figure 39, the ratio $(u_{v\theta_{2d}}/u_{v\theta_{3d}})$ is plotted along axial axis-$\zeta$. It is evident that the three-dimensional effects are larger for a smaller number of blades and the ratios of the two solutions are almost unity for NB = 20. In other words, the value of $(u_{v\theta_{3d}})$ will be closer to the two-dimensional solution for a larger number of the blades. The ratio $(u_{v\theta_{2d}}/u_{v\theta_{3d}})$ will approach unity far downstream and far upstream from the vortex lines. The effects of the small hub-to-tip ratio ($\nu = 0.3$) on $(u_{v\theta_{2d}}/u_{v\theta_{3d}})$ is large compared with those for the large hub-to-tip ratio ($\nu = 0.6$). The two-dimensional solution gives an underestimated absolute value of the tangential velocity at the hub and an overestimated value at the tip than the three-dimensional solution, and this is true for any number of the blades NB and for all hub-to-tip ratios. However, at mid radius ($\eta = 1+\nu/2$), the ratio $(u_{v\theta_{2d}}/u_{v\theta_{3d}})$ is very close to unity for all the cases. The maximum discrepancy between the two solutions is as much as 20% to 30%, especially for low hub-to-tip ratio and large blade spacing. It is evident that two-dimensional theories are inaccurate for low solidity and low hub-to-tip ratio blading used in certain applications. In Figure 41, the behavior of the ratio $(u_{v\theta_{2d}}/u_{v\theta_{3d}})$ for NB = 3 at 1/2, 1/4, 1/8, and 1/16 of the blade spacing, which corresponds to $\theta = 60^{o}$, $30^{o}$, $15^{o}$, and $7.5^{o}$ respectively, is shown. The largest departure of the ratio $(u_{v\theta_{2d}}/u_{v\theta_{3d}})$ from unity is at mid passage

($\theta = 60^{o}$). On the other hand, the largest difference of $|u_{v\theta_{2d}} - u_{v\theta_{3d}}|$ is 1/16 spacing point because of the short distance from the vortex lines.

It should be pointed out that the distribution of the axial velocity component due to equally spaced vortex lines on the $\zeta = 0$-plane decreases rapidly to zero for both two- and three-dimensional solutions, with respect to the increase in $\zeta$. This is especially true for NB = 20. Also, the order of magnitude of the induced axial velocity due to vortex lines is usually smaller than the corresponding tangential velocity, especially for NB = 20. The axial velocity is almost zero at the hub for small hub-to-tip ratios everywhere. The simple comparison of the ratio ($u_{v\zeta_{2d}}/u_{v\zeta_{3d}}$) when the absolute value of the axial velocity is small leads to misleading conclusions on the effects of NB. The comparison of the effects of NB were made at the point $\zeta = 0.1$, where the absolute value of axial velocity is relatively large. The calculated axial velocity ratios ($u_{v\zeta_{2d}}/u_{v\zeta_{3d}}$) on the plane of $\zeta = 0.1$ are shown in Figures 42a, 42b, and 42c for $\nu = 0.6$ and $\nu = 0.3$ at the hub, mid radius and tip, respectively, where s is the spacing angle and is equal to $360^{o}$/NB. The discrepancy between the two solutions is larger for small number of the blades at the hub for both $\nu = 0.6$ and 0.3. The behavior of the ratio ($u_{v\zeta_{2d}}/u_{v\zeta_{3d}}$) at the tip seems to be different from that at the hub; however, the order of magnitude of the axial velocity at the tip for NB = 20 is about 1/10 of the corresponding tangential velocity component. On the other hand, the order of the magnitude of the axial velocity at the tip for NB = 1 is almost the same as that of the corresponding tangential velocity. Therefore, three-dimensional effects are large for small hub-to-tip ratios with fewer blades. The two-dimensional solution gives overestimated absolute

values at the hub and underestimated values at the tip for small number of the blades. The ratio ($u_{v\zeta_{2d}}/u_{v\zeta_{3d}}$) at the mid radius is close to unity and the effects of NB and hub-to-tip ratio $\nu$ are relatively smaller at the hub and tip.

The radial velocity distributions are shown in Figure 43 for $\theta = 2^{o}$ and in Figure 44 for $\theta = 9^{o}$ at mid radius. The radial velocity is normalized with respect to the two-dimensional axial velocity at corresponding points since there is no radial velocity component in a two-dimensional flow. Comparing Figures 43 and 44, we find the magnitude of the radial velocity ratio at two different angular locations very close. The hub-to-tip ratio has a dominant effect compared with the number of the blades. Furthermore the radial velocities are about 10% to 40% of the two-dimensional axial velocity indicating the extent of three-dimensionality in the flow.

### 4.3.2 Source Line Model

The induced velocity due to NB radial source lines of unit strength spaced equally at $\zeta = 0$-plane is to be reported. The objective of this investigation is to examine the effects of the number of the blades NB and the hub-to-tip ratio $\nu$ on the flow field induced by equally spaced NB-radial source lines simulating the blade thickness. Generally, the flow field induced by source lines are orthogonal relative to those induced by vortex lines of the same magnitude. Namely, the distribution of the tangential velocity $u_{s\theta_{3d}}$ and axial velocity $u_{s\zeta_{3d}}$ due to source lines are similar to the distribution of the axial velocity $u_{v\zeta_{3d}}$ and tangential velocity $u_{v\theta_{3d}}$ due to vortex lines respectively.

The effects of the NB on the tangential velocity ratio ($u_{s\theta_{2d}}/u_{s\theta_{3d}}$) are plotted for NB = 1, 3, 5 and 20 at $\zeta = 0.1$ in Figures 45a, 45b, and 45c. The order of the magnitude of the tangential velocity due to source lines $u_{s\theta_{3d}}$ is usually smaller than the corresponding axial velocity due to source lines. This is especially true for NB = 20, where tangential velocity $u_{s\theta_{3d}}$ is almost zero. Therefore, from Figures 45a, 45b, and 45c, the effects of the NB on the ratio ($u_{s\theta_{2d}}/u_{s\theta_{3d}}$) must be carefully considered since for extremely large NB, the absolute value of the tangential velocity is very small while the ratio difference is quite large. Alternatively, for smaller NB, the absolute value is relatively larger and the ratio difference is relatively smaller. It is clear that the effects of the hub-to-tip ratio are dominant, unlike the effect of NB, on the three-dimensionality of the flow field.

As mentioned in the discussion of axial velocity induced by a single radial source line (Figure 35) spanning an annulus, the three-dimensional solution is very different from the two-dimensional solution at far up and down stream. The two-dimensional solution is the solution expressed in a cylindrical coordinate system. The two-dimensional unrolled solution has no interference effects due to the flow field at other radii ($\eta$). At far up and down stream ($\zeta \to \pm \infty$), the ratio $u_{s\zeta_{2d}}/u_{s\zeta_{3d}}$ is independent of NB. In the case of the tangential velocity $u_{v\theta_{3d}}$ and axial velocity $u_{v\zeta_{3d}}$ induced by vortex lines, and the tangential velocity $u_{s\theta_{3d}}$ induced by source lines, the ratio of these values to the two-dimensional solution is unity at far up and down stream ($\zeta \to \pm \infty$) since $u_{v\zeta_{3d}}$ and $u_{s\theta_{3d}}$ vanish at $\zeta = \pm \infty$ as the two-dimensional solution does. By the irrotationality condition, fluid layer at any radius $\eta$ has the same amount of circulation given by

$NB \cdot \Gamma/2$ at $\zeta = \pm \infty$. However, in the case of the axial velocity $u_{s\zeta_{3d}}$ induced by source lines, the fluid layer at any radius $\eta$ has an identical magnitude given by

$$(u_{s\zeta_{3d}})_{\zeta \to \pm \infty} = \pm \frac{NB \cdot Q}{2\pi(1+\nu)} \quad . \tag{86}$$

But the two-dimensional value $u_{s\zeta_{2d}}$ is a function of the radius $\eta$ even at $\zeta = \pm\infty$ since,

$$(u_{s\zeta_{2d}})_{\zeta \to \pm \infty} = \frac{NB \cdot Q}{4 \pi \eta} \quad . \tag{87}$$

Hence, the ratio $(u_{s\zeta_{2d}}/u_{s\zeta_{3d}})$ has the value

$$(u_{s\zeta_{2d}}/u_{s\zeta_{3d}})_{\zeta \to \pm \infty} = \frac{1 + \nu}{2\eta} \quad . \tag{88}$$

The effects of the NB on the axial velocity ratio $(u_{s\zeta_{2d}}/u_{s\zeta_{3d}})$ are shown in Figure 46 along the $\zeta$ axis for several NB at $\theta = 2^{o}$, a region relatively near the singular points. The effect of the number of the blades is large for large NB near the radial source lines, but at the far down stream, the ratio is independent of NB and has the value $1+\nu/2\eta$ as mentioned above. The order of the magnitude of the axial velocity $u_{s\zeta_{3d}}$ induced by source lines is usually larger than that of the corresponding tangential velocity $u_{s\theta_{3d}}$ which goes to zero rapidly, and this is also true for the two-dimensional case. The difference between the two solutions is great for small hub-to-tip ratio ($\nu = 0.3$), especially at the hub. However, at mid radius, the difference between two solutions is very small compared with the differences at the hub and tip.

Finally, the radial velocity distribution at the mid radius induced by NB radial source line of unit strength located at the plane $\zeta = 0$ is calculated for $\nu = 0.6$ and $0.3$ at $\theta = 2^{o}$ and is shown in Figure 47. The radial velocity distributions are plotted in terms of the ratio radial velocity to two-dimensional axial velocity component ($u_{s\eta}/u_{s\zeta_{2d}}$). As indicated earlier, the radial velocity due to vortex lines does not change its sign with respect to $\zeta$ or $\theta$. On the other hand, the radial velocity due to source lines changes its sign with respect to $\zeta$ or $\theta$. The plot shown in Figure 47 shows the effects of the hub-to-tip ratio and the number of the blades on the radial velocity induced in three-dimensional flow.

### 4.3.3 Lifting Surface Model Including Thickness Effects

In order to examine the effects of the stagger angle, number of the blades, thickness and hub-to-tip ratio, a system of NB series of radial vortex and source lines are considered for several simple models. The model consists of NB-equally spaced blades and each blade is represented by eight vortex and source lines arranged equidistant along the camber line of the blades (see Figures 48 and 49). In the present calculation, the camber is assumed to be zero and the calculations are carried out for stagger angles (at mid radius) of $0^{o}$, $18^{o}$, $36^{o}$, and $54^{o}$. The nondimentional chord length of the blades C is equal to 2.0 (twice the outer casing radius) on the cylindrical plane of radius $1+\nu/2$ (see Figure 49). The distribution of the strength of series vortex and source lines $\Gamma_j$, $Q_j$, $j = 1, 2, \ldots, 8$ representing the blades are assumed to be the same at all stagger angles $\lambda$, number of the blades NB and hub-to-tip ratio $\nu$. Even though this is not true for a practical blade

configuration, the main objective of this investigation is to understand the extent of three-dimensional effects and, from this point of view, these calculations are very useful. The values of $\Gamma_j$ and $Q_j$ used in this calculation are given in Table 4, where $\sum_{j=1}^{JVS}$ is equal to -1.0 according to our definition and $\sum_{j=1}^{JVS}$ is zero, satisfying the closure condition.

Table 4. Strength of Vortex and Source Configuration Used.

| | j=1 | j=2 | j=3 | j=4 | j=5 | j=6 | j=7 | j=8 |
|---|---|---|---|---|---|---|---|---|
| $\Gamma_j$ | -0.44000 | -0.16843 | -0.11862 | -0.09069 | -0.07053 | -0.05360 | -0.03824 | -0.01987 |
| $Q_j$ | 0.44559 | 0.05441 | -0.03425 | -0.08085 | -0.10545 | -0.11279 | -0.10301 | -0.06366 |

The location of the vortex and source lines are specified only by the tangential and axial coordinate ($\theta$, $\zeta$) since the vortex and source lines are assumed to be radial. The stagger angle $\lambda$, the coordinate of the vortex and source lines and the calculation points in $(\zeta', \eta_{mid}\theta)$-plane and those in $(\zeta', \theta)$-plane are shown in Figure 49 and in Figure 50, where $\zeta'$ is the line parallel to $\zeta$-axis at mid radius. The calculation points are located midway between the singular points. The induced velocities are calculated at points very near the blade at $\Delta\theta = 2^{\circ}$ and 1/2, 1/4, 1/8, 1/16-spacing points (See Figure 50).

It should be pointed out that in the present model every blade has the same distribution of $\Gamma_j$ and $Q_j$ without regard to the effects of different stagger angles ($\lambda$) and the number of the blades (NB), which is directly related to solidity. To avoid a misleading conclusion, the velocity components due to vortex and source will be shown separately to point out the effects of NB, $\lambda$ and $\nu$.

The typical tangential velocity distribution at the hub induced by NB-radial vortex lines is shown in Figures 51 and 52 for the same hub-to-tip ratio $\nu = 0.3$ and number of the blades NB = 1 but at different stagger angles ($\lambda = 0^o$ and $\lambda = 54^o$) to show the effect of stagger angle on the three-dimensional solution. The abscissa represents tangential direction and s is equal to one spacing angle ($s = 360^o/NB$). Figure 53 shows the ratio $u_{v\theta_{2d}}/u_{v\theta_{3d}}$ in the chordwise direction for $\lambda = 0^o$, $\Delta\theta = 2^o$ at the hub, mid radius and tip. The angular location $\Delta\theta = 2^o$ is chosen since the maximum discrepancy in the tangential velocity occurs near this location. As mentioned in Section 4.3.1, the effects of the number of the blades on the tangential velocity are quite similar to those of the lifting line model. Namely, for large NB, the ratio $u_{v\theta_{2d}}/u_{v\theta_{3d}}$ goes to unity. The maximum difference between the two solutions (about 30%) occurs when NB = 1, $\nu = 0.3$. The ratio $u_{v\theta_{2d}}/u_{v\theta_{3d}}$ in the vicinity of a leading edge is sometime very large, but the absolute value of $u_{v\theta_{3d}}$ at this point is usually small due to cancellation of the induced flow due to $\Gamma_{i,1}$ and $\Gamma_{i,2}$. Hence, the ratio $u_{v\theta_{2d}}/u_{v\theta_{3d}}$ at these points should not be emphasized. In Figures 54 and 55, the tangential velocities at two radial locations $\eta = \nu$ (hub) and $\eta = 1.0$ (tip) for NB = 3, $\lambda = 18^o$ and $\nu = 0.3$ are shown. The difference between two-dimensional and three-dimensional solutions are larger at the hub than at the tip. The absolute values are generally larger at the hub. Generally, the difference between the two solutions at the mid radius are negligibly small. The two-dimensional values are more uniform across the passage than the three-dimensional values at the hub and this trend is reversed at the tip. Two-dimensional solutions underestimate the maximum tangential velocity $u_{v\theta_{2d}}$ at the hub and

overestimated the value at the tip. The effects of the hub-to-tip ratio $\nu$ and the number of the blades (NB) on the difference between two solutions are more dominant than those due to stagger angle $\lambda$.

The effects of the number of the blades on the induced axial velocity $u_{\nu\zeta}$ due to the NB-series of radial vortex lines show the same trend as the behavior of the axial velocity in the "Lifting Line Model" mentioned in section 4.3.1. Namely, for large NB, the axial velocity goes to zero quite rapidly, especially at the hub. Therefore, the case of NB=1 is selected to discuss the effects of stagger angle $\lambda$. In Figures 56 and 57, the behavior of the axial velocity $u_{\nu\zeta_{3d}}$ and $u_{\nu\zeta_{2d}}$ are shown for widely varying stagger angle $\lambda = 0^{o}$ and $54^{o}$ for NP=1, $\nu = 0.3$ at the hub. The trend is almost similar for both cases, but the discrepancy at large stagger angles is slightly larger than that at small stagger angles. To show these effects clearly, the axial velocity ratio $u_{\nu\zeta_{2d}}/u_{\nu\zeta_{3d}}$ for NB=1 at $\zeta/c \cos\lambda = 0.0$ and $\eta = \nu$ (hub) are shown in Figure 58. The axial location $\zeta/c \cos\lambda = 0.0$ is selected since maximum difference between two solutions occurs near this location. The axial velocity ratio is larger for larger stagger angles at both hub and tip, and is also amplified by small hub-to-tip ratio. Incidentally, the ratio at large axial locations should not be emphasized due to small absolute values. The departure at the hub is larger than those at the tip and at mid radius.

The radial velocities induced by the NB-series of radial vortex lines are discussed below. The radial velocity distributions $u_{\nu\eta}/\sqrt{\Sigma\Gamma^2}_j$ is plotted along the tangential direction in Figure 59 at the mid radius and at $\zeta/c \cos\lambda = 0.0$ for $\lambda = 18^{o}$, $\nu = 0.6$ and 0.3 for various values of NB. It is clear that the small hub-to-tip ratio causes larger radial

velocity than the large hub-to-tip ratio, and the larger number of the blades makes the radial velocity distribution uniform along the tangential direction. The effect of the stagger angle $\lambda$ is relatively smaller than that of hub-to-tip ratio and number of blades (NB). Generally, the order of magnitude of the radial velocity induced by NB-series of radial vortex lines is approximately 15% of the maximum tangential and axial velocity components for $\nu = 0.6$ and 30% for $\nu = 0.3$.

Unlike the vortex system, the tangential velocity due to the NB series of radial source lines $u_{s\theta_{3d}}$ decreases relatively slowly along the axial direction. In order to examine the effects of the stagger angle $\lambda$, two chordwise planes, such as $\zeta/c \cos\lambda = 0$ and 1.0, are selected. The ratio $u_{s\theta_{2d}}/u_{s\theta_{3d}}$ is plotted along $\theta$ axis for $\nu = 0.3$ and NB = 1 at the hub in Figures 60 and 61. Also, the effects of hub-to-tip ratio ($\nu$) on the ratio $u_{s\theta_{2d}}/u_{s\theta_{3d}}$ for $\nu = 0.6$, NB = 1 at the hub are plotted in the same figure only for $\lambda = 0^{o}$ and $54^{o}$. The effect of the hub-to-tip ratio $\nu$ is more dominant than that of $\lambda$.

The axial velocity due to the NB-series of radial source lines $u_{s\zeta_{2d}}$ and $u_{s\zeta_{3d}}$ is usually larger than the corresponding tangential velocity $u_{s\theta_{2d}}$ and $u_{s\theta_{3d}}$, and different from the induced velocity due to a vortex system. The axial velocity $u_{s\zeta_{3d}}$ due to the NB-series of radial source and sink lines causes quite a large discrepancy from the two-dimensional solution for large NB, especially at the hub for small hub-to-tip ratio as mentioned in the "Source Line Model". The effects of the NB on the ratio $(u_{s\zeta_{2d}}/u_{s\zeta_{3d}})$ for zero stagger angle ($\lambda = 0$) are shown in Figure 62, (NB = 1, 3, 5, 20 for $\nu = 0.3$ and NB = 1, 20 for $\nu = 0.6$). For reference, the limiting values of $(u_{s\zeta_{2d}}/u_{s\zeta_{3d}})$ at far downstream $\zeta = \infty$ are also shown in the graph. They are $(1+\nu/2\eta) = 2.17$ at

the hub and 0.65 at the tip for $\nu = 0.6$. At the point close to the leading edge and trailing edge, the ratio has no meaning, since the axial velocity $u_{s\zeta_{3d}}$ is very small. The ratio $(u_{s_{2d}}/u_{s_{3d}})$ at the mid radius is very close to unity except near the leading edge and the trailing edge. The effects of stagger angle on the ratio $(u_{s\zeta_{2d}}/u_{s\zeta_{3d}})$ at the hub for NB = 20 are shown in Figure 63 in the region very close to the singular point ($\Delta\theta = 2^{o}$). The effects of stagger are negligible for large hub-to-tip ratio ($\nu = 0.6$), and the effects of NB and $\nu$ are more dominant than those of stagger.

The radial velocity distribution $u_{s\eta}/\sqrt{\Sigma Q_j^2}$ induced by NB series of radial source lines are shown in Figure 64 along the tangential direction for $\lambda = 18^{o}$ at $\zeta/c \cos\lambda = 0$ at mid radius for several NB and $\nu$. Similar to the vortex system, the radial velocities due to the NB series of radial source lines for small hub-to-tip ratio ($\nu = 0.3$) are larger than those of large hub-to-tip ratio. The larger number of the blades NB makes the distribution of the radial velocity uniform along the tangential direction. However, the radial velocity induced by the NB series of radial source lines for large NB is larger than that for small NB. Therefore, for the case of large NB and small hub-to-tip ratio, the radial velocity due to source lines is not necessarily small compared with other velocity components. The effect of the stagger angle $\lambda$ is relatively smaller than those due to NB and $\nu$.

### 4.3.4 Effects of the Radial Source Lines of Variable Strength

All the example calculations given in the preceding section were carried out for a series of radial vortex and source lines of constant strength. However, it is not necessary for a radial source line to be

of constant strength as mentioned in Section 2.2. It is expected that a series of source lines of variable strength can have three-dimensional effects directly. In order to examine the effects of the radial source line of variable strength along the radial direction, a three-bladed system of symmetric profiles and of zero stagger angle was considered for hub-to-tip ratio $\nu = 0.6$. Each blade is replaced only by a pair of radial source lines $Q_{i,1}$ and $Q_{i,2}$. The locations of $Q_{i,1}$ and $Q_{i,2}$ are shown in Figure 65, and the values of them are given by

$$Q_{i,1} = -0.5\eta + 0.9 \tag{89}$$

and

$$Q_{i,2} = 0.5\eta - 0.9, \tag{90}$$

where $i = 1$, 2 and 3. For the sake of convenience, the inlet flow velocity on which the three-dimensional perturbed velocities are superimposed is taken to be unity. For several angular locations the numerical results of the pressure distribution based on the inlet flow velocity are shown in Figures 66 and 67 at $\zeta = 0$ and $\zeta = 0.5$, respectively. The point $\zeta = 0$ is near the leading edge and $\zeta = 1.0$ is near the trailing edge. The flow field corresponding to $\zeta = 1.0$ is the same as that at $\zeta = 0$, and the values for negative $\theta$ are the same as those for positive $\theta$ by symmetry. At $\zeta = 0$, the discrepancies between the two- and three-dimensional analyses are quite small for any $\theta$, and the values based on the analyses are coincident at mid radius $\eta = 0.8$ (see Figure 66). However, in the region near the suction surface of the blade at $\zeta = 0.5$, the pressure coefficients based on the three-dimensional analysis are different near the hub and tip (see Figure 67). At mid radius, the difference between the two-dimensional and three-dimensional pressure coefficients vanish. For comparison, the same blade

system with constant strength of the radial source lines, $Q_{i,1} = 0.2$ and $Q_{i,2} = -0.2$, is shown in Figures 68 and 69. The strength of the source lines is taken to be the integrated mean value of the preceding model. Comparing the two cases, the discrepancies between the two-dimensional unrolled solutions and the three-dimensional solutions are relatively smaller than those of variable strength source lines. Thus, the effect of a source line of variable strength upon the three-dimensional flow field is large and the discrepancies between the two- and three-dimensional analyses are amplified by the variation of the strength of the source line along the radial direction. Furthermore, the differences between the pressure coefficients of the two analyses vanish at mid radius for the hub-to-tip ratio $\nu = 0.6$ for both constant and variable strength source lines.

# CHAPTER V

# CONCLUSIONS

The flow field in the axial flow turbomachinery encountered in practice is three-dimensional and is affected by viscosity and compressibility. Therefore, the three-dimensional potential flow theory can be used only for restricted three-dimensional flow problems because of the assumed incompressible, irrotational, and inviscid flow conditions. The three-dimensional potential flow theory can play an important part in the clarification of the three-dimensional effects on the flow field of an incompressible perfect fluid. The three-dimensional potential flow theory based on the analysis of Rossow (3) and Tyson (2) was modified in order to predict the three-dimensional flow effects. The blade row is replaced by a series of radial vortex lines of constant strength along the radial direction and a series of radial source lines of variable strength along the radial direction. The perturbed velocity field due to a single radial vortex and source line of constant strength was calculated for hub-to-tip ratios $\nu = 0.6$ and 0.3. The perturbed velocity field due to a radial vortex line of constant strength for $\nu = 0.6$ was coincident with the results of Reference (4). For the perturbed flow field due to a radial source line, there is no other numerical result available for comparison. The qualitative behavior, however, is very similar to that of the two-dimensional unrolled solutions except for the radial velocity components. The characteristic behavior of the three-dimensional perturbed flow field due to a single radial vortex and source line of strength unity discussed in Sections 4.2.2 and 4.2.3 are summarized below:

a) The qualitative behavior of the tangential and axial velocity components is similar to that for two-dimensional unrolled solutions. The maximum discrepancies between both analyses are 25% for $\nu = 0.6$ and 30% for $\nu = 0.3$.

b) The tangential and axial velocity components due to a single radial vortex line of constant strength are very similar to the axial and tangential velocity components due to a single radial source line of strength unity as in the two-dimensional unrolled solution. Also, the behavior of the velocity components due to a source line relative to the two-dimensional values is always opposite to that due a vortex line.

c) The behavior of the radial velocity components due to a single radial vortex and a source line of constant strength are very different.

d) At mid radius ($\eta = 1+\nu/2$), the tangential and axial velocity components of the three-dimensional flow field are very close to those for two-dimensional theory for hub-to-tip ratio $\nu = 0.6$, but small discrepancies between the two analyses were found for $\nu = 0.3$.

e) The three-dimensional effects are amplified by a small hub-to-tip ratio.

f) The discrepancy between two-dimensional and three-dimensional solution at the hub ($\eta = \nu$) are opposite to those at the tip ($\eta = 1.0$) and these are amplified by a small hub-to-tip ratio for both a vortex line and a source line.

The three-dimensional potential flow theory was modified to solve the three-dimensional flow field around a blade row of NB blades, where each blade is replaced by a series of radial vortex lines of constant strength and a series of radial source lines of variable strength.

Example calculations were carried out for the "Lifting Line Model", "Source Line Model", "Lifting Surface Model Including Thickness Effects" and "Effects of the Radial Source Line of Variable Strength". In the first and second example calculations, each blade is represented by a single radial vortex line ($\Gamma = -1.0$) or a source line ($Q = 1.0$), and the effects of the number of the blades NB and hub-to-tip ratios are examined. The effects of the stagger angle $\lambda$ together with NB and $\nu$ are examined in the third example calculation in which each blade is replaced by a series of radial vortex lines and source lines of constant strength. The calculations are carried out for stagger angles $0^{\circ}$, $18^{\circ}$, $36^{\circ}$, $54^{\circ}$, number of the blades NB = 1, 3, 5, 20 and hub-to-tip ratio $\nu = 0.6$ and 0.3. Finally, the effects of the radial source line of variable strength are investigated for simple models. The characteristic features of the three-dimensional flow field are summarized below:

a) The effects of the small hub-to-tip ratio on the discrepancy between the two- and three-dimensional solutions are greater than those of the number of the blades NB and the stagger angle $\lambda$.

b) Effects of the stagger angle $\lambda$ on the discrepancies between two solutions is usually smaller than those due to NB and $\nu$.

c) Small number of blades (NB) cause larger discrepancies between two solutions, especially at the hub, except for the axial and radial velocity components due to NB series of radial source lines. Alternatively, the axial and radial velocity components due to source lines are amplified by large number of the blades (NB) together with small $\nu$.

d) The radial source line of variable strength causes large discrepancy between two solutions even for relatively large hub-to-tip ratio, but at the mid radius, the discrepancies vanish for $\nu = 0.6$.

# REFERENCES


1. Meyer, R. "Beitrag zur Theories feststehender Schaufelgitter," Mitt. Aus Dem Inst. Aerodynamic (E.T.H., Zurich) Report 11, 1946 (Publisher, Verlag Leeman, Zurich. English Translation ARC 8869).

2. Tyson, R. N., Jr. "Three-Dimensional Interference Effects of a Finite Number of Blades in an Axial Turbomachine," November 1952, California Institute of Technology, Hydrodynamics Laboratory, Report No. E-19.1.

3. Rossow, Vernon J. "An Analysis of the Error Involved in Unrolling the Flow Field in Turbine Problem," Mitt Aus Dem Inst. Aerodynamik (E.T.H., Zurich) Report 23, 1957 (Publisher, Verlag Leeman, Zurich).

4. Etter, R. J. and van Dyke, P., "Three-Dimensional Flow Field from a Radial Vortex Filament," December 1969, Hydronautics Incorporated Technical Report 703-7.

5. Love, Carl H. "Abscissas and Weights for Gaussian Quadrature for N = 2 to 100, and N = 125, 150, 175, 200," December 1966, National Bureau of Standard Monograph 98.

6. Tamura, A., Howells, R., and Lakshminarayana, B. "Three-Dimensional Potential Flow Around a Body Spanning an Annulus: Computer Program and Solution," Applied Research Laboratory, The Pennsylvania State University. Technical Memorandum 73-173, 1973.

7. Oshima, M., et al. "Blade Characteristics of Axial Impellers," Proc. 2nd Int. JSME Symposium on Fluid Machinery and Fluidics, Tokyo, Japan, Vol. 1, 1973, p. 119.

8. Watson, G. N. Theory of Bessel Functions. Cambridge University Press, 1958.

9. Milne-Thomson, L. M. Theoretical Hydrodynamics. McMillan, 1968.

# APPENDIX A

## Specification of the Boundary Condition for Radial Vortex Line and Source Line

### Specification of the Boundary Conditions for a Radial Vortex Line

The single radial vortex line of constant strength $\Gamma$ located at $\zeta = 0$, $\theta = 0^{o}$ is split into $\gamma d\omega$ (see Figure 70) and distributed over $-\delta/2 < \theta < \delta/2$ as given by

$$\int_{-\delta/2}^{\delta/2} \gamma d\omega = \gamma\delta = \Gamma \quad . \tag{A1}$$

The induced velocity $\Delta q$ at $(\eta, \theta, \delta/2)$ due to $\gamma d\omega$ is given by

$$\Delta q = \gamma d\omega/4\pi h \ (\cos \alpha_1 - \cos \alpha_2) \quad , \tag{A2}$$

where

$$\cos \alpha_1 = \frac{\overline{AD}}{\overline{DP'}} = \frac{\eta \cos (\theta - \omega) - m}{\sqrt{\eta^2 + m^2 + (\Delta\zeta/2)^2 - 2m\eta \cos (\theta - \omega)}} \quad , \tag{A3}$$

$$\cos \alpha_2 = -\frac{\overline{AL}}{\overline{P'L}} = -\frac{\ell + m - \eta \cos (\theta - \omega)}{\sqrt{\eta^2 + (\ell+m)^2 + (\Delta\zeta/2)^2 - 2(\ell+m)\eta\cos(\theta - \omega)}} \tag{A4}$$

and

$$\sin \alpha = \frac{\overline{PP'}}{h} = \frac{\Delta\zeta/2}{\sqrt{\eta^2 \sin^2 (\theta - \omega) + (\Delta\zeta/2)^2}} \quad . \tag{A5}$$

Therefore, the tangential velocity component of the induced velocity due to the total of the split radial vortex lines is given by

$$v_\theta = \int_{-\delta/2}^{\delta/2} \Delta q \sin\alpha \cos(\theta - \omega)\, d\omega$$

$$= \frac{\gamma}{4\pi} \int_{-\delta/2}^{\delta/2} \frac{\Delta\zeta/2 \cos(\theta-\omega)}{\eta^2 \sin^2(\theta-\omega) + (\Delta\zeta/2)^2} \left\{ \frac{\eta \cos(\theta-\omega) - m}{\sqrt{\eta^2+m^2+(\Delta\zeta/2)^2 - 2m\eta\cos(\theta-\omega)}} + \right.$$

$$\left. \frac{\ell + m - \eta\cos(\theta-\omega)}{\sqrt{\eta^2 + (\ell+m)^2 + (\Delta\zeta/2)^2 - 2(\ell+m)}} \right\} d\omega \quad . \tag{A6}$$

Integrate with respect to $\omega$ and take the limit as $\Delta\zeta \to 0$; then,

$$\lim_{\Delta\zeta \to 0} v_\theta = \gamma/2\eta, \qquad \text{for } -\delta/2 < \theta < \delta/2 \quad . \tag{A7}$$

Specification of the Boundary Conditions for a Radial Source Line

In the same way as for the vortex line, a radial source line of variable strength $Q(\eta)$ located at $\zeta = 0$, $\theta = 0^o$ is split into $\mu(\eta)d\omega$ (see Figure 71) and distributed over $-\delta/2 < \theta < \delta/2$ as given by

$$\int_{-\delta/2}^{\delta/2} \mu(\eta)\, d\omega = \mu(\eta)\delta = Q(\eta) \quad . \tag{A8}$$

The induced velocity due to a split source $\mu(\eta)$ is represented by

$$\Delta q = \frac{\mu(\eta)\, d\omega}{2\pi\sqrt{\eta^2\sin^2(\theta - \omega) + (\Delta\zeta/2)^2}} \quad . \tag{A9}$$

The axial component of the induced velocity due to the total of the split radial source lines is given by

$$v_\zeta = \int_{-\delta/2}^{\delta/2} \Delta q \cos\alpha \, d\omega$$

$$= \frac{\Delta\zeta}{4\pi} \int_{-\delta/2}^{\delta/2} \frac{\mu(\eta)}{\eta \sin^2(\theta - \omega) + (\Delta\zeta/2)^2} \, d\omega \, . \qquad \text{(A10)}$$

Integrate and take a limit as $\Delta\zeta \to 0$; then,

$$\lim_{\Delta\zeta \to 0} v_\zeta = \mu(\eta)/2\eta, \quad \text{for } -\delta/2 < \theta < \delta/2 \, . \qquad \text{(A11)}$$

## APPENDIX B

### Elimination of the Summation About i in the Series Summation

Usually the blade row in turbomachinery is constructed by equally spaced blades of the same profile. Therefore, the distribution of the series of vortex and source lines is the same for any blade. Now, $\theta_{i,j}$ is the angular coordinate of the location of the j-th vortex or source line for the i-th blade. From the periodic characteristics, we get

$$\theta_{i,j} = \theta_{1,j} + (2\pi/NB)(i - 1) \quad . \tag{A12}$$

Using Equation (A12), we can eliminate the summation with respect to i in Equation (39) in Section 3.1. Thus,

$$\sin m(\theta-\theta_{i,j}) = \sin m(\theta-\theta_{1,j})\cos 2m\pi(i-1)/NB - \cos m(\theta-\theta_{i,j})\sin 2m\pi(i-1)/NB \tag{A13}$$

Let

$$S(j,m) = \sum_{n=1}^{\infty} \exp(\mp K_{mn}(\zeta-\zeta_j)) \cdot F_v(K_{mn}, \nu) \cdot Z_m(K_{mn}\eta) \quad . \tag{A14}$$

Then

$$\Phi_v = \mp \sum_{j=1}^{JVS} \frac{\Gamma_j}{4\pi} \sum_{i=1}^{NB} (\theta-\theta_{1j} - \frac{2\pi}{NB}(i-1) + 2 \sum_{m=1}^{\infty} \frac{1}{m} [\sin m(\theta-\theta_{1j})\cos \frac{2m\pi(i-1)}{NB}$$

$$- \cos m(\theta-\theta_{1j}) \sin \frac{2m\pi(i-1)}{NB}] S(j,m))$$

$$= \sum_{j=1}^{JVS} \frac{\Gamma_j}{4\pi} \left(NB(\theta-\theta_{1j}) - (NB-1)\pi + 2 \sum_{m=1}^{\infty} \left[\frac{1}{m} \sin m(\theta-\theta_{1j}) \sum_{i=1}^{NB} \cos \frac{2m\pi(i-1)}{NB}\right.\right.$$

$$\left.\left. - \cos m(\theta-\theta_{1j}) \sum_{i=1}^{NB} \sin \frac{2m\pi(i-1)}{NB} \right] S(j,m)\right) \qquad \text{(A15)}$$

and

$$\sum_{i=1}^{NB} \cos \frac{2m\pi(i-1)}{NB} = \cos\left((1-1/NB) \cdot m\pi\right) \cdot \sin m\pi / \sin(m\pi/NB),$$

$$= 0$$

where $m \neq \ell \cdot NB$. When m is a multiple of NB ($m = \ell \cdot NB$), we get

$$\sum_{i=1}^{NB} \cos \frac{2m\pi(i-1)}{NB} = \sum_{i=1}^{NB} \cos\left((i-1) \cdot 2\ell\pi\right) = NB.$$

Similarly,

$$\sum_{i=1}^{NB} \sin \frac{2m\pi(i-1)}{NB} = \sin\left((1-1/NB)m\pi\right) \cdot \sin m\pi / \sin(m\pi/NB)$$

$$= 0 ,$$

where $m \neq \ell \cdot NB$, and when $m = \ell \cdot NB$,

$$\sum_{i=1}^{NB} \sin \frac{2m\pi(i-1)}{NB} = \sum_{i=1}^{NB} \sin\left((i-1) \cdot 2\ell\pi\right) = 0$$

Therefore, the velocity potential reduces to

$$\Phi_v = \sum NB \sum_{j=1}^{JVS} \frac{\Gamma_j}{4\pi} \left(\theta-\theta_{1j} - (1 - 1/NB)\pi + 2 \sum_{\ell=1}^{\infty} \frac{\sin k(\theta-\theta_{ij})}{k} \cdot S(j,k)\right), \qquad \text{(A16)}$$

where $k = \ell \cdot NB = 1, 2, 3, \ldots$ In the same way, the summation with respect to i in equation (46) can be eliminated.

# APPENDIX C

## Related Bessel Function and Characteristics of the Series Expression

a) Function $Z_m(K_{mn}\eta)$

$$Z_m(k_{mn}\eta) = J_m(K_{mn}\eta)\left[\frac{\partial Y_m(K_{mn}\eta)}{\partial\eta}\right]_{\eta=1} - \left[\frac{\partial J_m(K_{mn}\eta)}{\partial\eta}\right]_{\eta=1} Y_m(K_{mn}\eta) \quad . \tag{A17}$$

From Equation (A17)

$$Z_m(K_{mn}\eta) = K_{mn}\{J_m(\chi)\cdot\left[\frac{\partial Y_m(\chi)}{\partial\chi}\right]_{\chi=K_{mn}} - \left[\frac{\partial J_m(\chi)}{\partial\chi}\right]_{\chi=K_{mn}}\cdot Y_m(\chi)\} \quad ,$$

where $\chi = K_{mn}\eta$. Then by Lommel's formula for Bessel Function,

$$[Z_m(K_{mn}\eta)]_{\eta=1} = K_{mn}\left[\frac{2}{\pi\chi}\right] = \frac{2}{\pi} \tag{A18}$$

and also from the boundary condition given by Equation (11) in Section 2.1,

$$\frac{J_m'(K_{mn}\nu)}{Y_m'(K_{mn}\nu)} = \frac{J_m'(K_{mn})}{Y_m'(K_{mn})} \quad . \tag{A19}$$

Then,

$$Z_m(K_{mn}\eta) = \frac{Y_m'(K_{mn})}{Y_m'(K_{mn}\nu)}\ \bar{Z}_m(K_{mn}\eta) \quad , \tag{A20}$$

where

$$\bar{Z}_m(K_{mn}\eta) = J_m(K_{mn}\eta)\ Y_m'(K_{mn}\nu) - J_m'(K_{mn}\nu)\ Y_m(K_{mn}\eta) \quad .$$

Therefore

$$[\bar{Z}_m(K_{mn}\eta)]_{\eta\ \nu} = [Z_m(\chi)]_{\chi=K_{mn}\nu} = K_{mn}[J_m(\chi)\ \frac{\partial Y_m(\chi)}{\partial\chi} - \frac{\partial J_m(\chi)}{\partial\chi}\ Y_m(\chi)]_{\chi=\nu K_{mn}}$$

by Lommel's formula

$$[Z_m(K_{mn}\eta)]_{\eta=\nu} = K_{mn}\,[2/\pi\chi]_{\chi=K_{mn}\nu} = 2/\nu\pi \quad .$$

Hence,

$$[Z_m(K_{mn}\eta)]_{\eta=\nu} = \frac{2}{\nu\pi}\,\frac{Y_m'(K_{mn})}{Y_m'(K_{mn}\nu)} \quad . \tag{A21}$$

b) Integral and Derivatives of $Z_m(K_{mn}\eta)$

From boundary condition (A20),

$$\left[\frac{\partial Z_m(K_{mn}\eta)}{\partial\eta}\right]_{\eta=1,\nu} = 0 \tag{A22}$$

$$\frac{\partial^2 Z_m(K_{mn}\eta)}{\partial\eta^2} = \begin{cases} \frac{2}{\pi}\,(m^2 - K_{mn}^2) & \text{when } \eta = 1 \\ \frac{2}{\nu\pi}\,(\frac{m^2}{\nu^2} - K_{mn}^2)\,\frac{Y_m'(K_{mn})}{Y_m'(K_{mn}\nu)} & \text{when } \eta = \nu \end{cases} \tag{A23}$$

and

$$\int_\nu^1 \eta Z_m^{\,2}(K_{mn}\eta)\,d\eta = -\frac{1}{K_{mn}^2}\int_{K_{mn}\nu}^{K_{mn}} S Z_m^{\,2}(S)\,dS = \left[\frac{S^2}{2}\left(\left(1 - \frac{m^2}{S^2}\right)Z_m^{\,2}(S) + Z_m^{\,2}(S)\right)\right]_{K_{mn}\nu}^{K_{mn}} \tag{A24}$$

where $[Z_m'(S)]_{S=K_{mn},K_{mn}\nu} = 0$.

c) Closed Form for Series Expression

By Dini's expansion,

$$\sum_{n=1}^{\infty} \frac{\int_\nu^1 \eta Z_m(K_{mn}\eta)\,d\eta}{\int_\nu^1 \eta Z_m^{\,2}(K_{mn}\eta)\,d\eta}\, Z_m(K_{mn}\eta) = 1, \tag{A25}$$

using Equation (A18), we obtain

$$\sum_{n=1}^{\infty} \frac{\int_{\nu}^{1} \eta Z_m(K_{mn}\eta)\,d\eta}{\int_{\nu}^{1} \eta Z_m^{\,2}(K_{mn}\eta)\,d\eta} = \frac{\pi}{2} . \tag{A26}$$

The tangential and radial velocity components due to a single radial vortex line and also the axial velocity component due to a single radial source line are zero at $\zeta = 0$.

$$(u_{v\theta})_{\zeta=0} = \mp \frac{\Gamma}{4\eta\pi} \left(1+2 \sum_{m=1}^{\infty} \cos m\theta \sum_{n=1}^{\infty} \frac{\int_{\nu}^{1} \eta Z_m(K_{mn}\eta)\,d\eta}{\int_{\nu}^{1} \eta\, Z_m^{\,2}(K_{mn}\eta)\,d\eta} Z_m(K_{mn}\eta)\right) = 0 , \tag{A27}$$

$$(u_{v\eta})_{\zeta=0} = \mp \frac{\Gamma}{2\pi} \sum_{m=1}^{\infty} \frac{\sin m\theta}{m} \sum_{n=1}^{\infty} \frac{\int_{\nu}^{1} \eta Z_m(K_{mn}\eta)\,d\eta}{\int_{\nu}^{1} \eta Z_m^{\,2}(K_{mn}\eta)\,d\eta} \frac{\partial Z_m(K_{mn}\eta)}{\partial \eta} = 0 \tag{A28}$$

and

$$(u_{S\zeta})_{\zeta=0} = \frac{1}{4\pi} \left(\pm \frac{2}{1-\nu^2} \int_{\nu}^{1} Q(\eta)\,d\eta \pm \sum_{n=2}^{\infty} \frac{\int_{\nu}^{1} Q(\eta) Z_o(K_{on}\eta)\,d\eta}{\int_{\nu}^{1} \eta Z_o^{\,2}(K_{on}\eta)\,d\eta} Z_o(K_{on}\eta)\right.$$

$$\left. \pm 2 \sum_{m=1}^{\infty} \cos m\theta \sum_{n=1}^{\infty} \frac{\int_{\nu}^{1} Q(\eta) Z_m(K_{mn}\eta)\,d\eta}{\int_{\nu}^{1} \eta Z_m^{\,2}(K_{mn}\eta)\,d\eta} Z_m(K_{mn}\eta)\right) = 0 \tag{A29}$$

The tangential and radial velocity components due to a single radial vortex line of constant strength should have an inflection point at $\zeta = 0$; then,

$$\left[\frac{\partial^2 u_{v\theta}}{\partial \zeta^2}\right]_{\zeta=0} = \mp \frac{\Gamma}{2\pi\eta} \sum_{m=1}^{\infty} \cos m\theta \sum_{n=1}^{\infty} K_{mn}^2 \frac{\int_{\nu}^{1} \eta Z_m(K_{mn}\eta)\, d\eta}{\int_{\nu}^{1} \eta Z_m^2(K_{mn}\eta)\, d\eta} Z_m(K_{mn}\eta) = 0 \tag{A30}$$

and

$$\left[\frac{\partial^2 u_{v\eta}}{\partial \zeta^2}\right]_{\zeta=0} = \mp \frac{\Gamma}{2\pi} \sum_{m=1}^{\infty} \frac{\sin m\theta}{m} \sum_{n=1}^{\infty} K_{mn}^2 \frac{\int_{\nu}^{1} \eta Z_m(K_{mn}\eta)\, d\eta}{\int_{\nu}^{1} \eta Z_m^2(K_{mn}\eta)\, d\eta} \cdot \frac{\partial Z_m(K_{mn}\eta)}{\partial \eta} = 0 . \tag{A31}$$

Also, the axial velocity component due to a single radial vortex line of constant strength has a maximum value at $\zeta = 0$; then,

$$\left[\frac{\partial u_{v\zeta}}{\partial \zeta}\right]_{\zeta=0} = \mp \frac{\Gamma}{2\pi} \sum_{m=1}^{\infty} \frac{\sin m\theta}{m} \sum_{n=1}^{\infty} K_{mn}^2 \frac{\int_{\nu}^{1} \eta Z_m(K_{mn}\eta)\, d\eta}{\int_{\nu}^{1} \eta Z_m^2(K_{mn}\eta)\, d\eta} \cdot Z_m(K_{mn}) = 0 . \tag{A32}$$

Similarly, for the three-dimensional flow field due to a single radial source line of variable strength, the tangential and radial velocity components have a maximum value at $\zeta = 0$; then,

$$\left[\frac{\partial u_{S\theta}}{\partial \zeta}\right]_{\zeta=0} = \mp \frac{1}{2\pi\eta} \sum_{m=1}^{\infty} m \sin m\theta \sum_{n=1}^{\infty} \frac{\int_{\nu}^{1} Q(\eta) Z_m(K_{mn}\eta)\, d\eta}{\int_{\nu}^{1} \eta Z_m^2(K_{mn}\eta)\, d\eta} \cdot Z_m(K_{mn}\eta)\, d\eta = 0 \tag{A33}$$

and

$$\left[\frac{\partial u_{S\eta}}{\partial \zeta}\right]_{\zeta=0} = -\frac{1}{4\pi}\left(\mp \sum_{n=2}^{\infty} \frac{\int_{\nu}^{1} Q(\eta) Z_o(K_{on}\eta)\,d\eta}{\int_{\nu}^{1} \eta Z_o^{\,2}(K_{on}\eta)\,d\eta} \frac{\partial Z_o(K_{on}\eta)}{\partial \eta}\right.$$

$$\left. \pm 2 \sum_{m=1}^{\infty} \cos m\theta \sum_{n=1}^{\infty} \frac{\int_{\nu}^{1} Q(\eta) Z_m(K_{mn}\eta)\,d\eta}{\int_{\nu}^{1} \eta Z_m^{\,2}(K_{mn}\eta)\,d\eta} \frac{\partial Z_m(K_{mn}\eta)}{\partial \eta}\right) = 0 . \qquad \text{(A34)}$$

The axial velocity component has an inflection point at $\zeta = 0$; then,

$$\left[\frac{\partial^2 u_{S\zeta}}{\partial \zeta^2}\right]_{\zeta=0} = \frac{1}{4\pi}\left(\mp \sum_{n=2}^{\infty} K_{on} \frac{\int_{\nu}^{1} Q(\eta) Z_o(K_{on}\eta)\,d\eta}{\int_{\nu}^{1} \eta Z_o^{\,2}(K_{on}\eta)\,d\eta} Z_o(K_{on}\eta)\right.$$

$$\left. \mp 2 \sum_{m=1}^{\infty} \cos m\theta \sum_{n=1}^{\infty} K_{mn} \frac{\int_{\nu}^{1} Q(\eta) Z_m(K_{mn}\eta)\,d\eta}{\int_{\nu}^{1} \eta Z_m^{\,2}(K_{mn}\eta)\,d\eta} Z_m(K_{mn}\eta)\right) = 0 . \qquad \text{(A35)}$$

# APPENDIX D

## Approximate Formula for the Solution of the Three-Dimensional Flow Field

The solutions of the three-dimensional flow field due to a single radial vortex line and source line include series summations of Bessel functions and trigonometric functions and are quite complicated. A modification of the three-dimensional solutions will be attempted here. The qualitative behavior of the three-dimensional flow field is similar to the two-dimensional unrolled solution. The perturbed velocities are approximately identical for both two-dimensional and three-dimensional cases at mid radius for any hub-to-tip ratio. Rossow (3) suggested the use of Taylor expansion for the exact solution of the three-dimensional flow field due to a single radial vortex line as an approximate formula valid for hub-to-tip ratios close to unity. However, this approximate formula may not be valid for small hub-to-tip ratios because of the assumption made in the process of the Taylor expansion. In the process of calculating the three-dimensional flow field, duplicate calculations are required in order to superimpose the effects of the vortex and source lines. Once the basic solutions are obtained, the superposition of the flow field for several vortex and source lines involves only simple algebraic equations. Therefore, if the basic solutions are represented by simple approximate formula based on numerical results of the basic solutions, these approximate formula are valid for any calculation for the same hub-to-tip ratio. Several approximate formulations are suggested below:

a) Approximate velocity potential and velocity components due to a single radial vortex line of constant strength

$$(\Phi_v)_{ap} = -\frac{\Gamma}{2\pi} \tan^{-1} \frac{\tan \theta/2}{\tanh B\zeta}, \tag{A36}$$

$$(u_{v\theta})_{ap} = -\frac{\Gamma}{4\pi\eta} \frac{\sinh 2B\zeta}{\cosh 2B\zeta - \cos \theta}, \tag{A37}$$

$$(u_{v\eta})_{ap} = -\frac{\Gamma}{2\pi} \frac{B' \zeta \sin \theta}{\cosh 2B\zeta - \cos \theta} \tag{A38}$$

and

$$(u_{v\zeta})_{ap} = \frac{\Gamma}{2\pi} \frac{B \sin \theta}{\cosh 2B\zeta - \cos \theta}, \tag{A39}$$

where $B = B(\eta)$, $B' = \partial B(\eta)/\partial\eta$. These are similar to the two-dimensional unrolled solutions except for the radial velocity (see Appendix E). The functional behavior of the approximate formula are found to be quite similar to the three-dimensional exact solutions. The approximate tangential and radial velocity components have the same limiting values at $\zeta \to \pm 0$ and $\zeta \to \pm \infty$ as the three-dimensional exact solutions. Also, the approximate tangential and radial velocity components have inflection points at $\zeta = 0$ and the axial velocity component has a maximum at $\zeta = 0$. However, the functions $B(\eta)$ and $B'(\eta)$ are unknown. But, from numerical results of the exact solution at the particular $\eta$ and $\theta$, the values $B(\eta)$ and $B'(\eta)$ in Equations (A37), (A38) and (A39) can be determined. The development of these approximate solutions is planned for the future.

b) Approximate velocity potential and velocity components due to a single radial source line of constant strength:

The approximate formula for the three-dimensional flow field due to a single radial source line of variable strength can be written as

$$(\Phi_S)_{ap} = \frac{Q}{4\pi(1+\nu)C} \ln\left(2(\cosh 2C\zeta - \cos\theta)\right), \tag{A40}$$

$$(u_{S\theta})_{ap} = \frac{Q}{4\pi(1+\nu)C\eta} \frac{\sin\theta}{\cosh 2C\zeta - \cos\theta}, \tag{A41}$$

$$(u_{S\eta})_{ap} = -\frac{Q\,C'}{4\pi(1+\nu)C}\left(1 + \frac{1}{C}\ln(2(\cosh 2C\zeta - \cos\theta)) - \frac{2\zeta\ \sinh 2C\zeta}{\cosh 2C\zeta - \cos\theta}\right) \tag{A42}$$

and

$$(u_{S\zeta})_{ap} = \frac{Q}{2\pi(1+\nu)} \frac{\sin 2C\zeta}{\cosh 2C\zeta - \cos\theta}, \tag{A43}$$

where $C = C(\eta)$, $C' = \partial C(\eta)/\partial\eta$, and $C = 1/2\eta$ correspond to the two-dimensional unrolled solutions (see Appendix E). Again, the functions $C(\eta)$ and $C'(\eta)$ are unknown, similar to the vortex system. These quantities will be determined for fixed $\eta$ and $\theta$. The values $C(\eta)$ and $C'(\eta)$ so derived are valid for the estimation of the velocity components along the $\zeta$ axis for particular $\eta$, $\theta$, $\nu$. Values of B, B', C and C' of the present formula, whose functional behavior are quite similar to the corresponding exact solutions, will be determined by using the exact numerical results at a few points for particular $\eta$, $\theta$ and $\zeta$. Then, the approximate velocity components at any $\zeta$ coordinate can be easily determined.

# APPENDIX E

## Two-Dimensional Unrolled Solution

The velocity potential due to a vortex of strength $\Gamma$ and a source of strength Q located at $\zeta = 0$ and $\theta = 0$ are given by,

$$\Phi_v = -\frac{\Gamma}{2\pi} \tan^{-1} \frac{\tan \theta/2}{\tanh \zeta/2\eta} \tag{A44}$$

and

$$\Phi_S = \frac{Q}{4\pi} \ell n \left(2(\cosh \zeta/\eta - \cos\theta)\right) . \tag{A45}$$

The corresponding velocity components are:

$$u_{v\theta} = -\frac{\Gamma}{4\pi\eta} \frac{\sinh \zeta/\eta}{\cosh \zeta/\eta - \cos \theta}, \tag{A46}$$

$$u_{v\zeta} = \frac{\Gamma}{4\pi\eta} \frac{\sin \theta}{\cosh \zeta/\eta - \cos \theta} , \tag{A47}$$

$$u_{S\theta} = \frac{Q}{4\pi\eta} \frac{\sin \theta}{\cosh \zeta/\eta - \cos\theta} \tag{A48}$$

and

$$u_{S\zeta} = \frac{Q}{4\pi\eta} \frac{\sinh \zeta/\eta}{\cosh \zeta/\eta - \cos\theta} , \tag{A49}$$

where the positive direction of $\Gamma$ is based on the right-hand screw rule, and the positive and negative values of Q correspond to a source and sink, respectively. The tangential and axial velocity components due to a series of radial vortex lines of constant strength and due to a series of radial source lines of variable strength replacing the equally spaced blade rows of NB blades are given by,

$$u_{v\theta} = -\sum_{i=1}^{NB}\sum_{j=1}^{JVS} \frac{\Gamma_j}{4\pi\eta\cdot NB} \frac{\sinh\left(\frac{(\zeta-\zeta_j)\cdot NB}{\eta}\right)}{\cosh\left(\frac{(\zeta-\zeta_j)\cdot NB}{\eta}\right) - \cos((\theta-\theta_{i,j})\cdot NB)}, \tag{A50}$$

$$u_{v\zeta} = \sum_{i=1}^{NB}\sum_{j=1}^{JVS} \frac{\Gamma_j}{4\pi\eta\cdot NB} \frac{\sin((\theta-\theta_{i,j})\cdot NB)}{\cosh\left(\frac{(\zeta-\zeta_j)\cdot NB}{\eta}\right) - \cos((\theta-\theta_{i,j})\cdot NB)}, \tag{A51}$$

$$u_{S\theta} = \sum_{i=1}^{NB}\sum_{j=1}^{JVS} \frac{Q_j(\eta)}{4\pi\eta\cdot NB} \frac{\sin((\theta-\theta_{i,j})\cdot NB)}{\cosh\left(\frac{(\zeta-\zeta_j)\cdot NB}{\eta}\right) - \cos((\theta-\theta_{i,j})\cdot NB)}, \tag{A52}$$

and

$$u_{S\zeta} = \sum_{i=1}^{NB}\sum_{j=1}^{JVS} \frac{\bar{Q}_j(\eta)}{4\pi\eta\cdot NB} \frac{\sinh\left(\frac{(\zeta-\zeta_j)\cdot NB}{\eta}\right)}{\cosh\left(\frac{(\zeta-\zeta_j)\cdot NB}{\eta}\right) - \cos((\theta-\theta_{i,j})\cdot NB)}. \tag{A53}$$

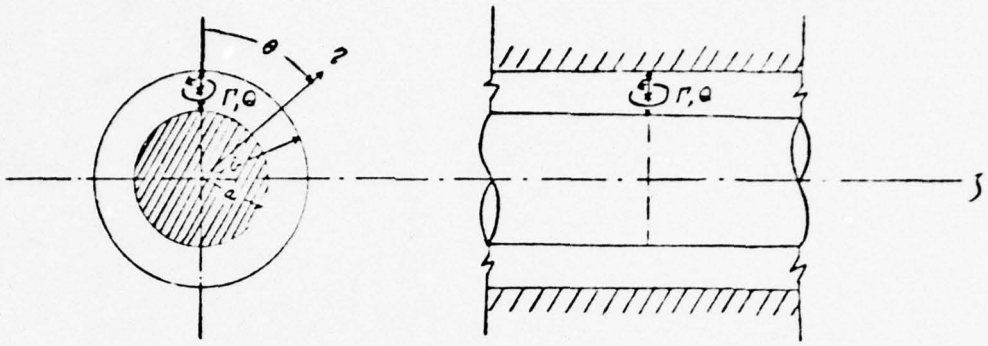


Figure 1 : Single Radial Vortex and Source Line

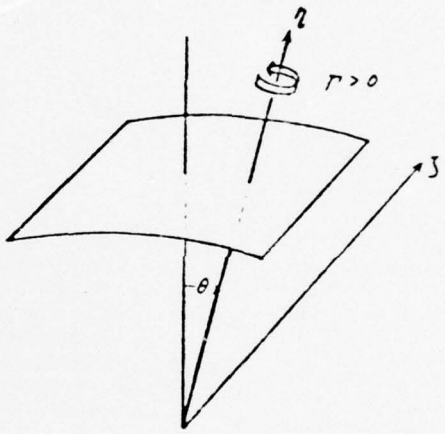


Figure 2: Coordinate System

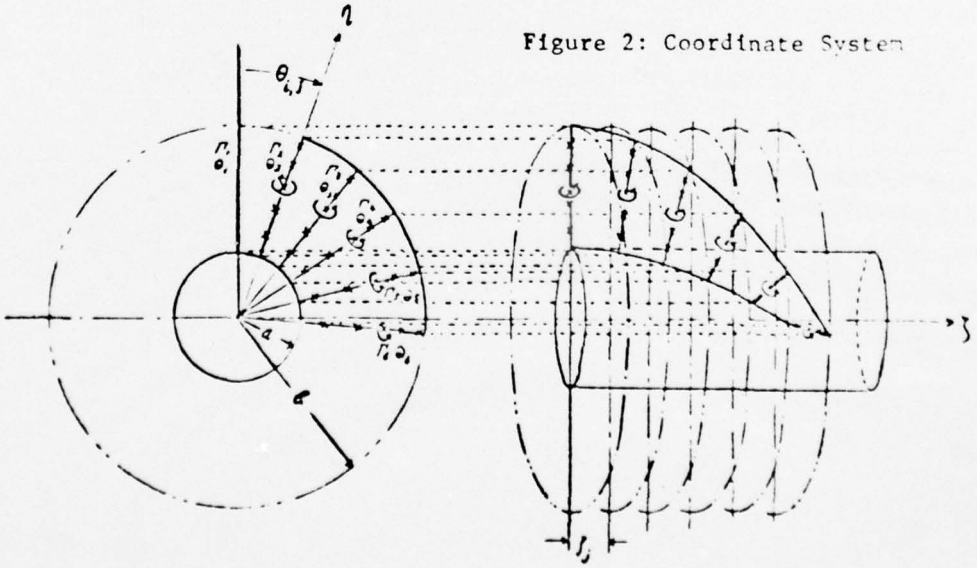


Figure 3: Blade Replaced by Radial Vortex and Source Lines

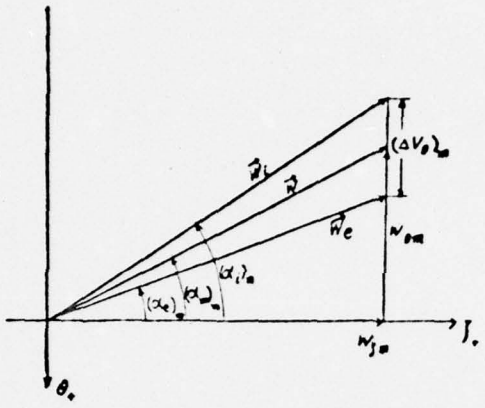

Figure 4: Velocity Triangle at Mid Radius

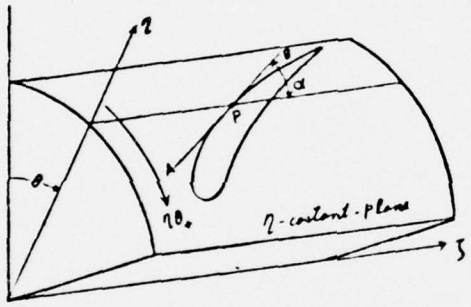

Figure 5a $\eta$-Constant Plane

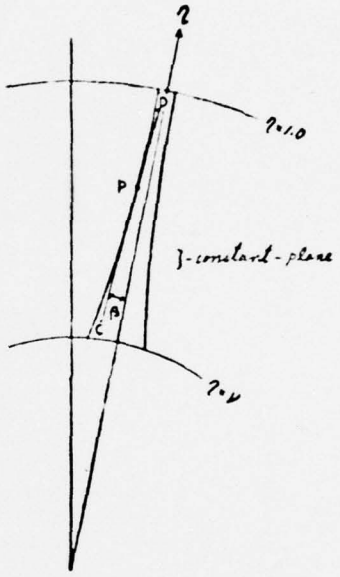

Figure 5b $\zeta$-Constant Plane

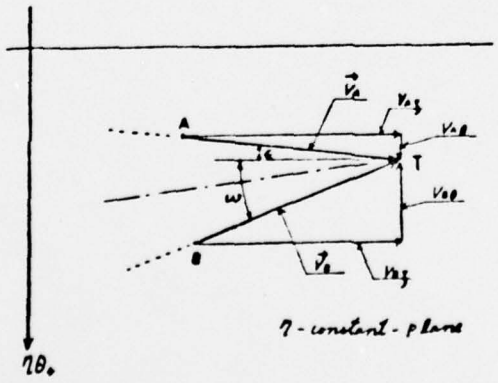

Figure 6: Velocity at the Trailing Edge to Satisfy Kutta-Joukowski's Condition

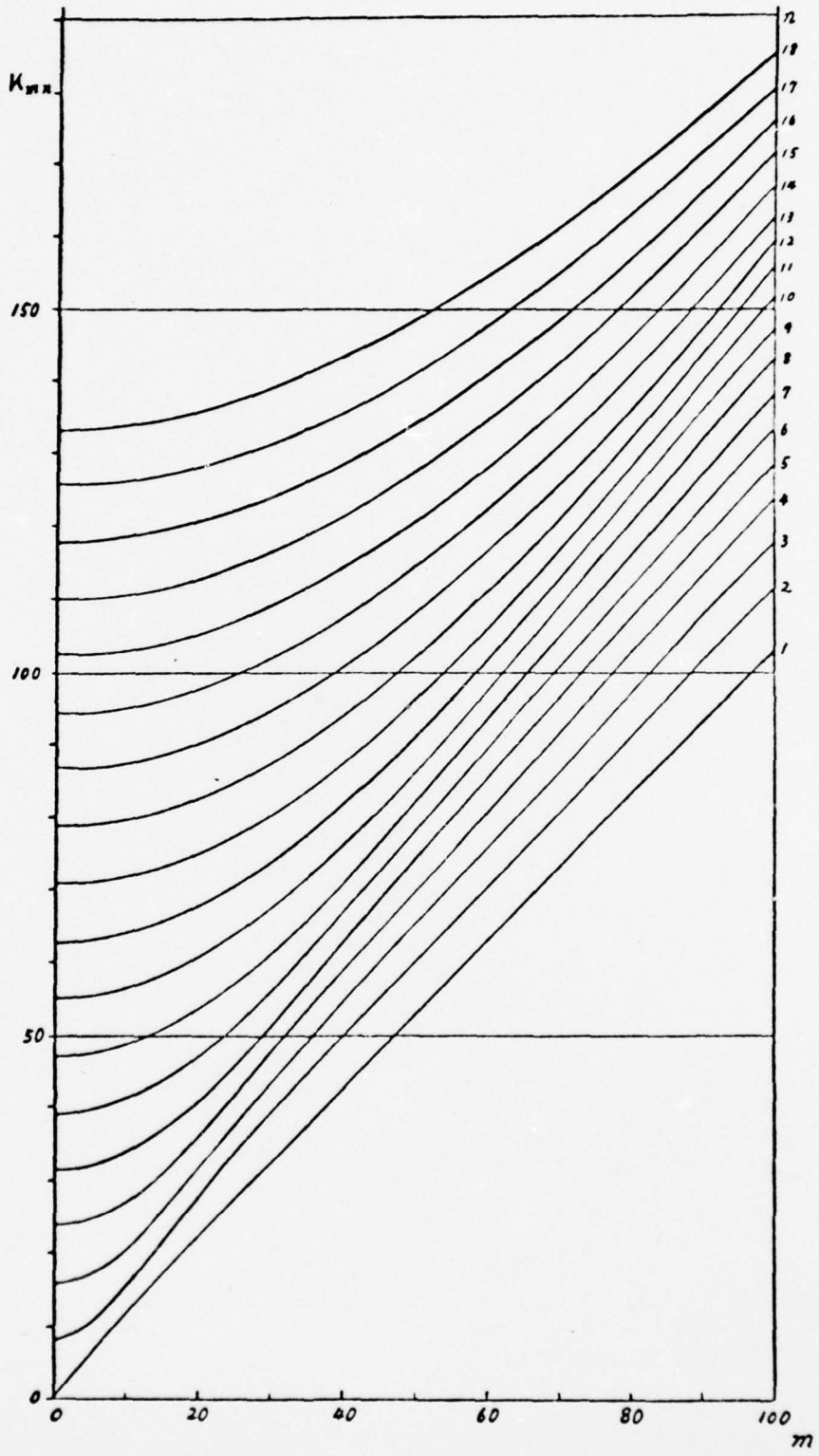


Figure 7 : Eigen Values for $\nu = 0.6$

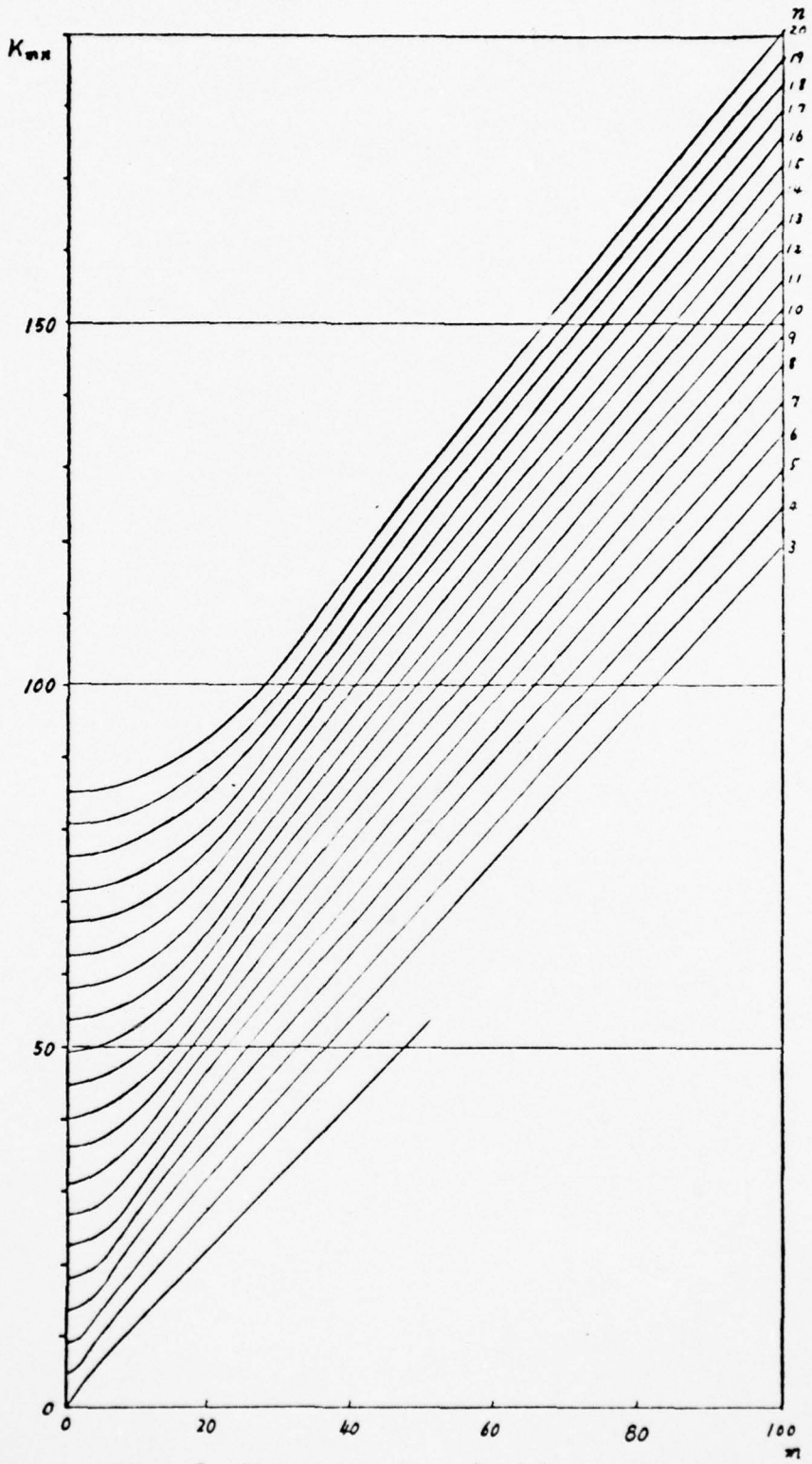


Figure 8 : Eigen Values for $\nu = 0.3$

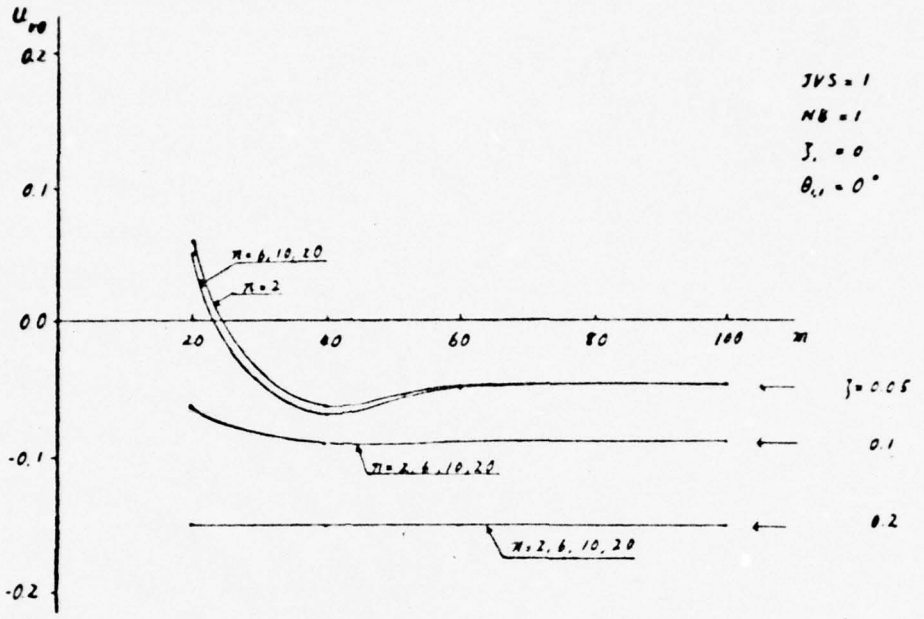


Figure 9: Convergency of $u_{r\theta}$ at $\theta = 30°$, $\zeta = 0.8$ for $\nu = 0.6$

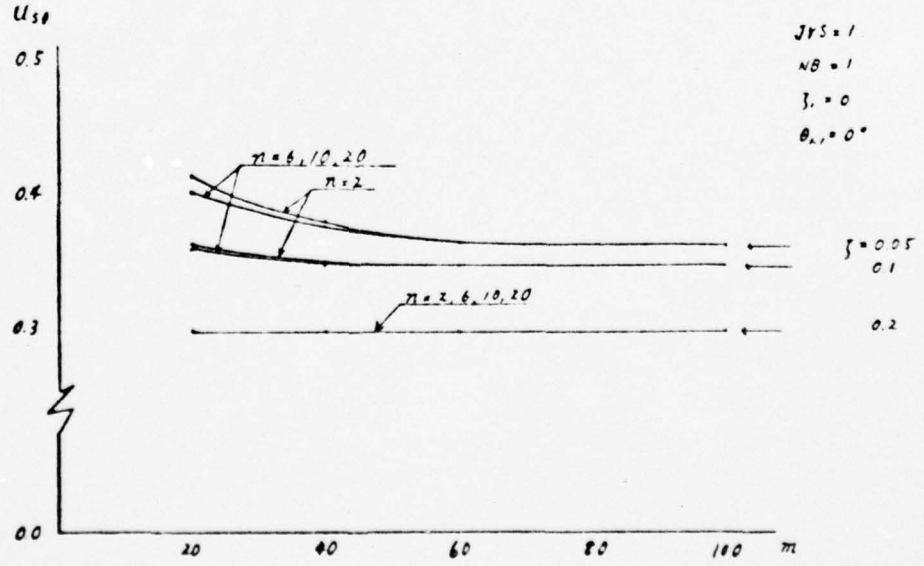


Figure 10: Convergency of $u_{s\theta}$ at $\theta = 30°$, $\zeta = 0.8$ for $\nu = 0.6$

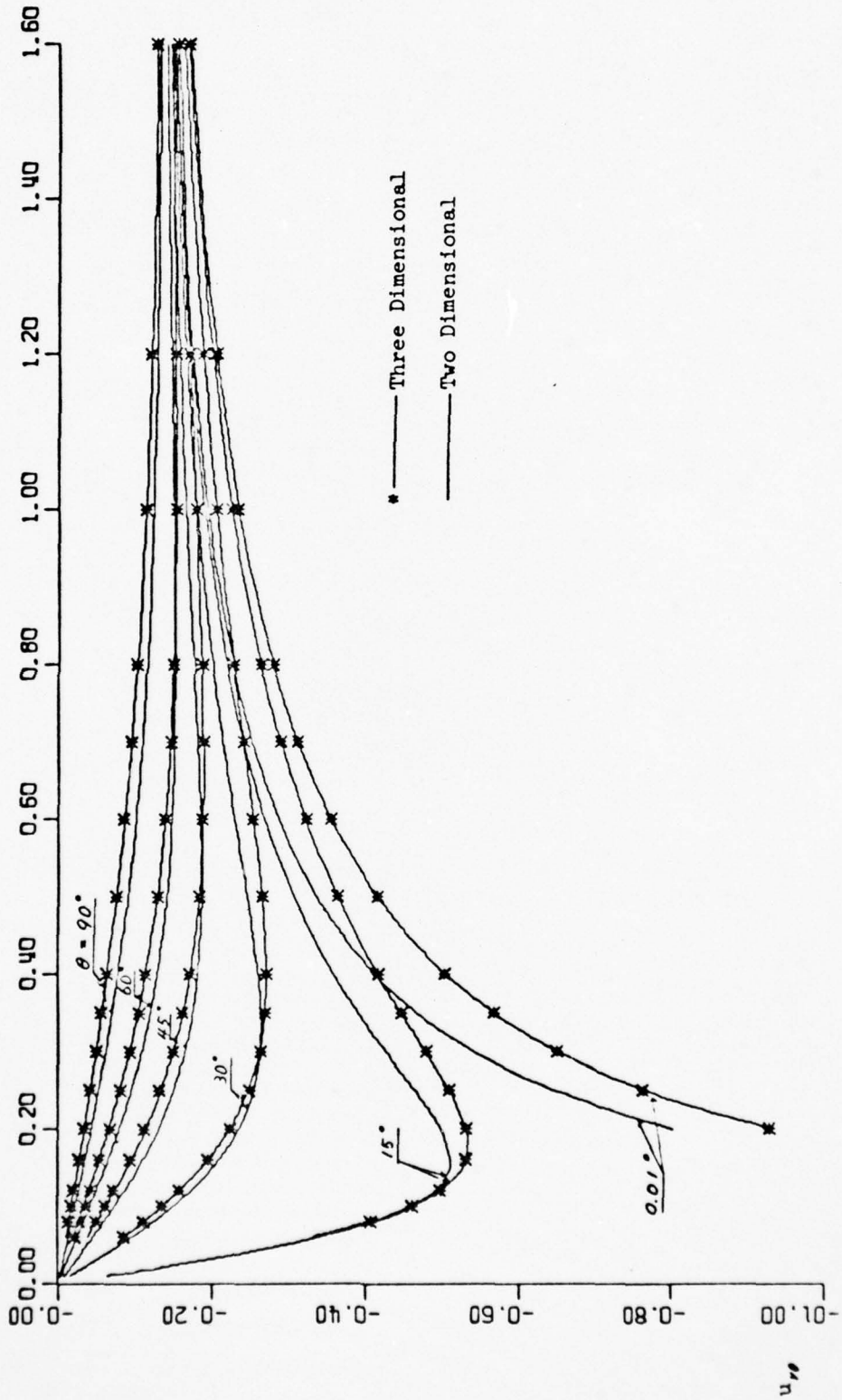


Figure 11: Tangential Velocity Distribution $u_{r,\theta}$ at the Hub($\eta$ = 0.6) due to a Single Radial Vortex Line of Strength Unity for $\nu$ = 0.6

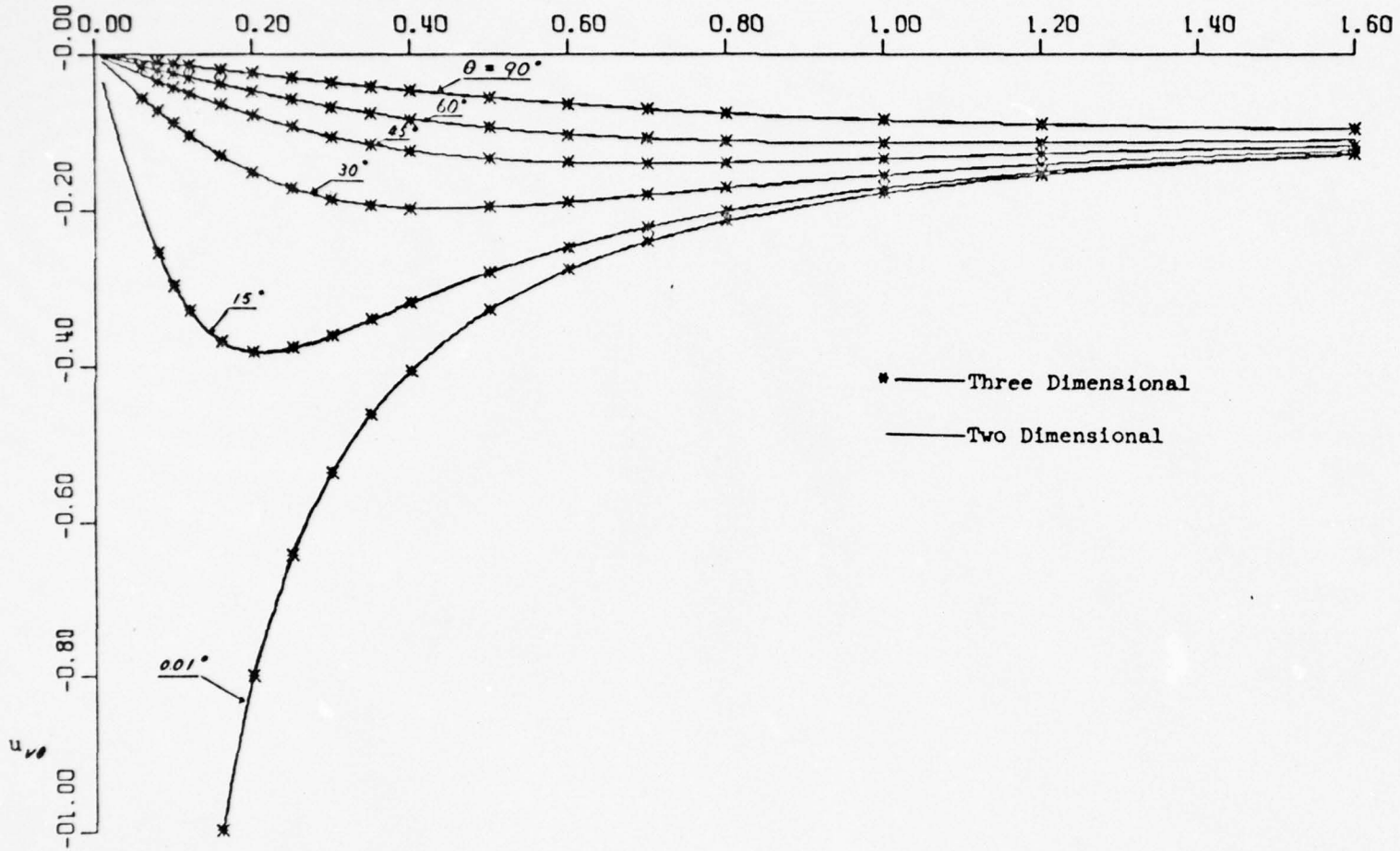


Figure 12: Tangential Velocity Distribution $u_{v\theta}$ at the Mid Radius($\eta$ = 0.8) due to a Single Radial Vortex Line of Strength Unity for $\nu$ = 0.6

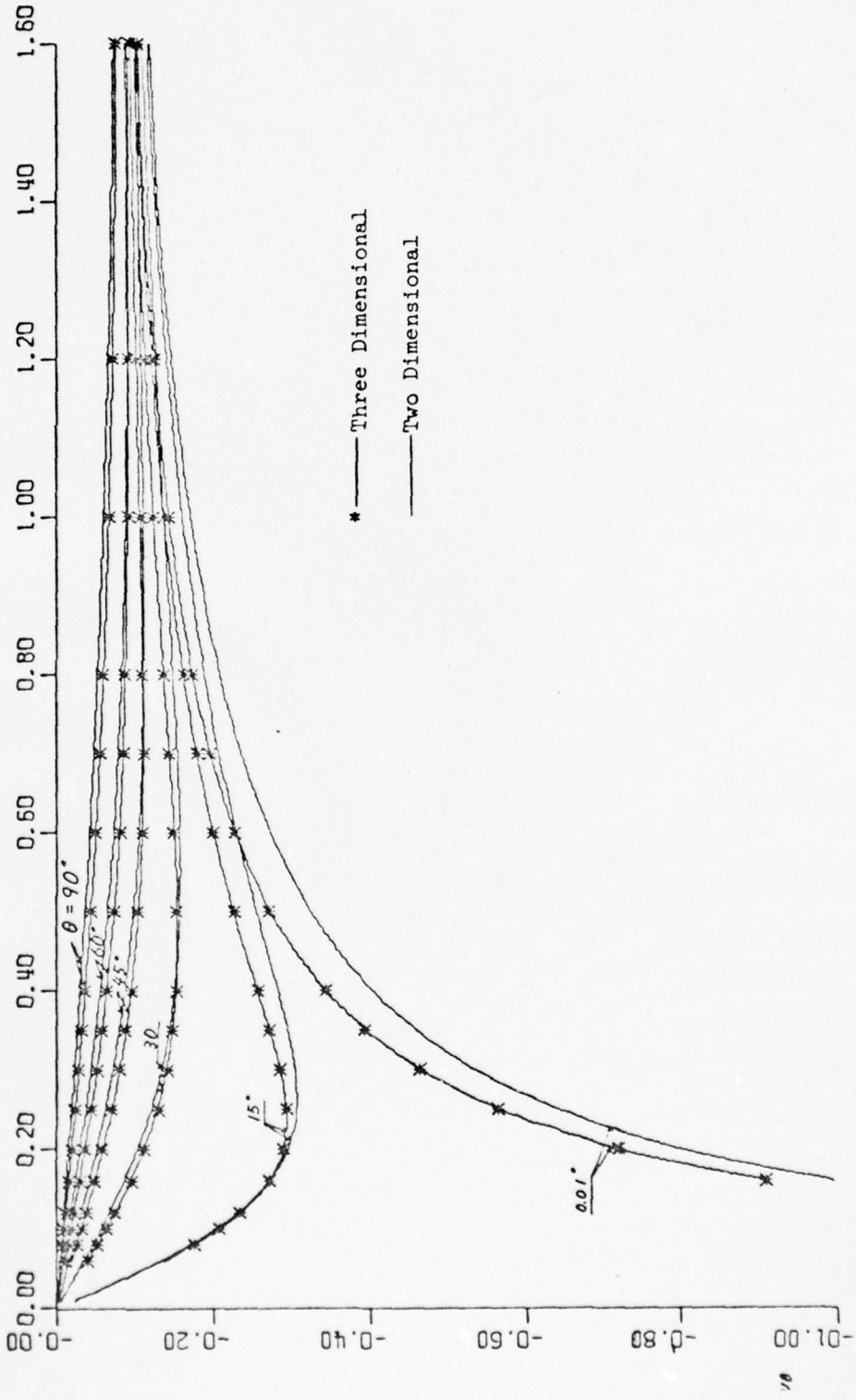


Figure 13: Tangential Velocity Distribution $u_{r\theta}$ at the Tip( $\zeta = 1.0$) due to a Single Radial Vortex line of Strength Unity for $\nu = 0.6$

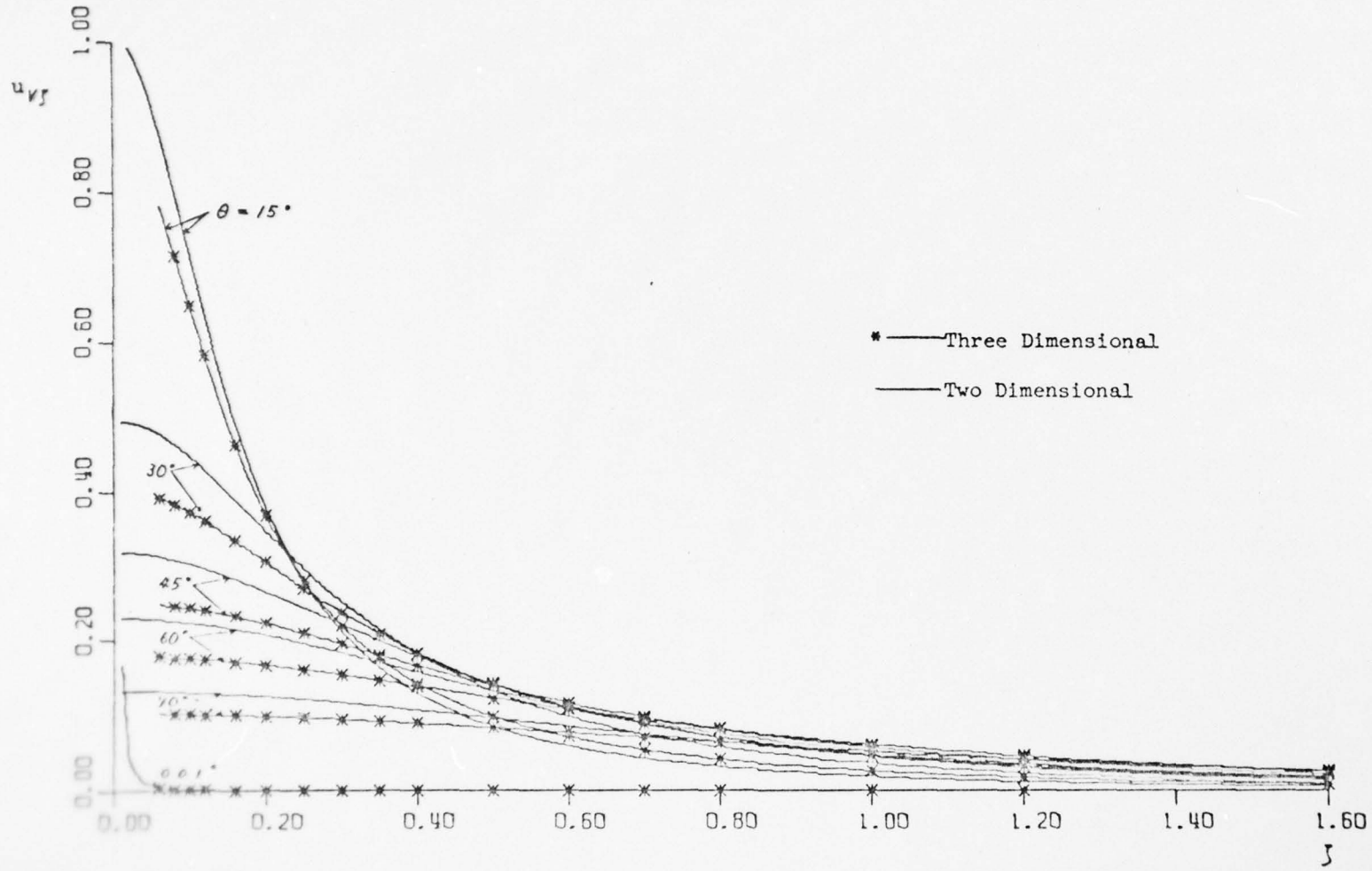


Figure 14: Axial Velocity Distribution $u_{\nu\zeta}$ at the Hub( $\eta = 0.6$) due to a Single Radial Vortex Line of Strength Unity for $\nu = 0.6$

AD-A040 672 PENNSYLVANIA STATE UNIV UNIVERSITY PARK APPLIED RESE--ETC F/G 13/7
THREE DIMENSIONAL INVISCID EFFECTS AND LIMITATIONS OF CASCADE T--ETC(U)
APR 74 A TAMURA
N00017-73-C-1418

UNCLASSIFIED TM-74-78 NL

2 OF 2
AD A040672

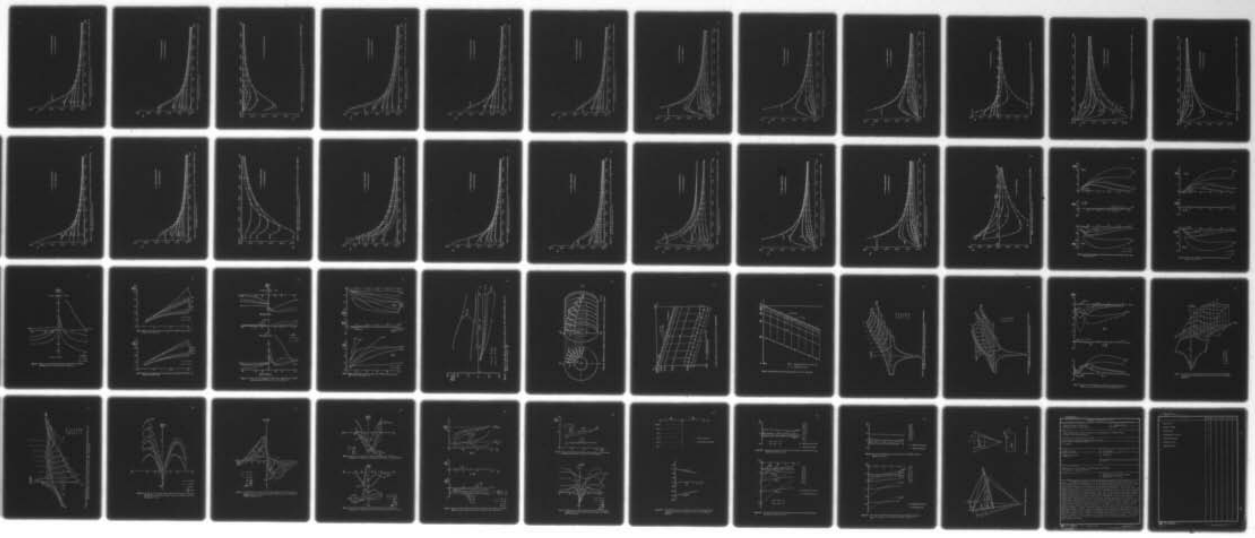

END

DATE FILMED
7-77

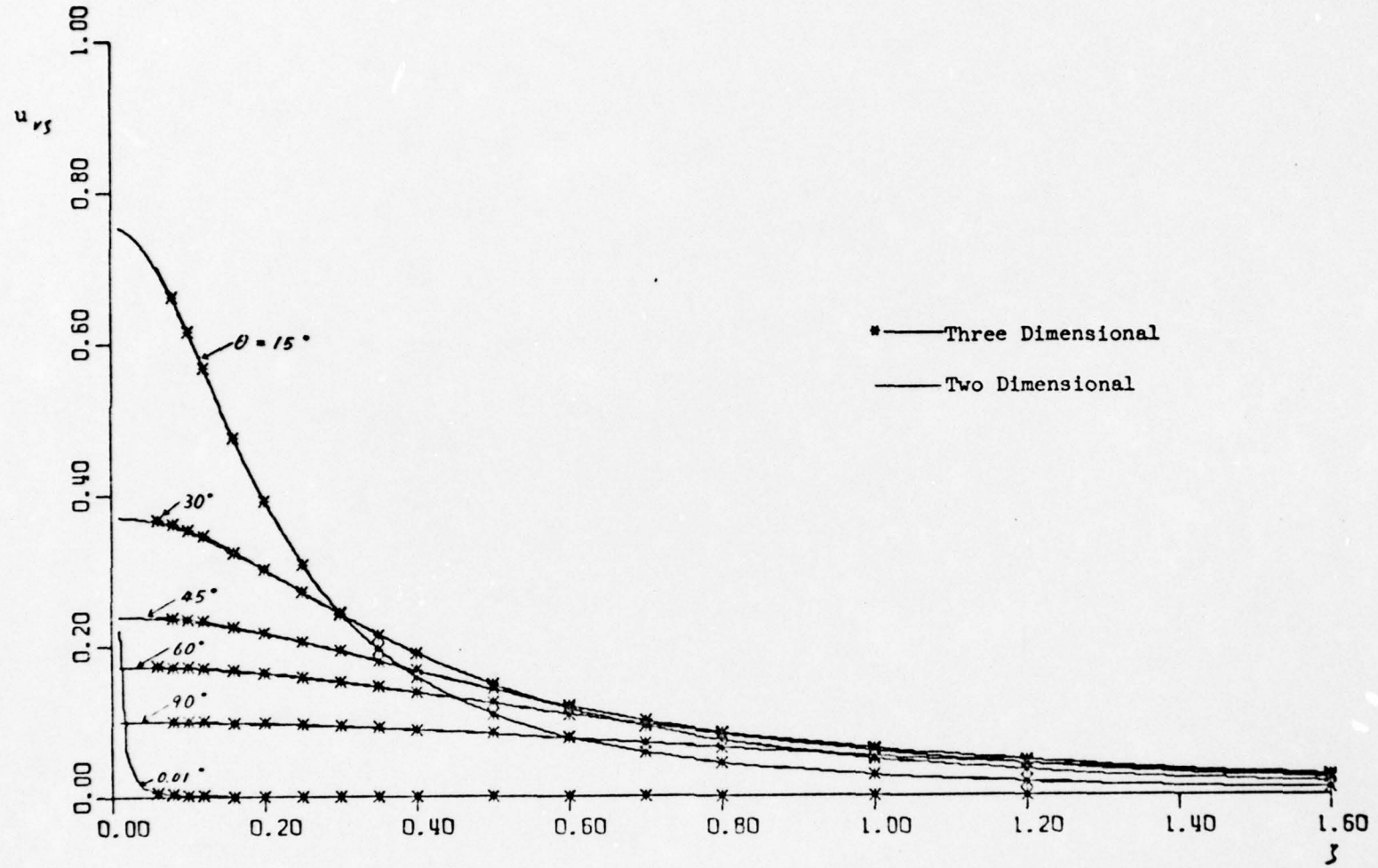


Figure 15: Axial Velocity Distribution $u_{rs}$ at the Mid Radius($\zeta = 0.8$) due to a Single Radial Vortex Line of Strength Unity for $\nu = 0.6$

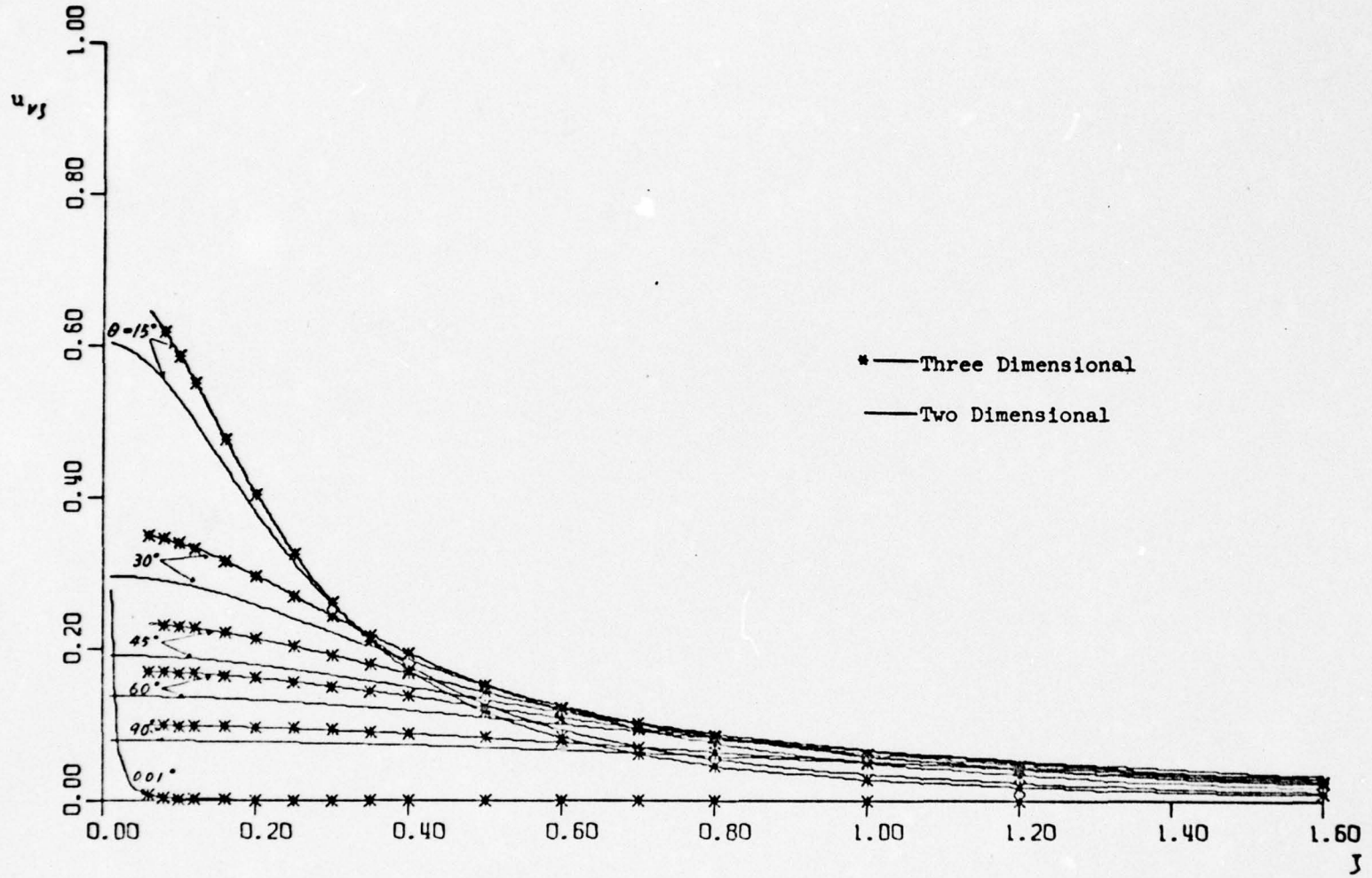


Figure 16: Axial Velocity Distribution $u_{\nu j}$ at the Tip($\eta = 1.0$) due to a Single Radial Vortex Line of Strength Unity for $\nu = 0.6$

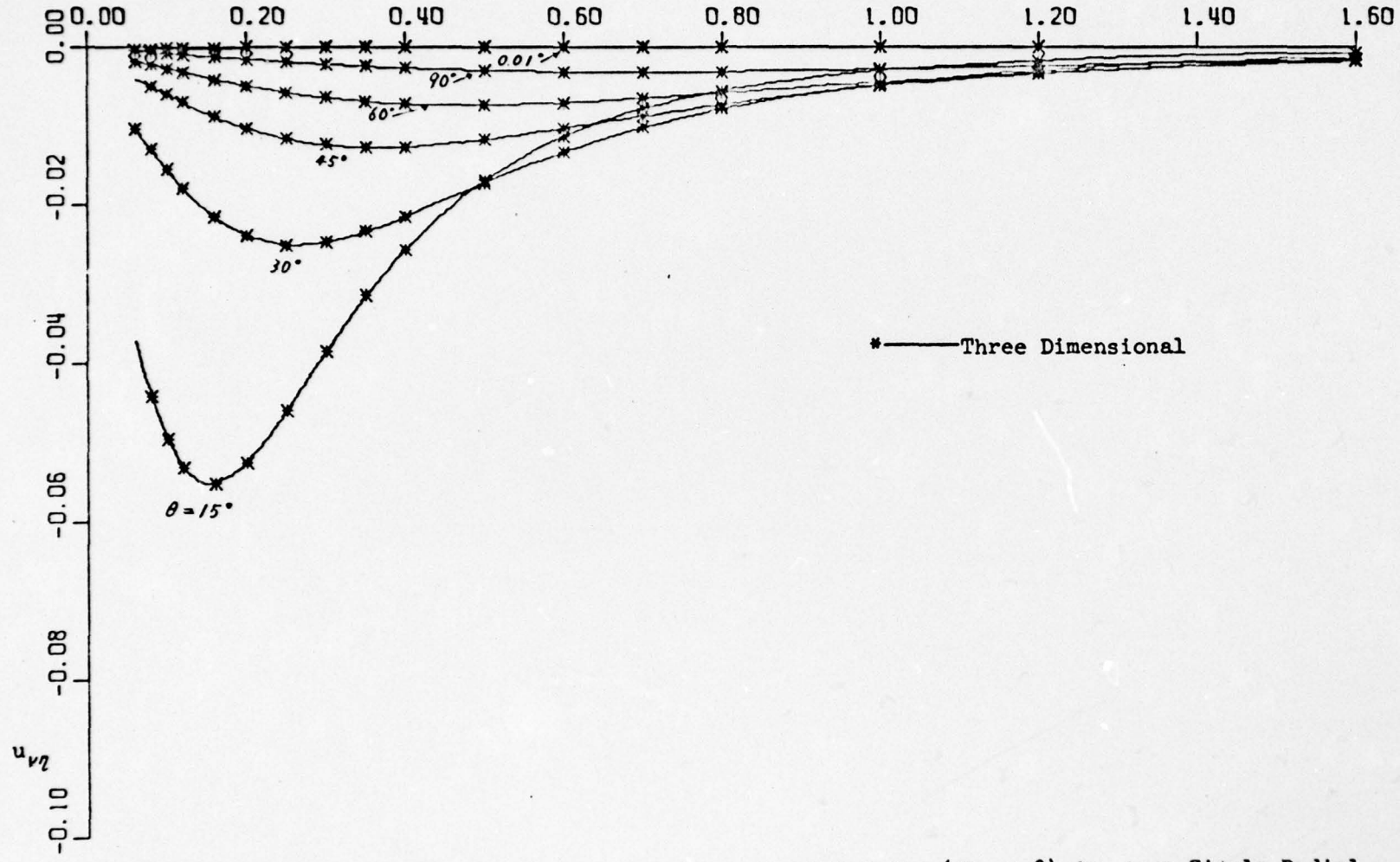


Figure 17: Radial Velocity Distribution $u_{\nu\eta}$ at the Mid Radius($\eta$ = 0.8) due to a Single Radial Vortex Line of Strength Unity for $\nu$ = 0.6

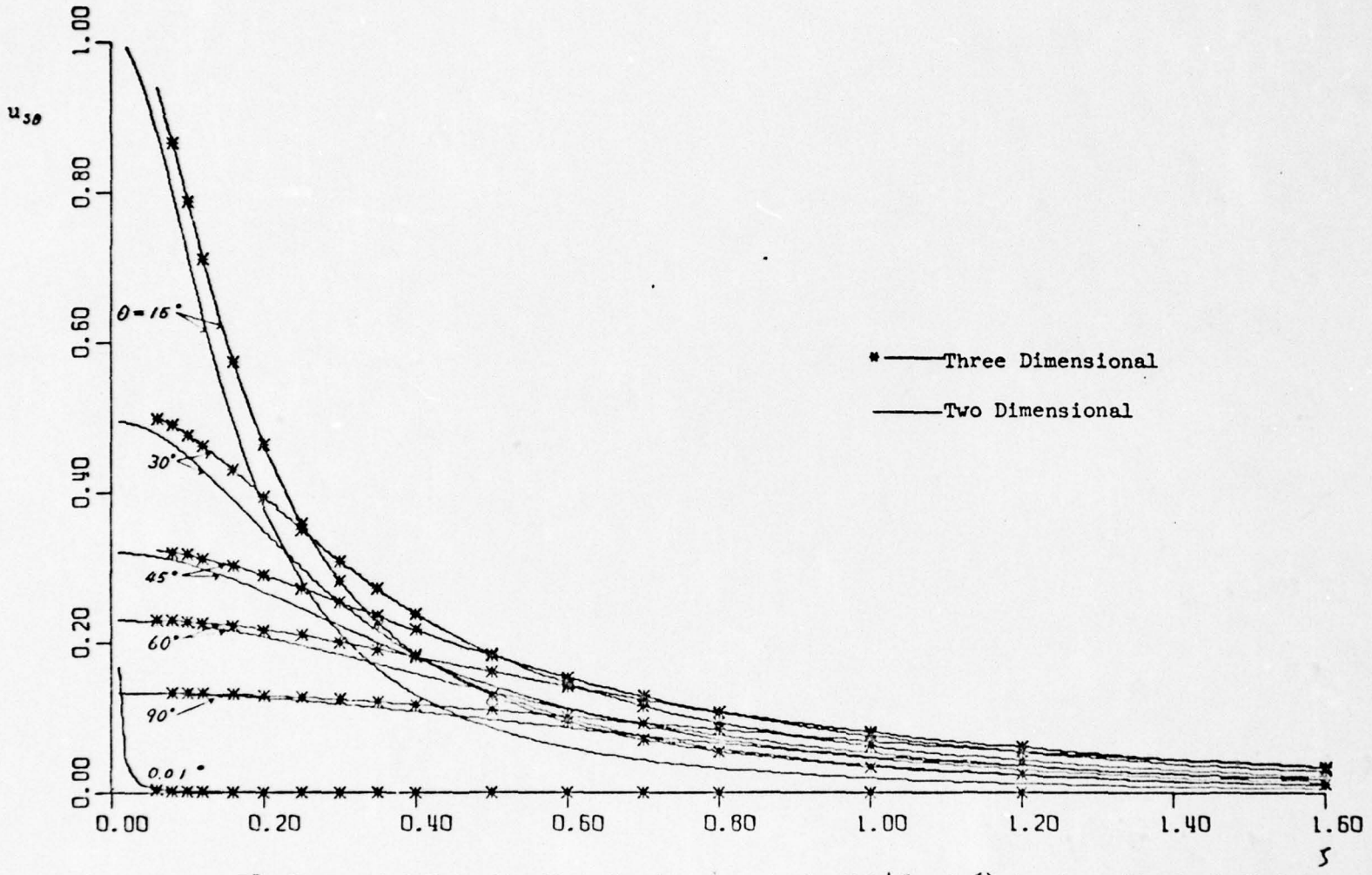


Figure 18: Tangential Velocity Distribution $u_{s\theta}$ at the Hub($\eta = 0.6$) due to a Single Radial Source Line of Strength Unity for $\nu = 0.6$

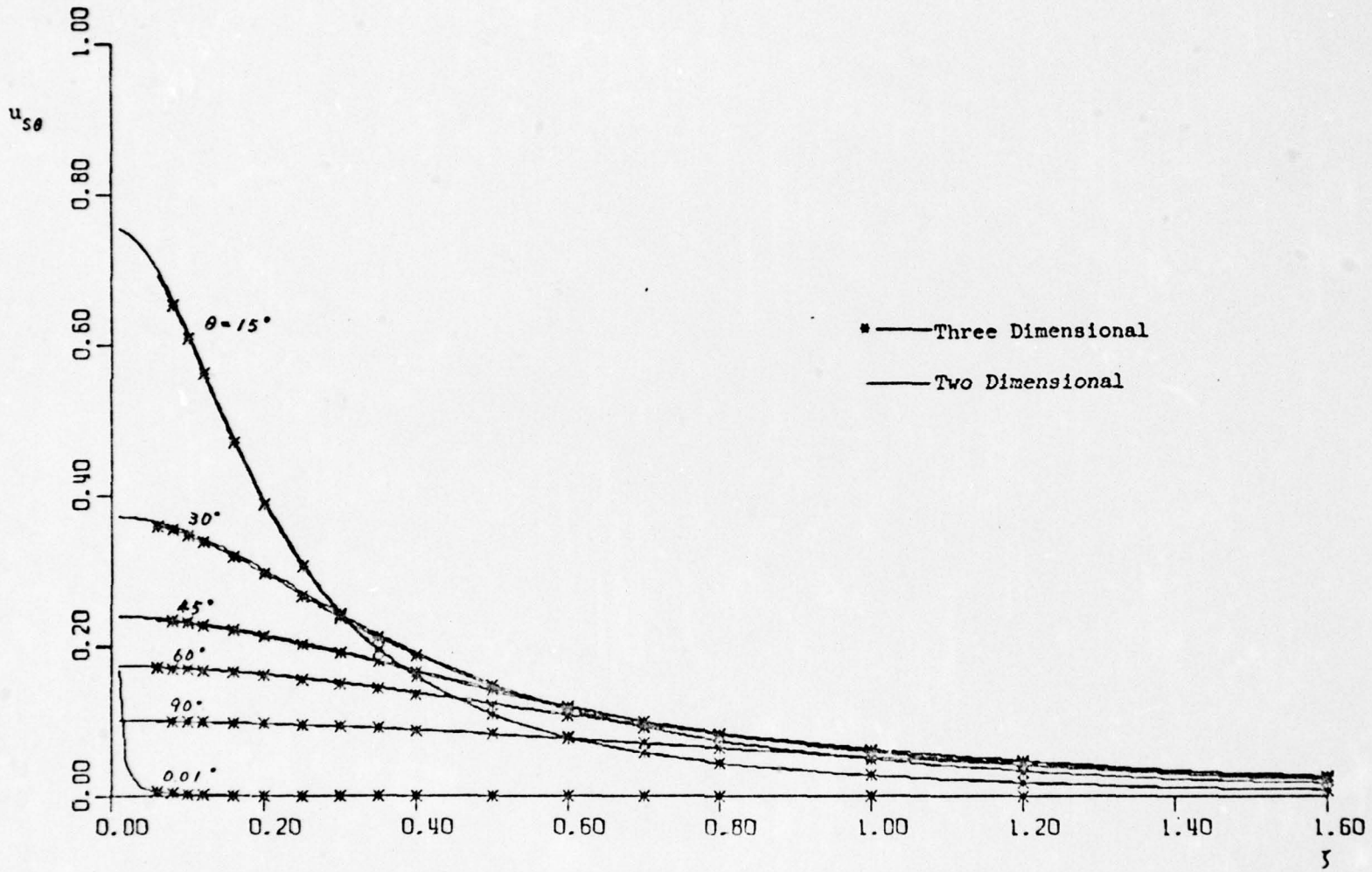


Figure 19: Tangential Velocity Distribution $u_{s\theta}$ at the Mid Radius( $\eta = 0.8$) due to a Single Radial Source Line of Strength Unity for $\nu = 0.6$

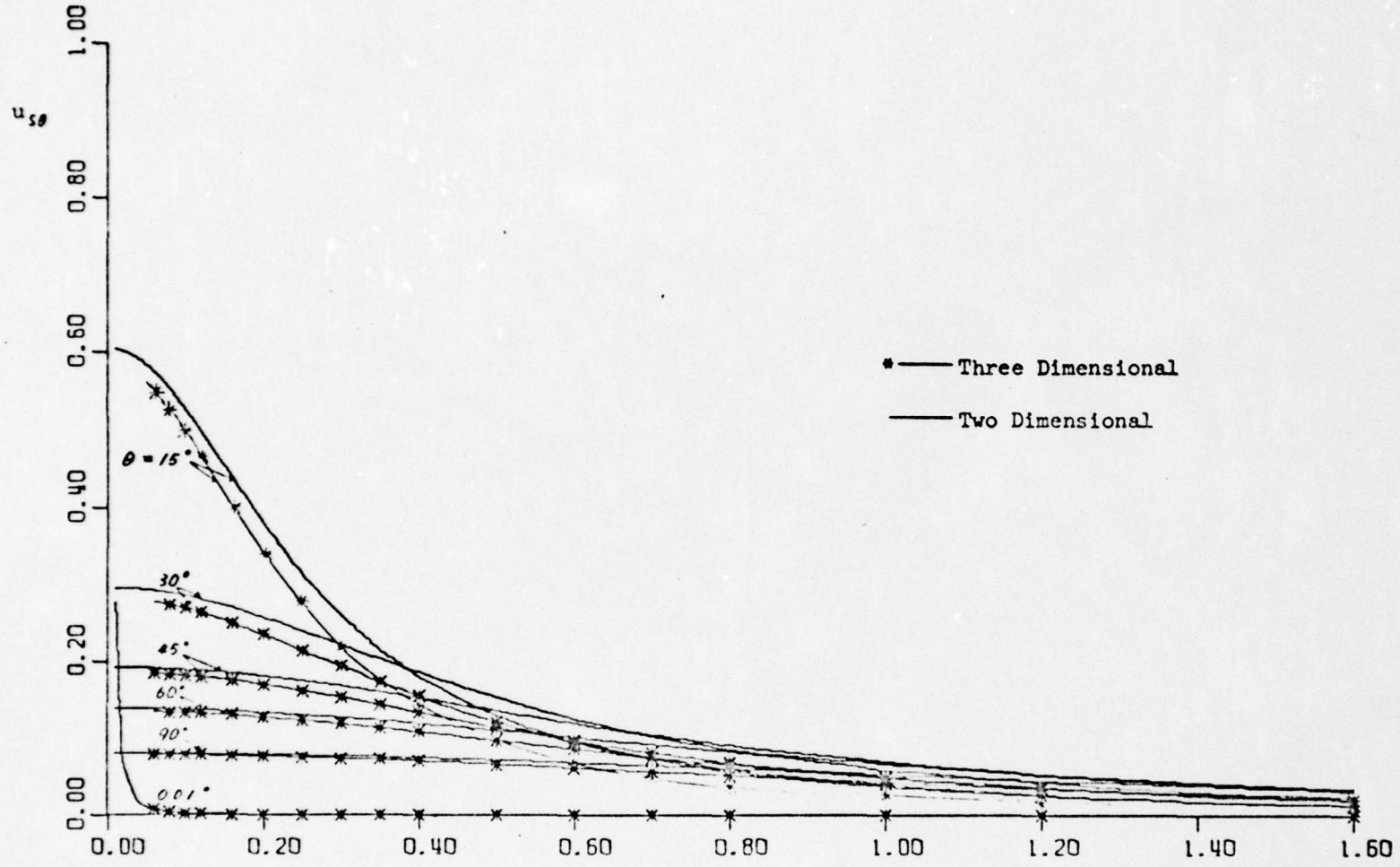


Figure 20: Tangential Velocity Distribution $u_{s\theta}$ at the Tip($\eta = 1.0$) due to a Single radial Source Line of Strength Unity for $\nu = 0.6$

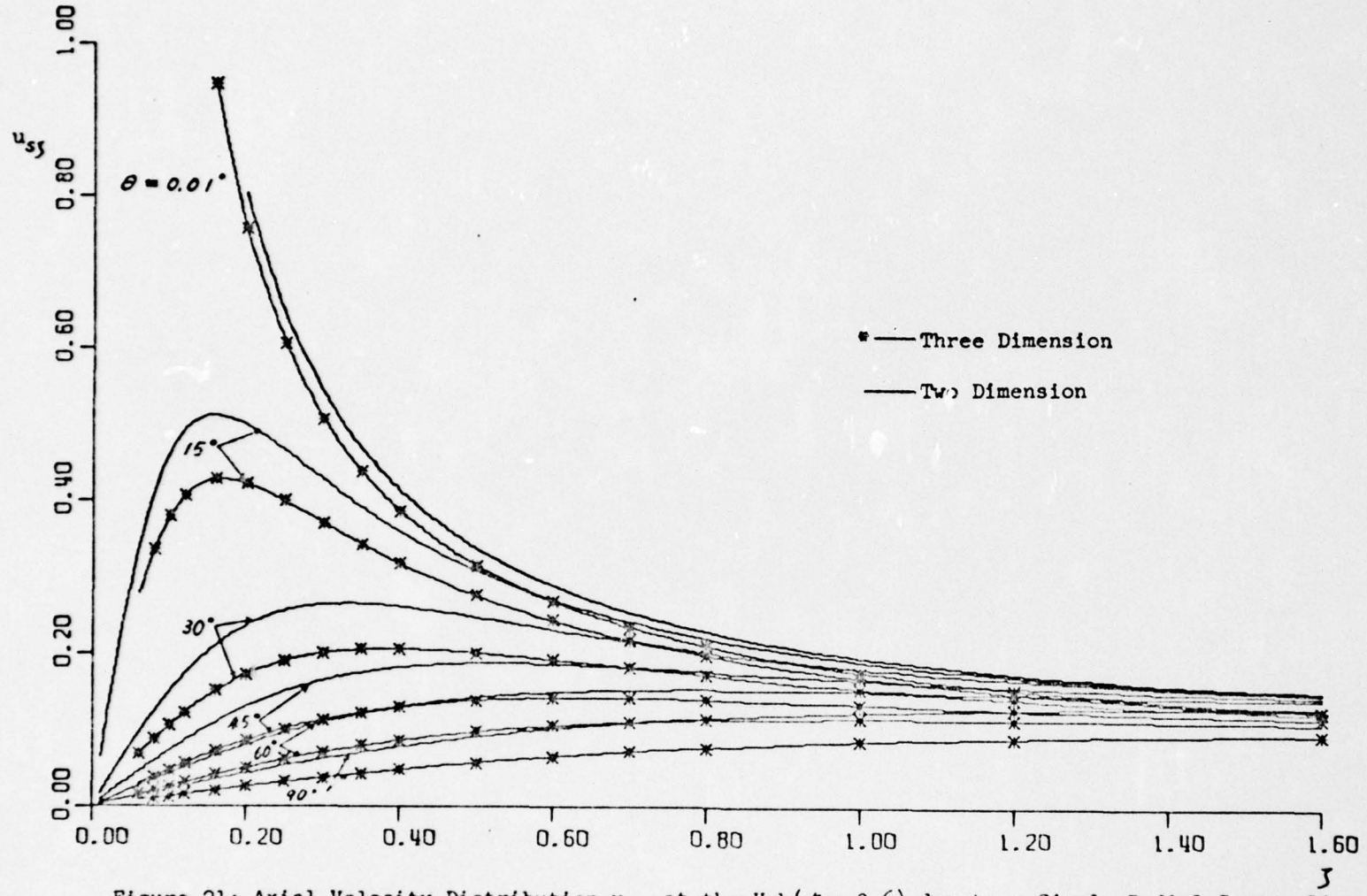


Figure 21: Axial Velocity Distribution $u_{sf}$ at the Hub( $\eta = 0.6$) due to a Single Radial Source Line of Strength Unity for $\nu = 0.6$

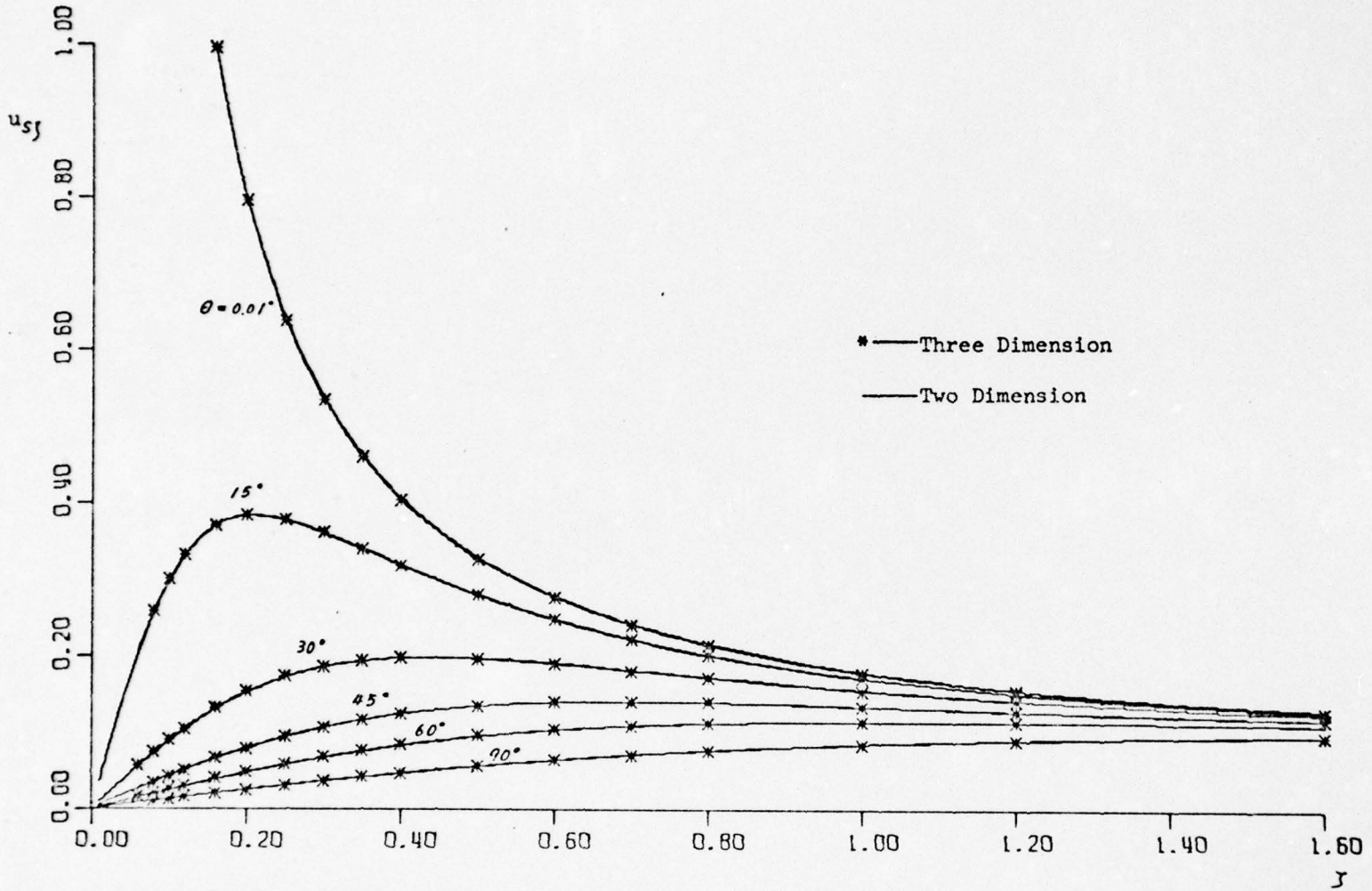


Figure 22: Axial Velocity Distribution $u_{sf}$ at the Mid Radius( $\eta = 0.8$) due to a Single Radial Source Line of Strength Unity for $\nu = 0.6$

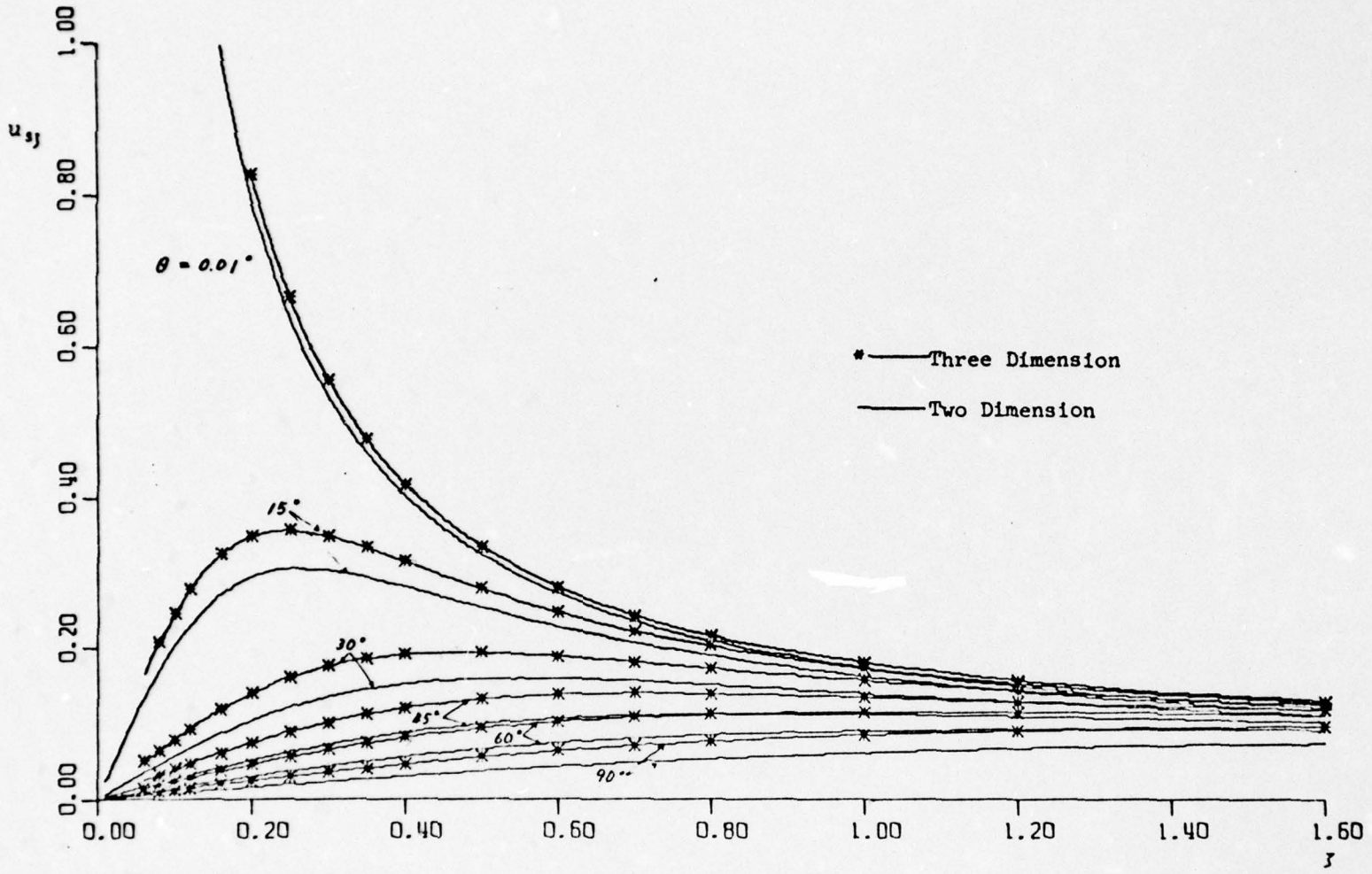


Figure 23: Axial Velocity Distribution $u_{sj}$ at the Tip( $\eta = 1.0$) due to a Single Radial Source Line of Strength Unity for $\nu = 0.6$

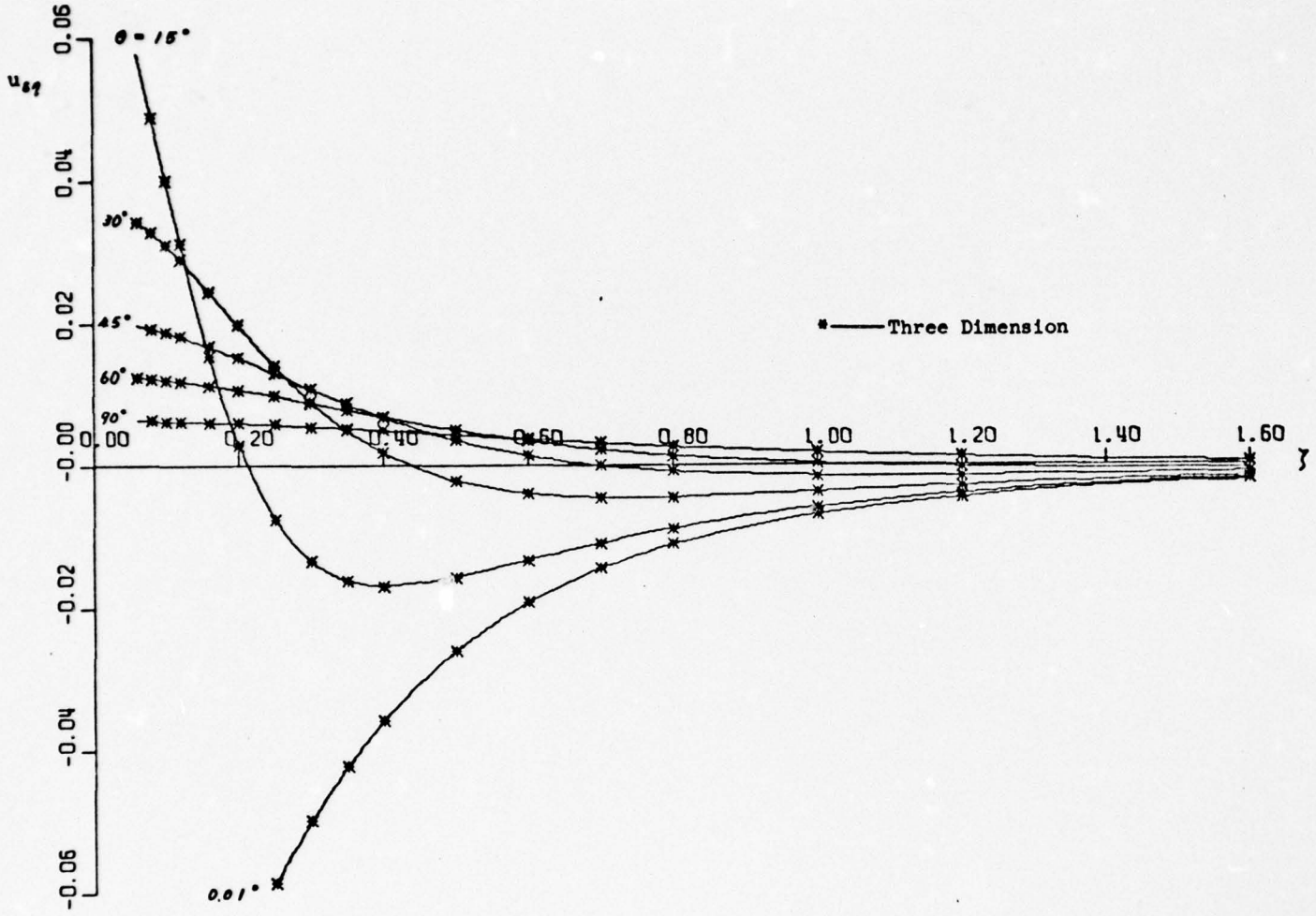


Figure 24: Radial Velocity Distribution $u_{sq}$ at the Mid Radius( $\eta = 0.8$) due to a Single Radial Source Line of Strength Unity for $\nu = 0.6$

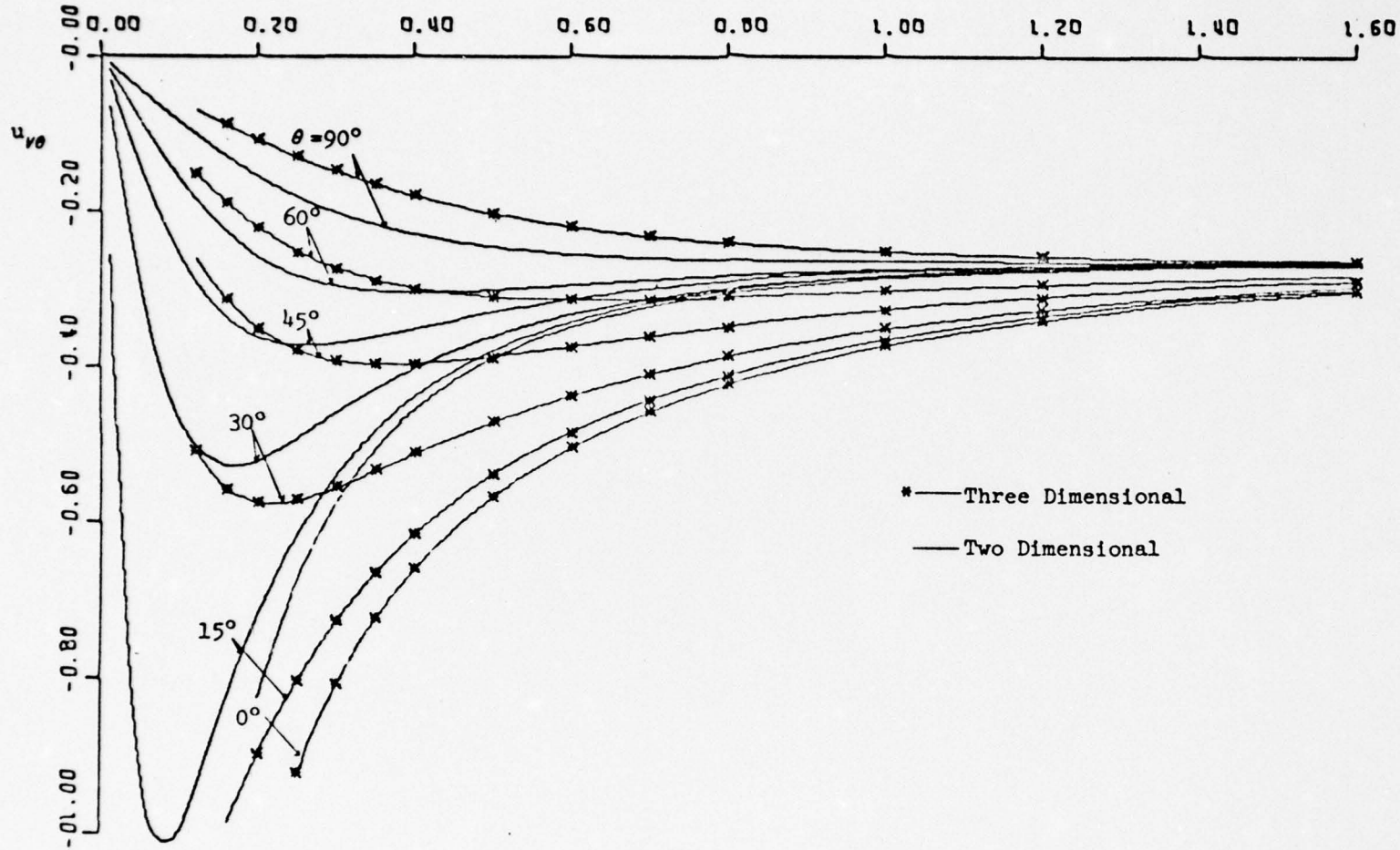


Figure 25: Tangential Velocity Distribution $u_{v\theta}$ at the Hub($\eta$ = 0.3) due to a Single Radial Vortex Line of Strength Unity for $\nu$ = 0.3

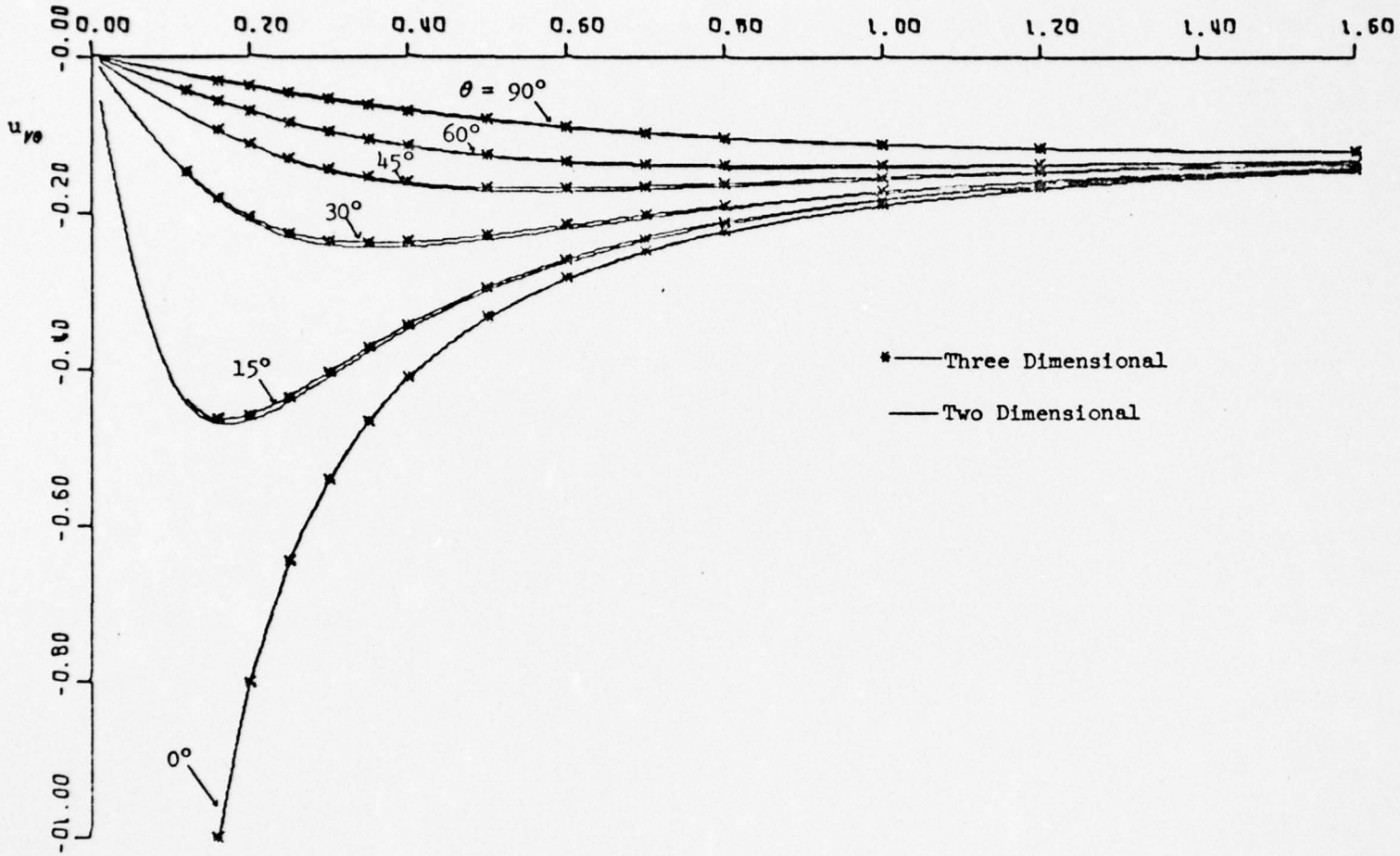


Figure 26: Tangential Velocity Distribution $u_{r\theta}$ at the Mid Radius( $\eta = 0.65$)due to a Single Radial Vortex Line of Strength Unity for $\nu = 0.3$

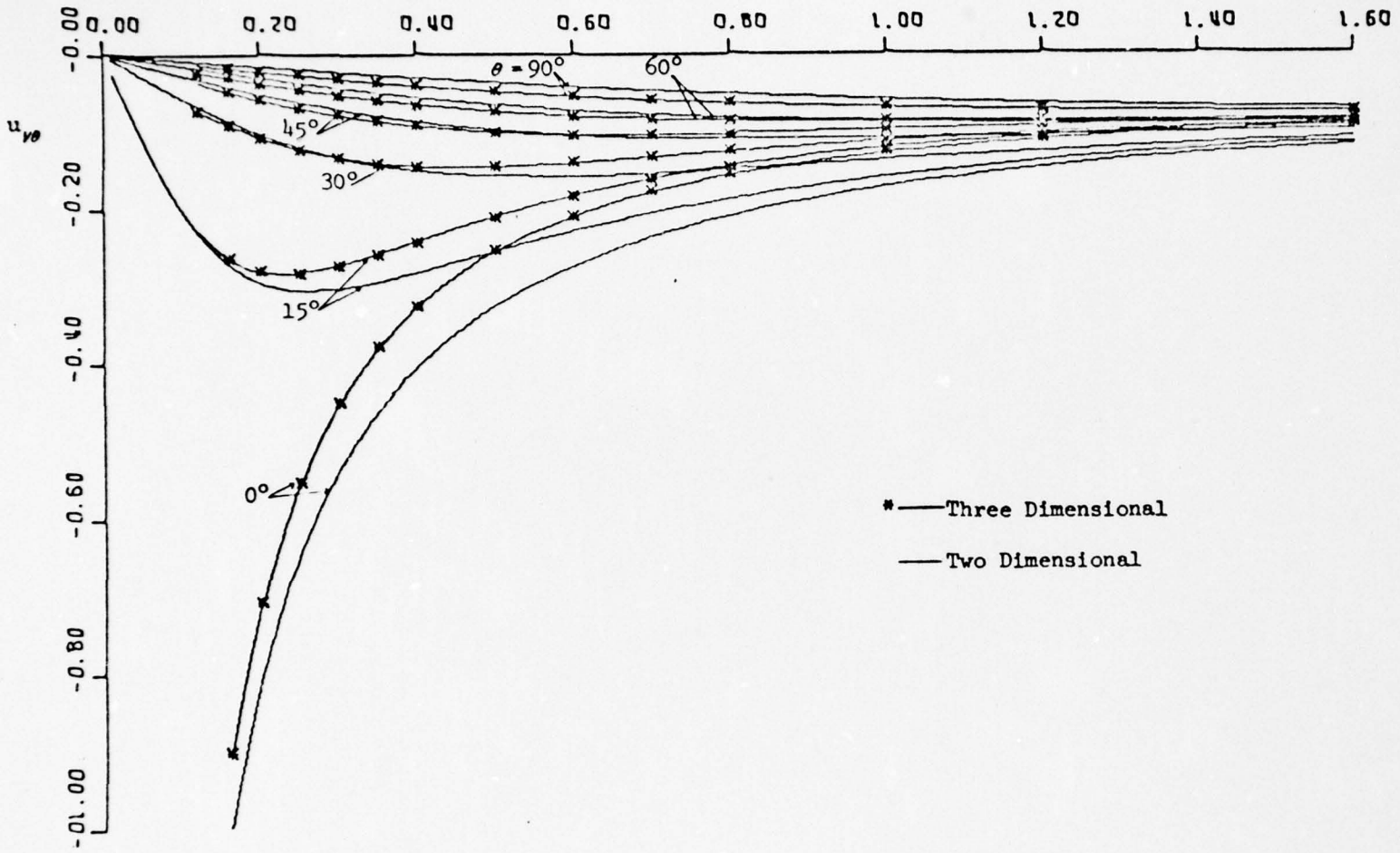


Figure 27: Tangential Velocity Distribution $u_{v\theta}$ at the Tip($\eta = 1.0$) due to a Single Radial Vortex Line of Strength Unity for $\nu = 0.3$

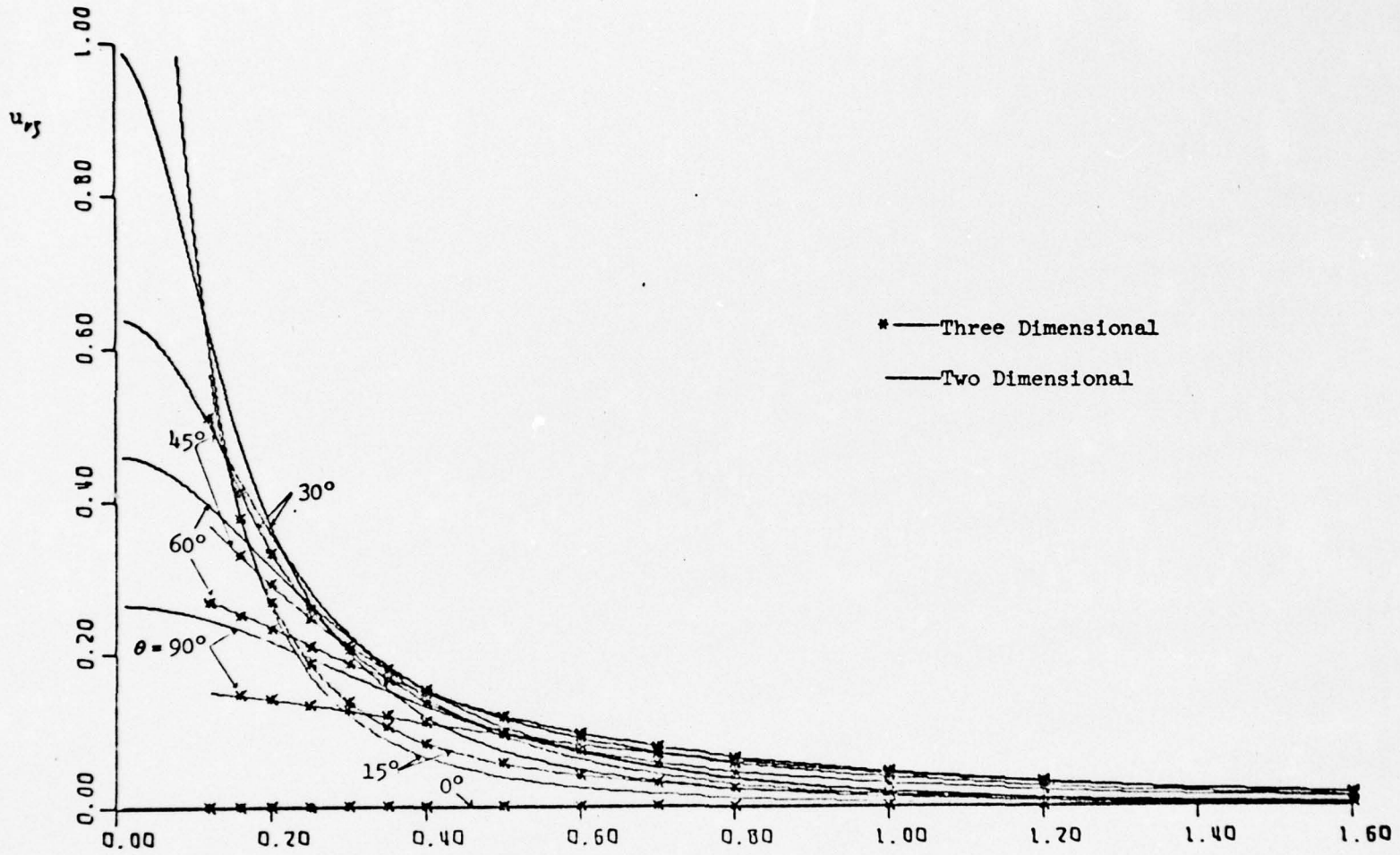


Figure 28: Axial Velocity Distribution $u_{rs}$ at the Hub($\rho = 0.3$) due to a Single Radial Vortex Line of strength Unity for $\nu = 0.3$

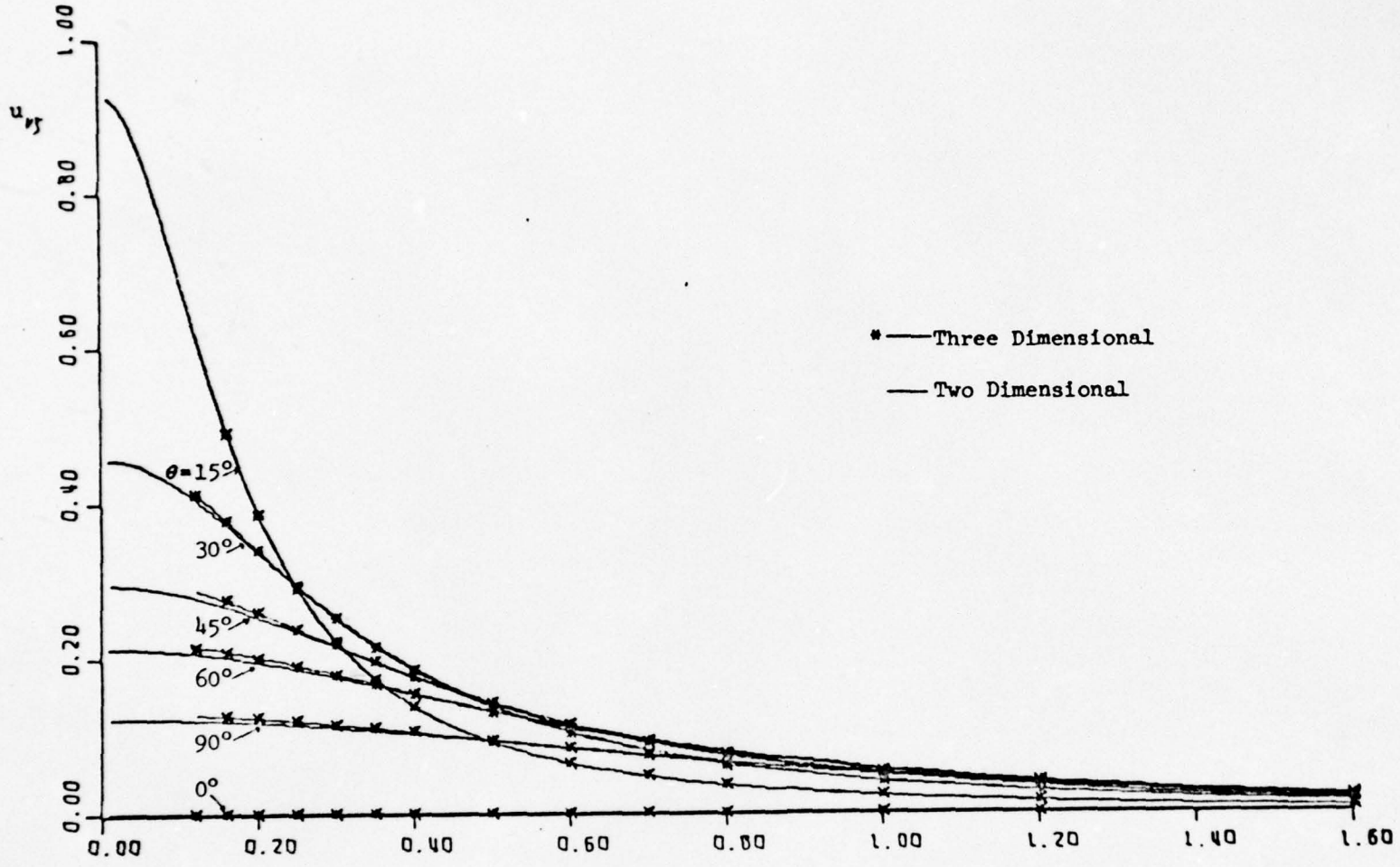


Figure 29: Axial Velocity Distribution $u_{\nu\zeta}$ at the Mid Radius( $\eta = 0.65$) due to a Single Radial Vortex Line of Strength Unity for $\nu = 0.3$

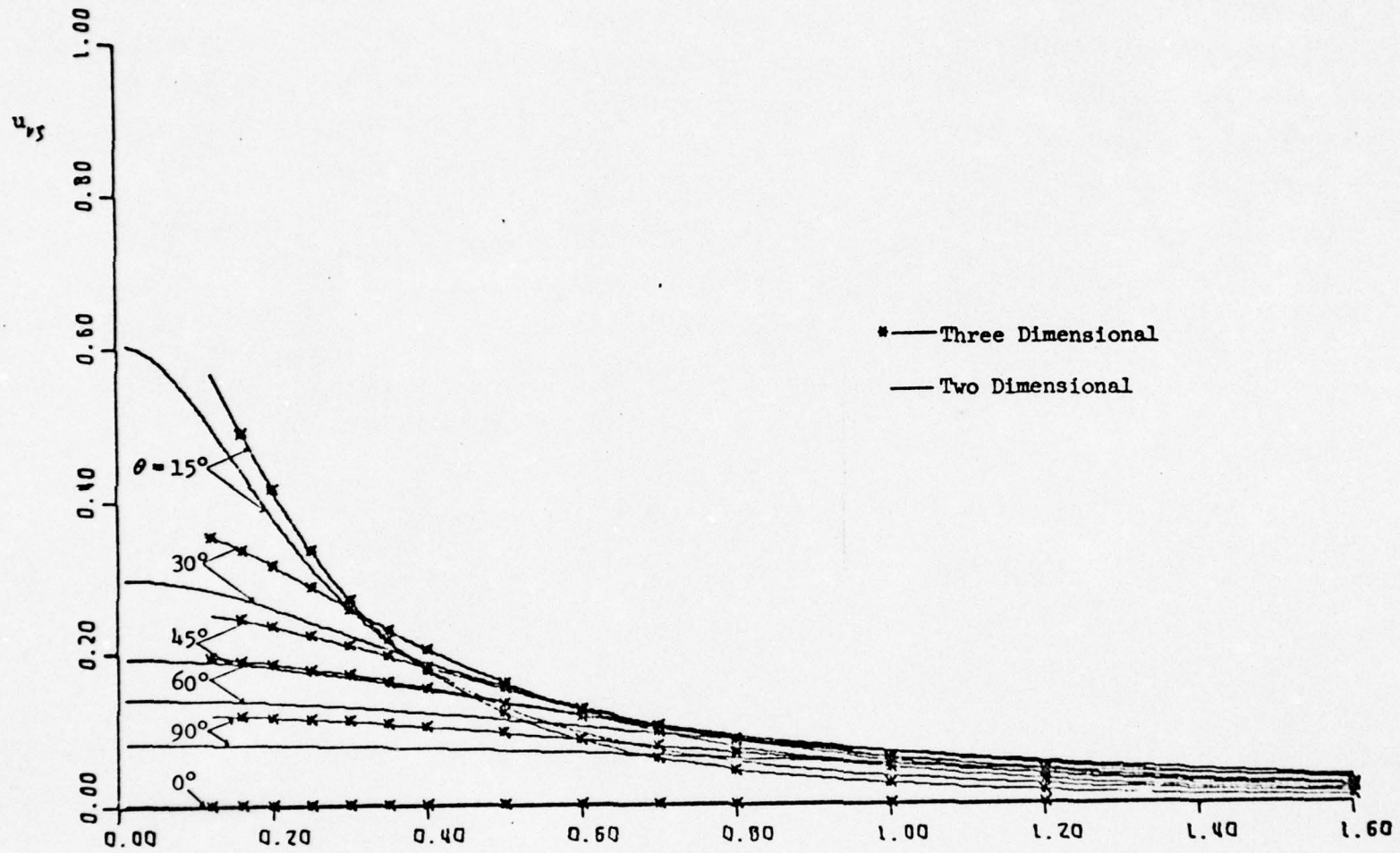


Figure 30: Axial Velocity Distribution $u_{\nu\zeta}$ at the Tip( $\eta = 1.0$) due to a Single Radial Vortex Line of Strength Unity for $\nu = 0.3$

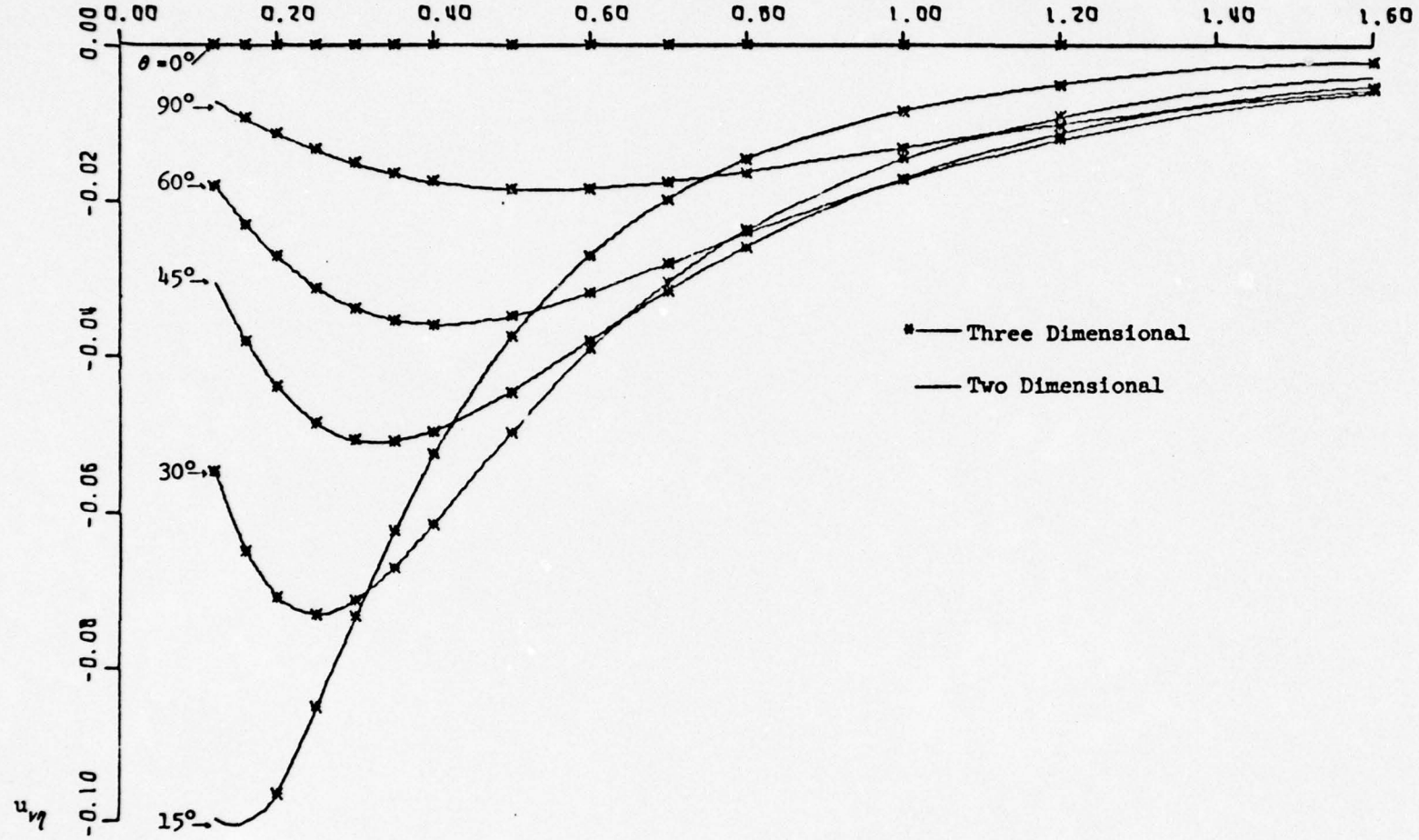


Figure 31: Radial Velocity Distribution $u_{r\eta}$ at the Mid Radius($\eta = 0.65$) due to a Single Radial Vortex Line of Strength Unity for $\nu = 0.3$

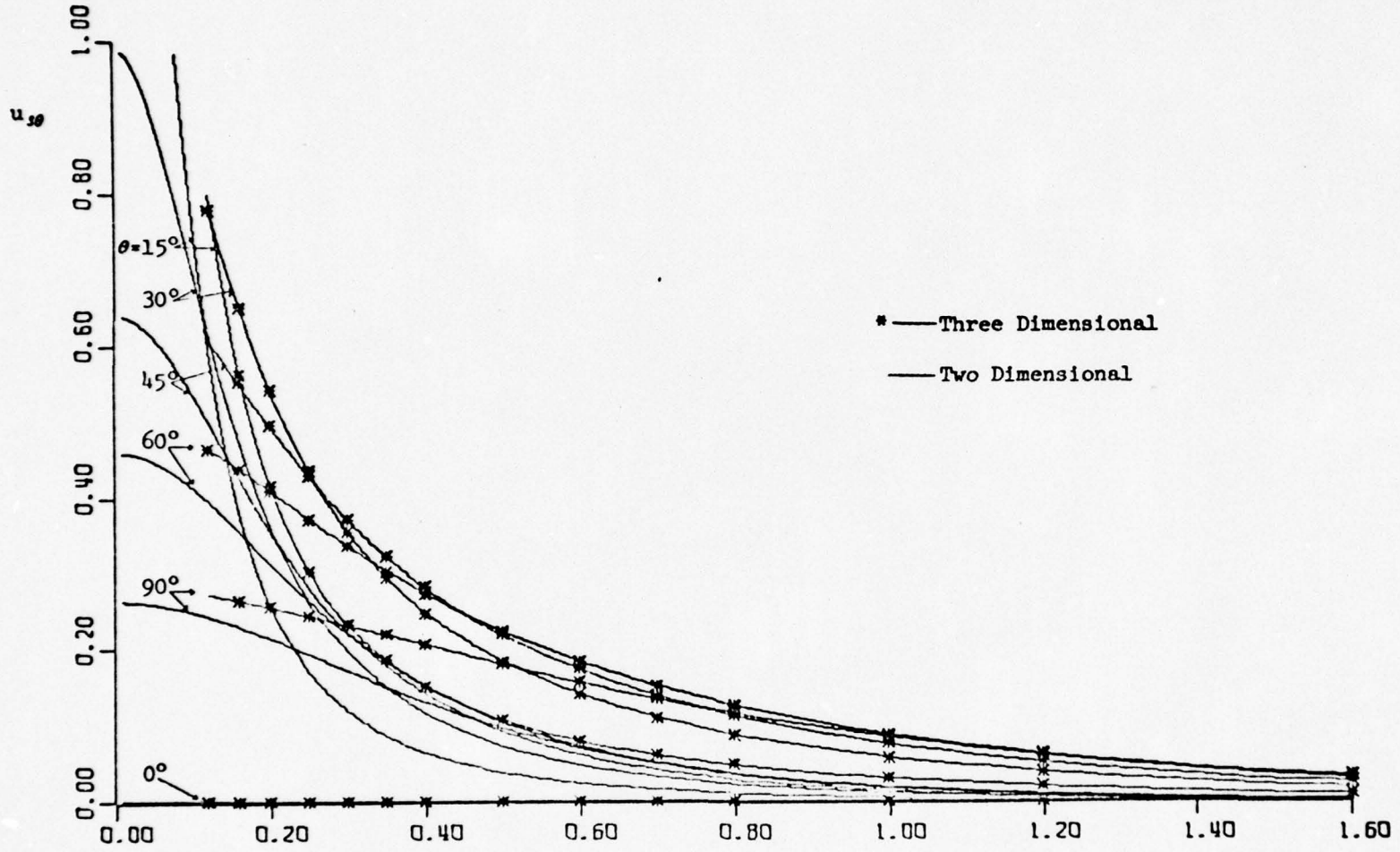


Figure 32: Tangential Velocity Distribution $u_{s\theta}$ at the Hub( $\eta = 0.3$) due to a Single Radial Source Line of Strength Unity for $\nu = 0.3$

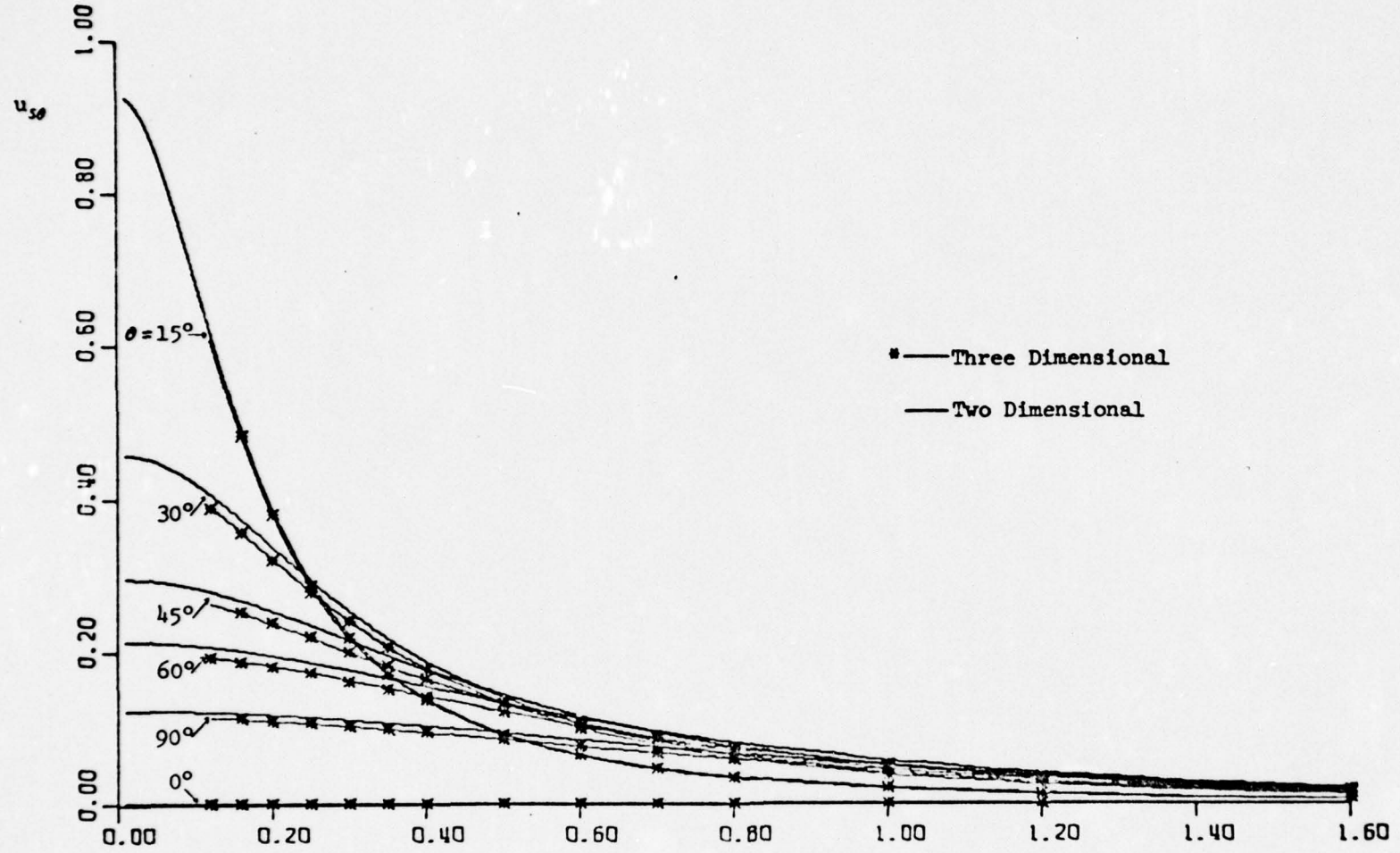


Figure 33: Tangential Velocity Distribution $u_{s\theta}$ at the Mid Radius( $\eta = 0.65$) due to a Single Radial Source Line of Strength Unity for $\nu = 0.3$

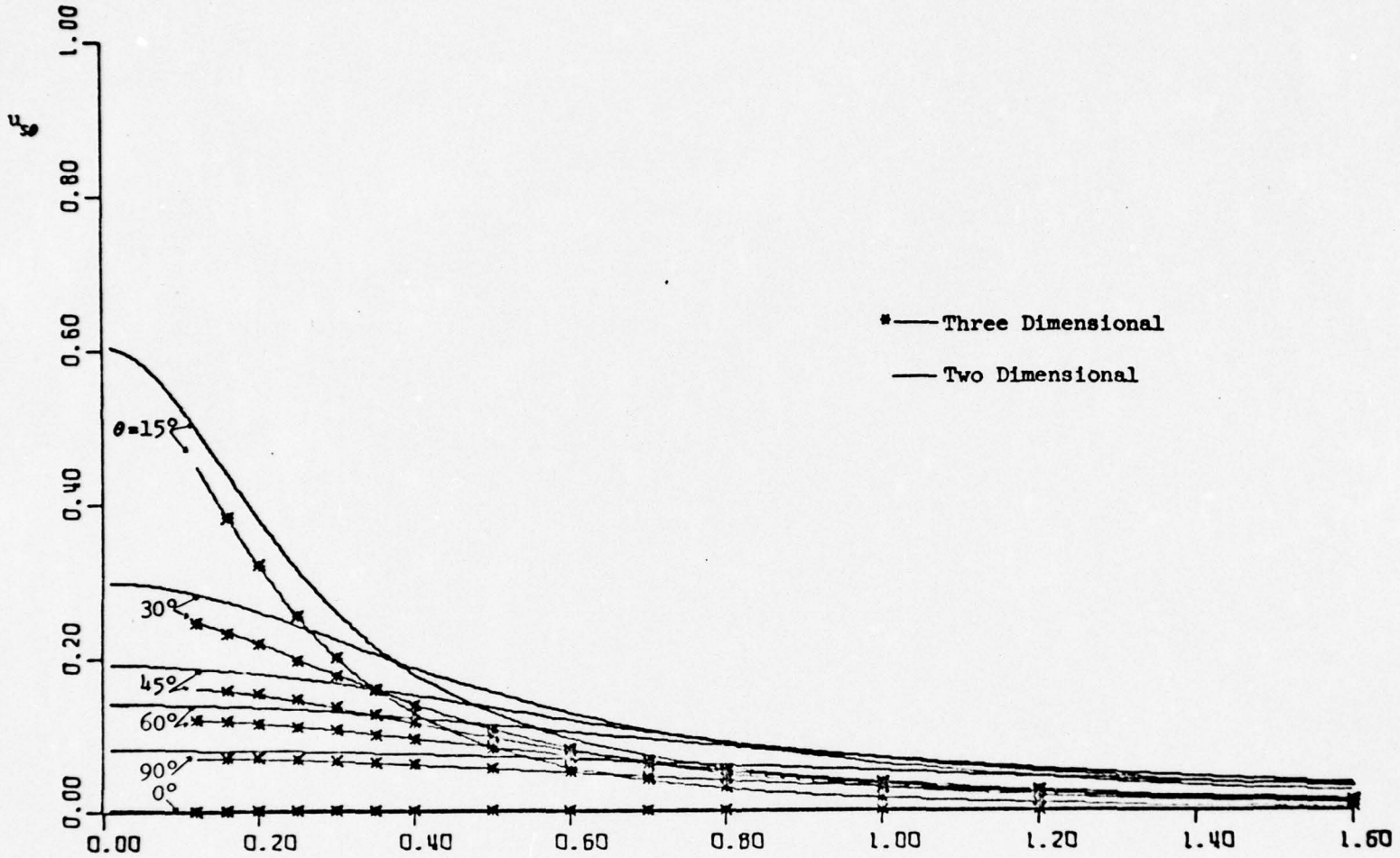


Figure 34: Tangential Velocity Distribution $u_{s\theta}$ at the Tip( $\eta = 1.0$) due to a Single Radial Source Line of Strength Unity for $\nu = 0.3$

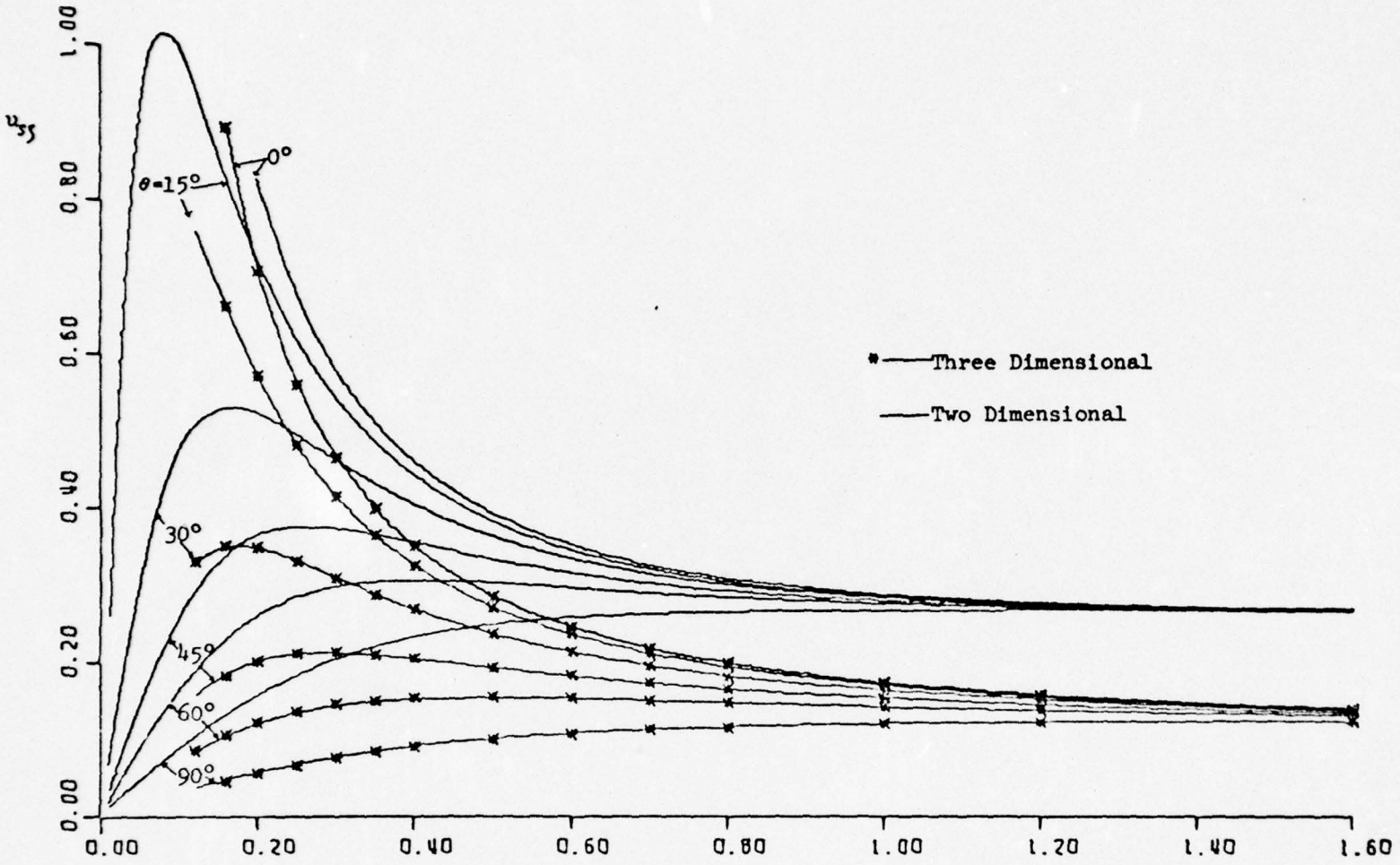


Figure 35: Axial Velocity Distribution $u_{55}$ at the Hub( $\eta$ = 0.3) due to a Single Radial Source Line of Strength Unity for $\nu$ = 0.3

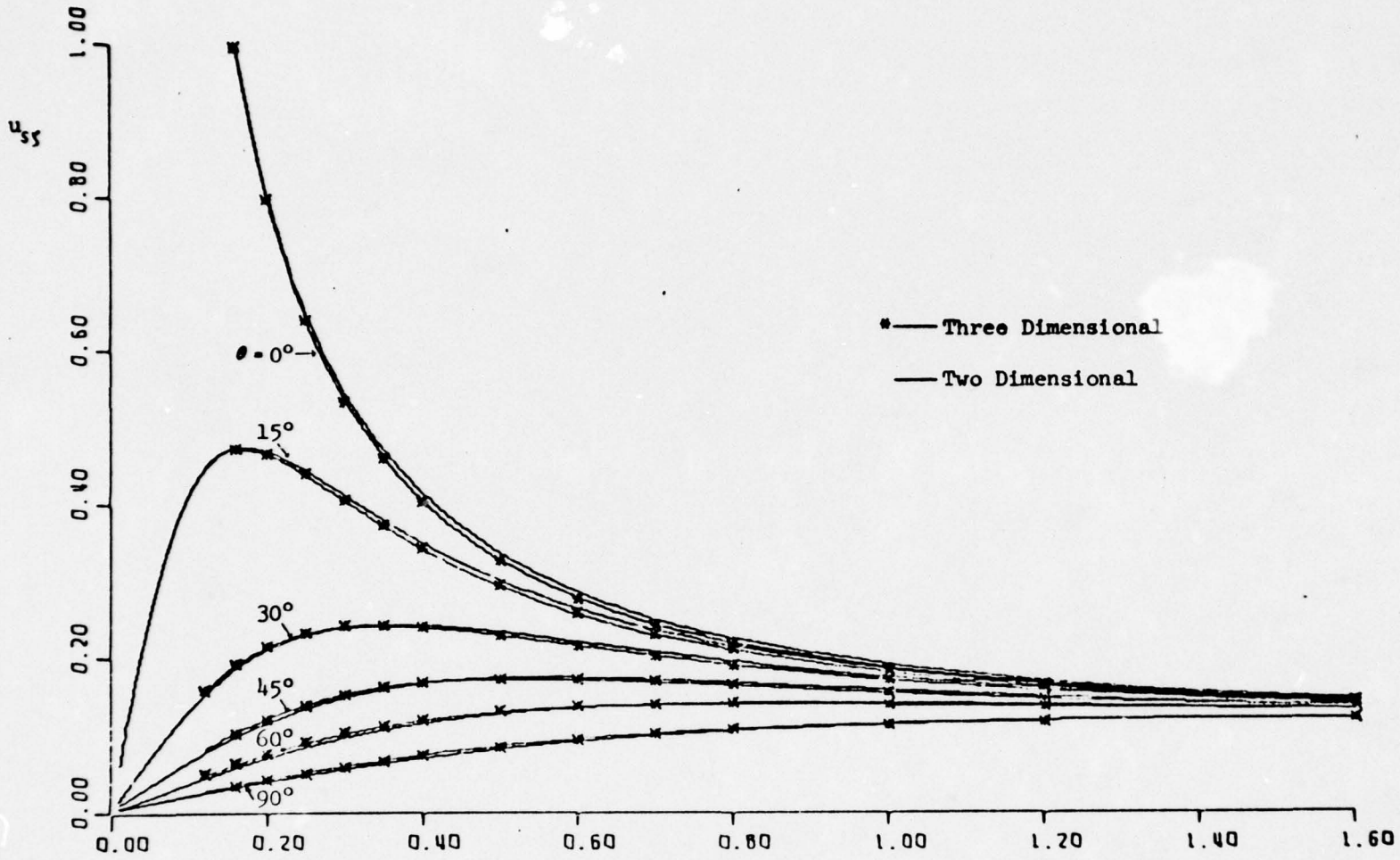


Figure 36: Axial Velocity Distribution $u_{ss}$ at the Mid Radius($\eta = 0.65$) due to a Single Radial Source Line of Strength Unity for $\nu = 0.3$

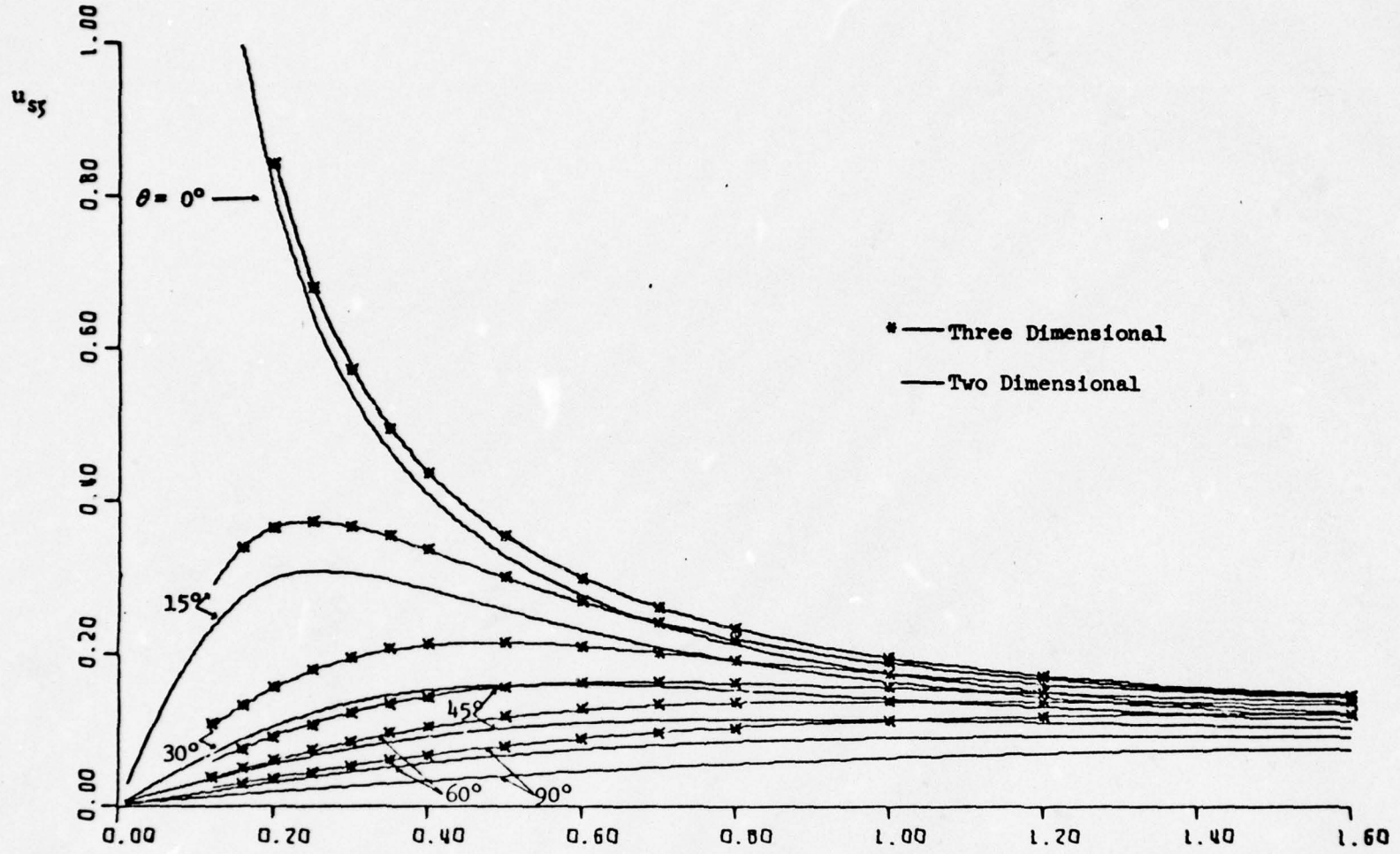


Figure 37: Axial Velocity Distribution $u_{sf}$ at the Tip( $\eta = 1.0$) due to a Single Radial Source Line of Strength Unity for $\nu = 0.3$

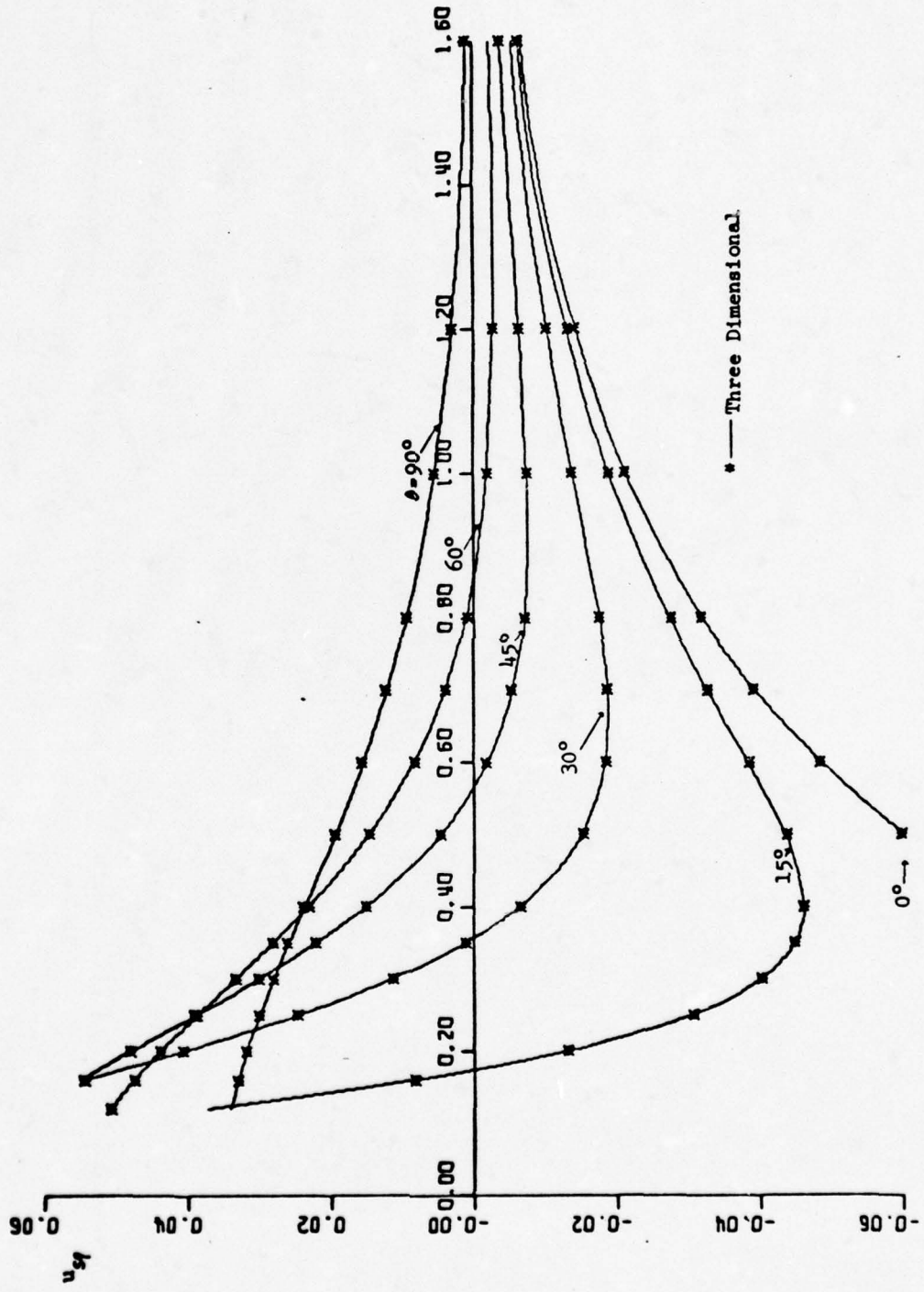


Figure 38: Radial Velocity Distribution $u_{sr}$ at the Mid Radius( $\rho = 0.65$) due to a Single Radial Source Line of Strength unity for $\nu = 0.3$

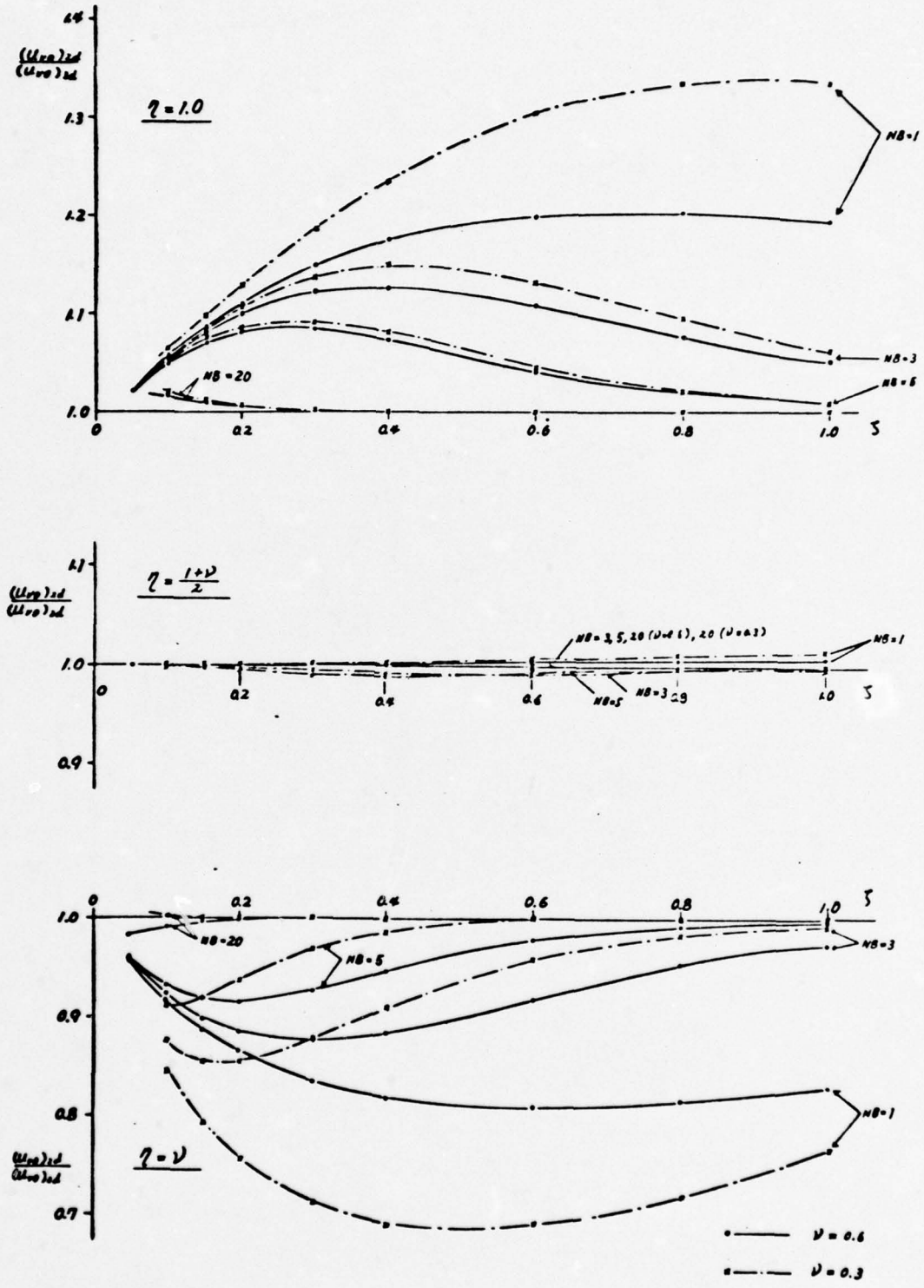


Fig.39: Ratio of the Tangential Velocities induced by the Radial Vortex Lines of JVS=1 at $\vartheta=2°$

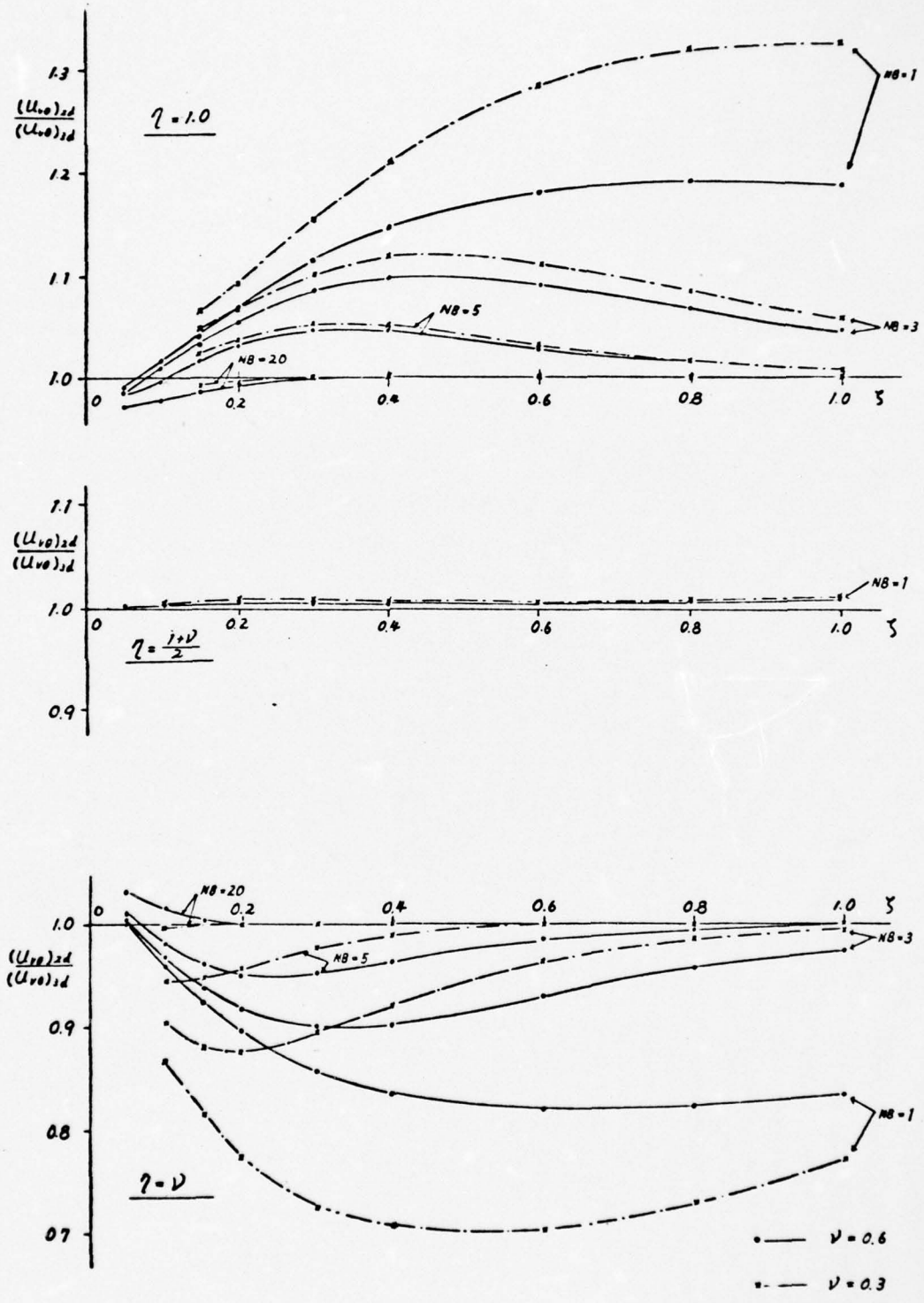


**Fig.40**: Ratio of the Tangential Velocities induced by the Radial Vortex Lines of JVS=1 at $\vartheta = 9^{\circ}$

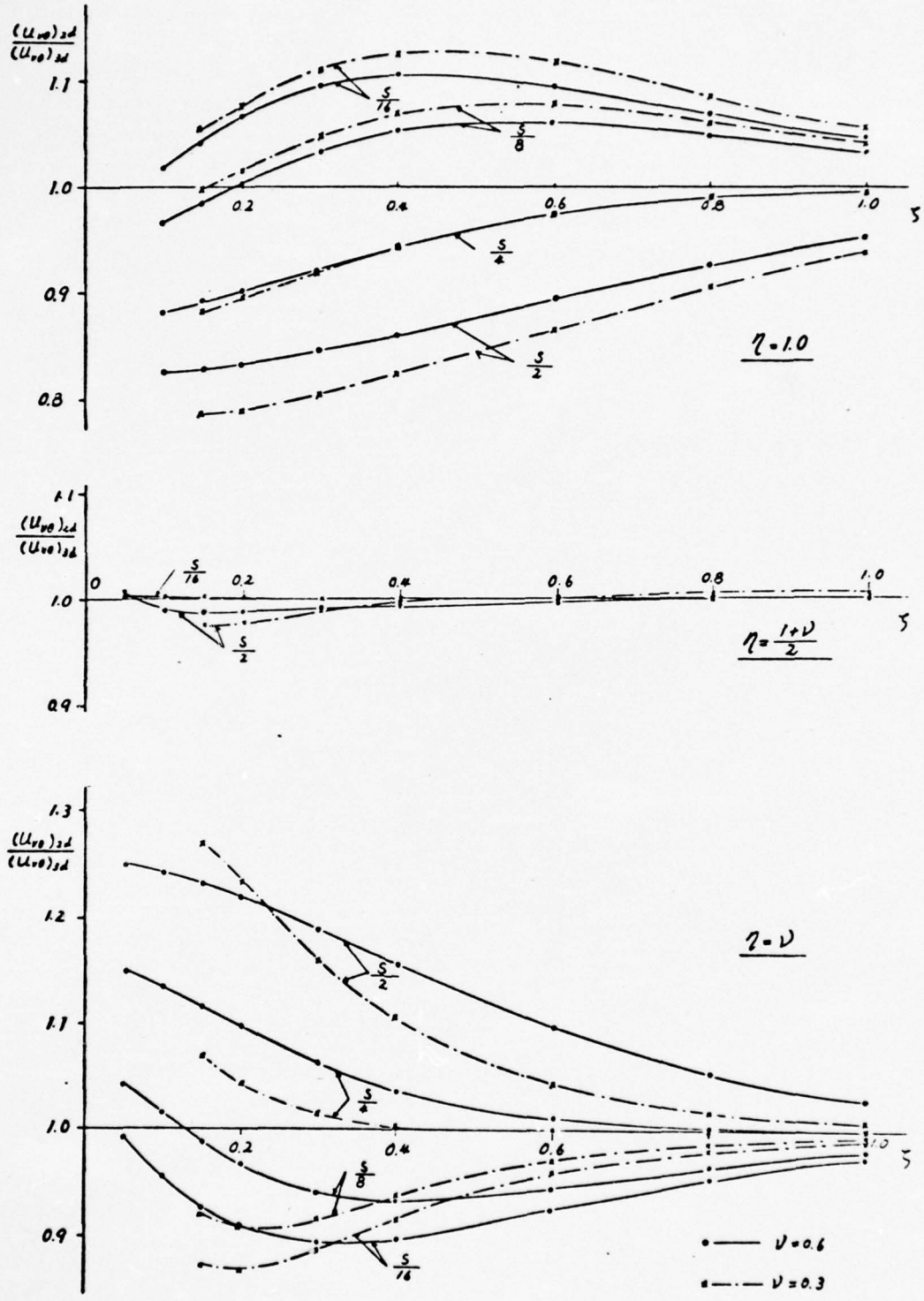


Fig.41: Ratio of the Tangential Velocities induced by the Radial Vortex Lines of JVS=1 at =1/2,1/4, 1/8, 1/16-Spacing Points for NB=3

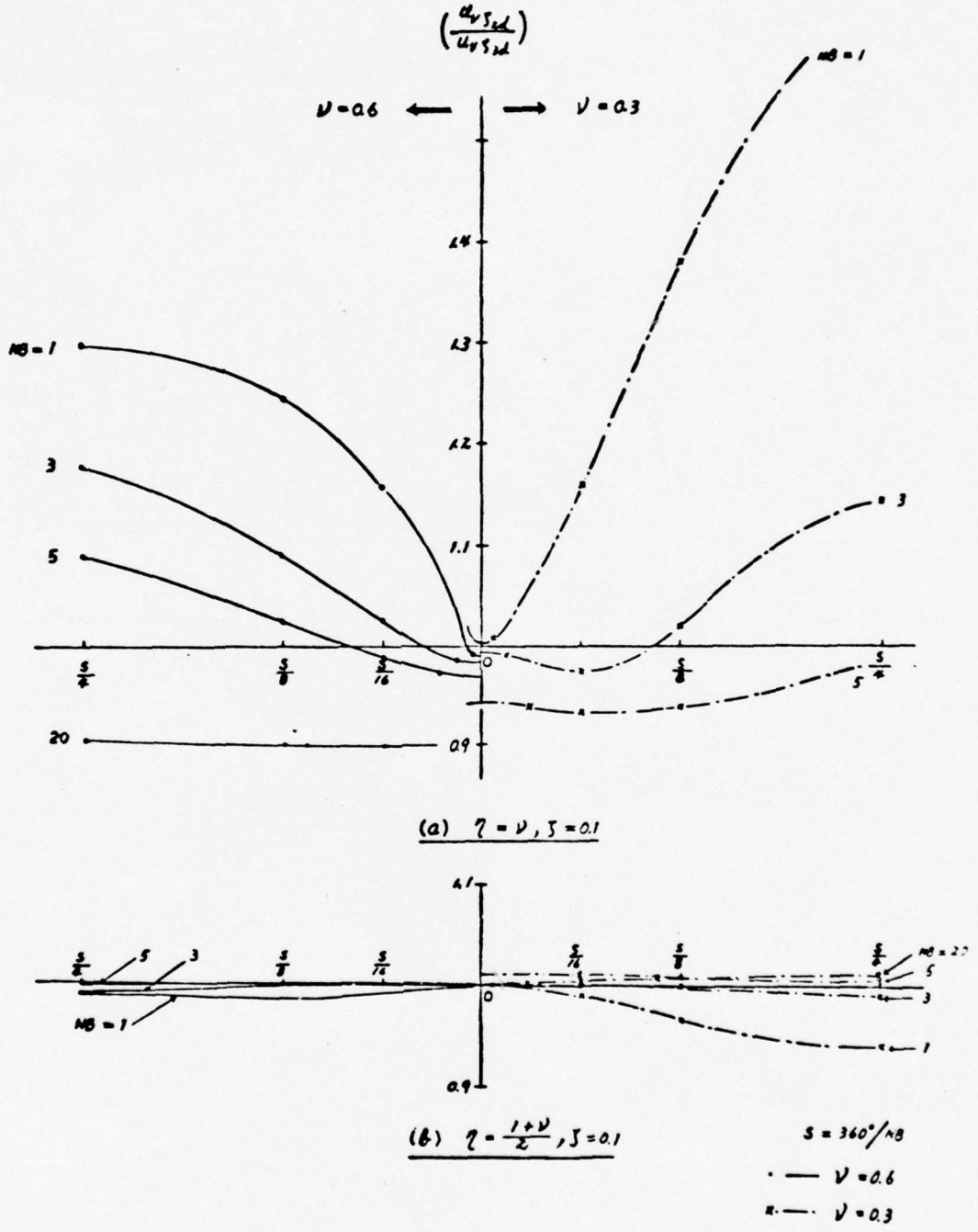


Figure 42: Ratio of the Axial Velocities induced by the Radial Vortex Lines of JVS=1 at $\zeta = 0.1$, $\eta = \nu$ and $\frac{1+\nu}{2}$

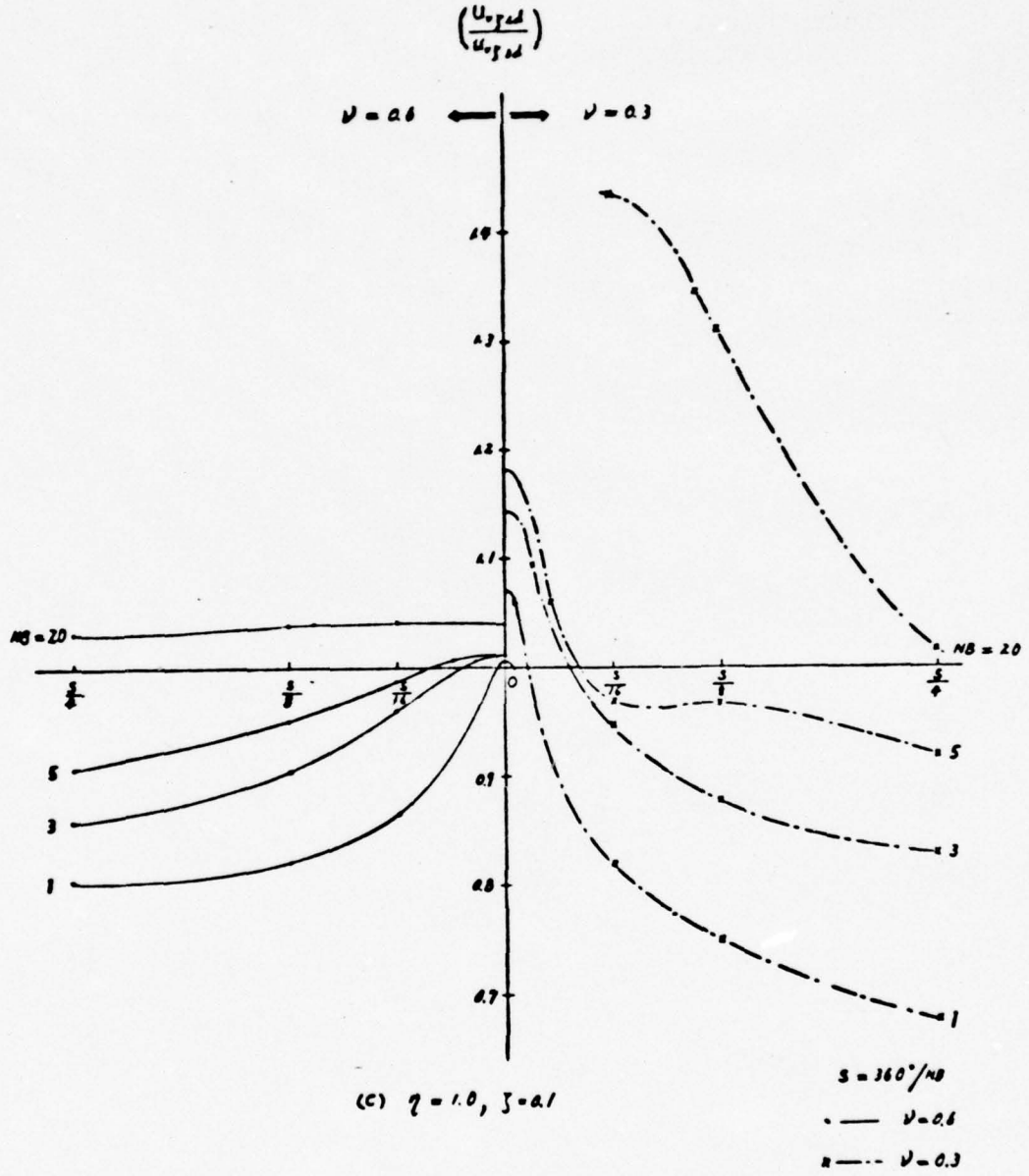


**Fig.42c**: Ratio of the Axial Velocities induced by the Radial Vortex Lines of JVS=1 at $\zeta$=0.1 and $\eta$=1.0

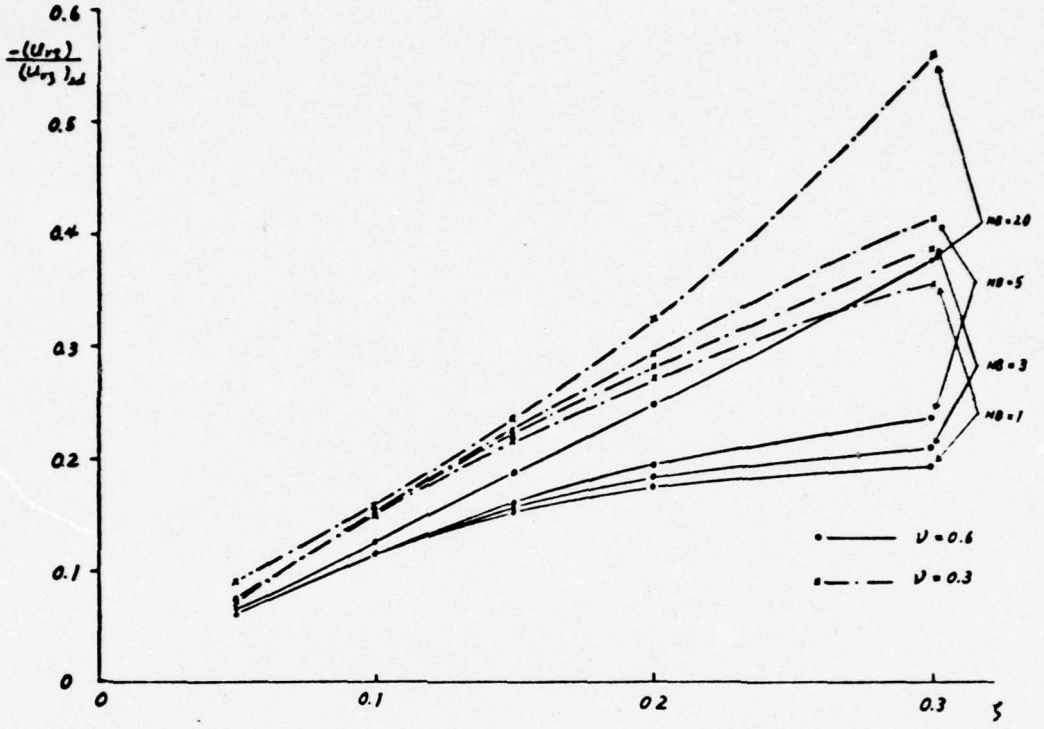


**Fig.43**: Ratio of the Radial Velocities induced by the Radial Vortex Lines of JVS=1 at $\theta = 2°$ and $\eta = \frac{r+l}{2}$

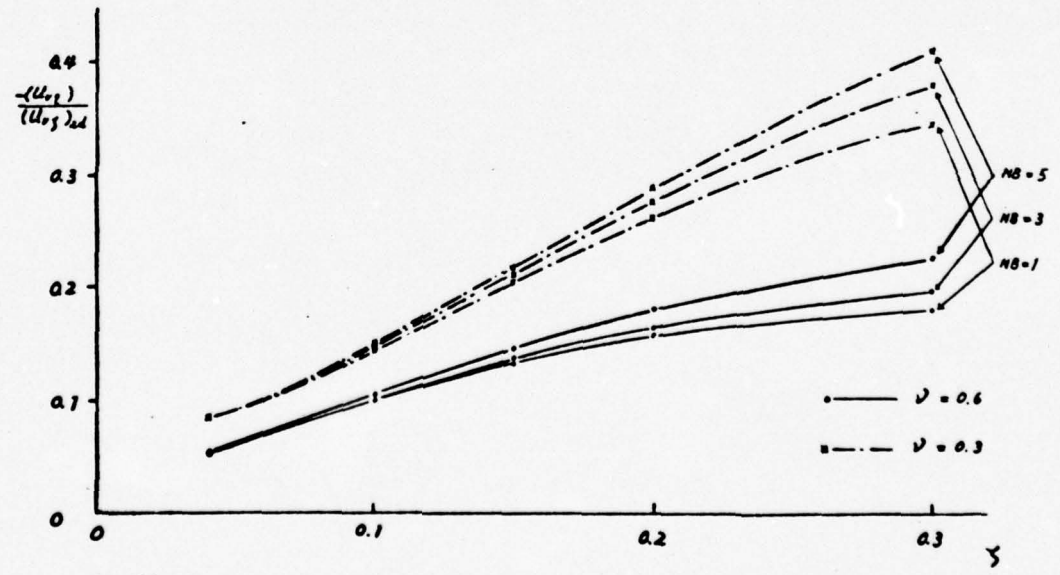


**Fig.44**: Ratio of the Radial Velocities induced by the Radial Vortex Lines of JVS=1 at $\theta = 9°$ and $\eta = \frac{r+l}{2}$

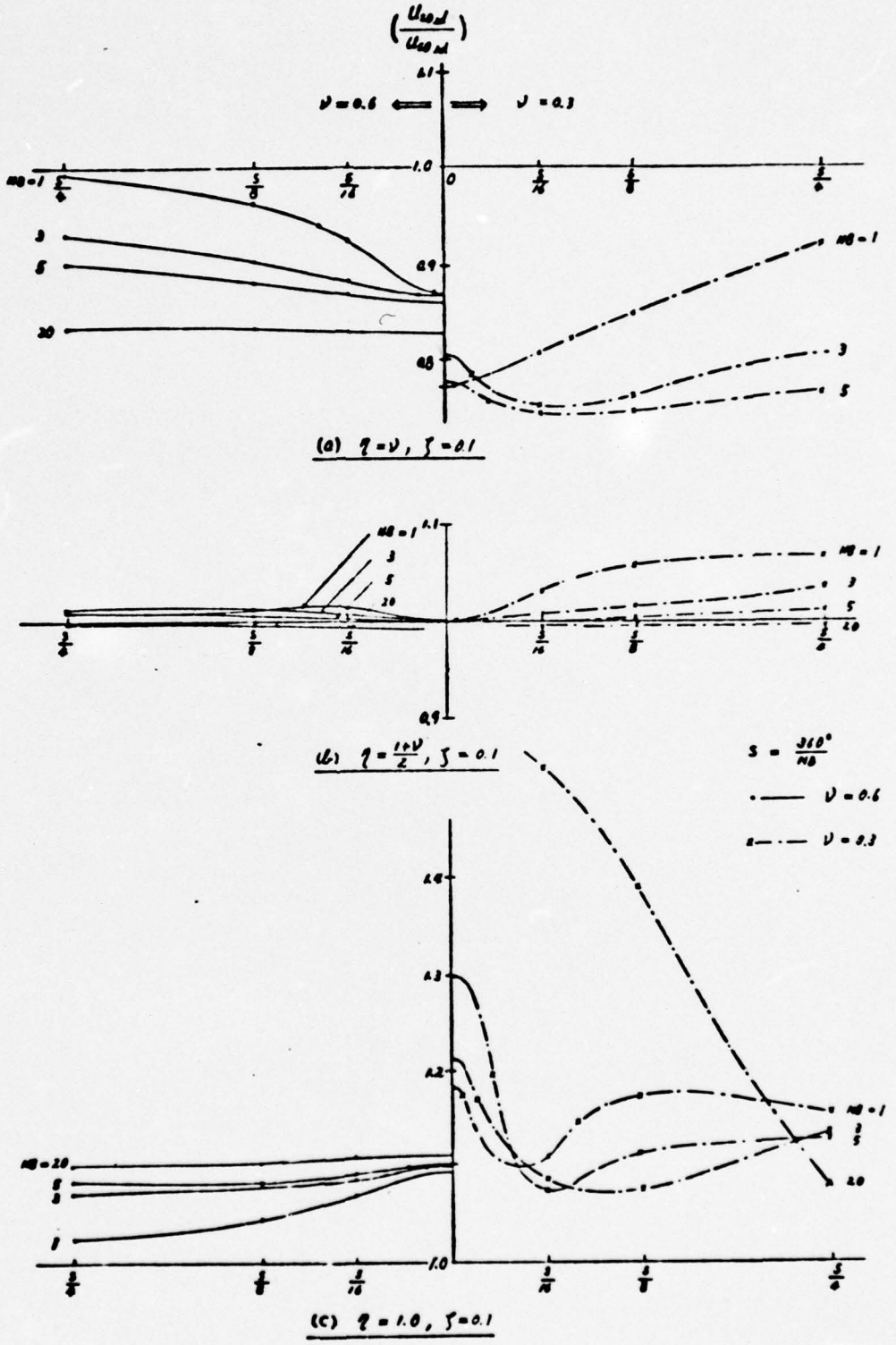


**Figure 45** : Ratio of the Tangential Velocities induced by the Radial Source Lines of JVS=1 at $\zeta$=0.1, $\eta = \nu, \frac{1+\nu}{2}$ and 1.0

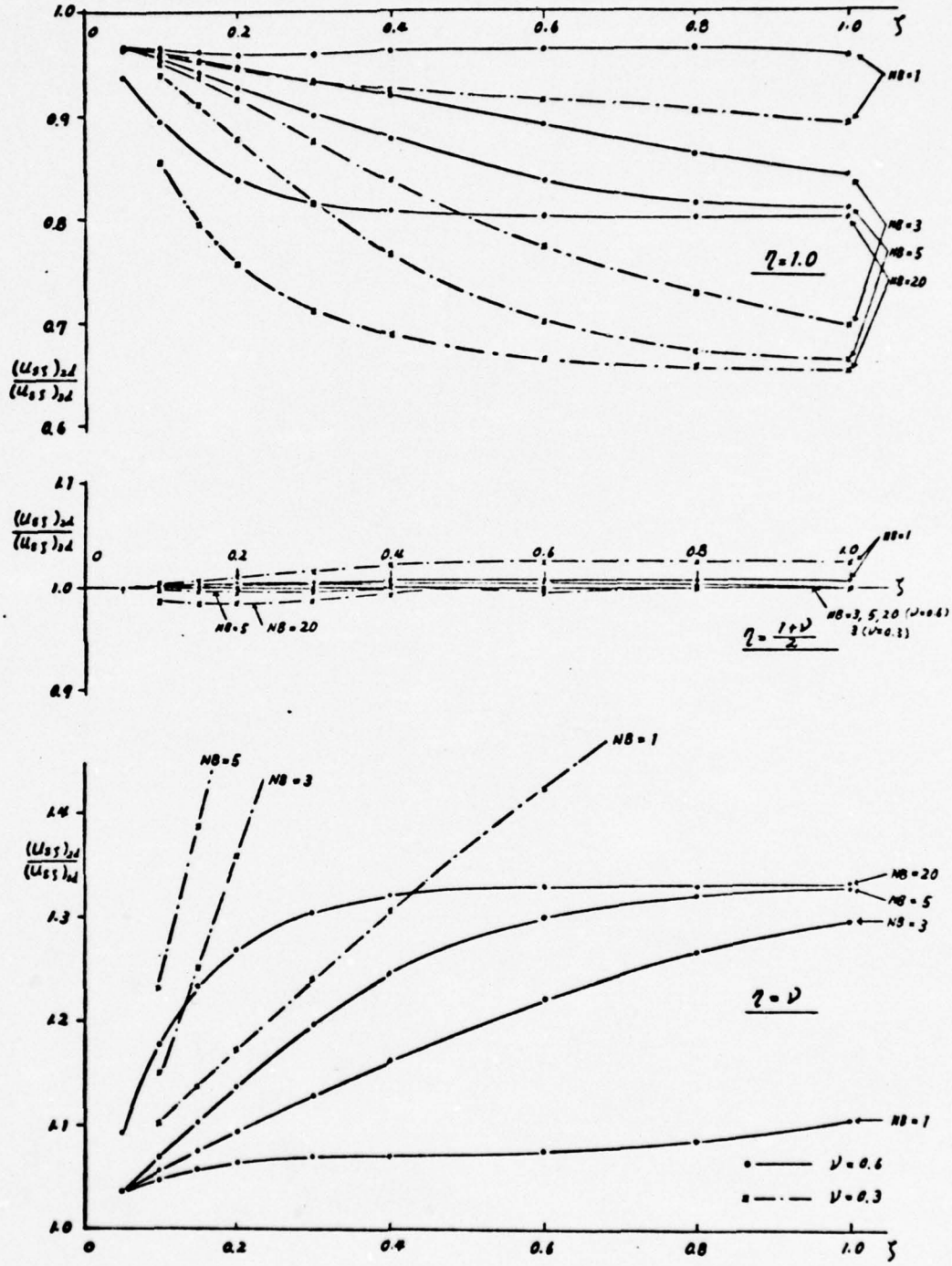


Fig.46: Ratio of the Axial Velocities induced by the Radial Source Lines of JVS=1 at $\theta = 2^{\circ}$, $\eta = \nu, \frac{1+\nu}{2}$ and 1.0

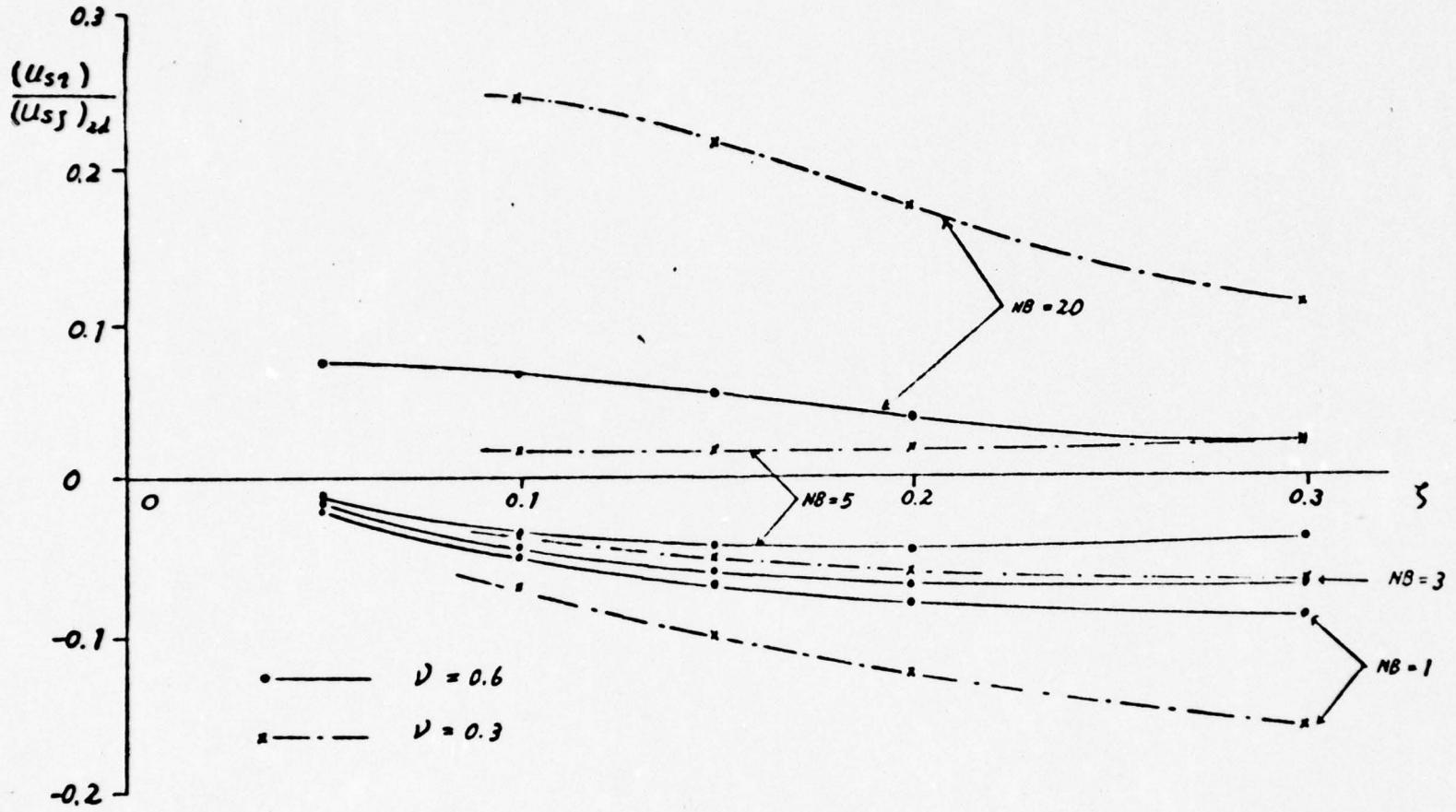


Fig.47: Ratio of the Radial Velocities induced by the Radial Source Lines of JVS=1 at $\theta = 2°$ and $\eta = \frac{1+\nu}{2}$

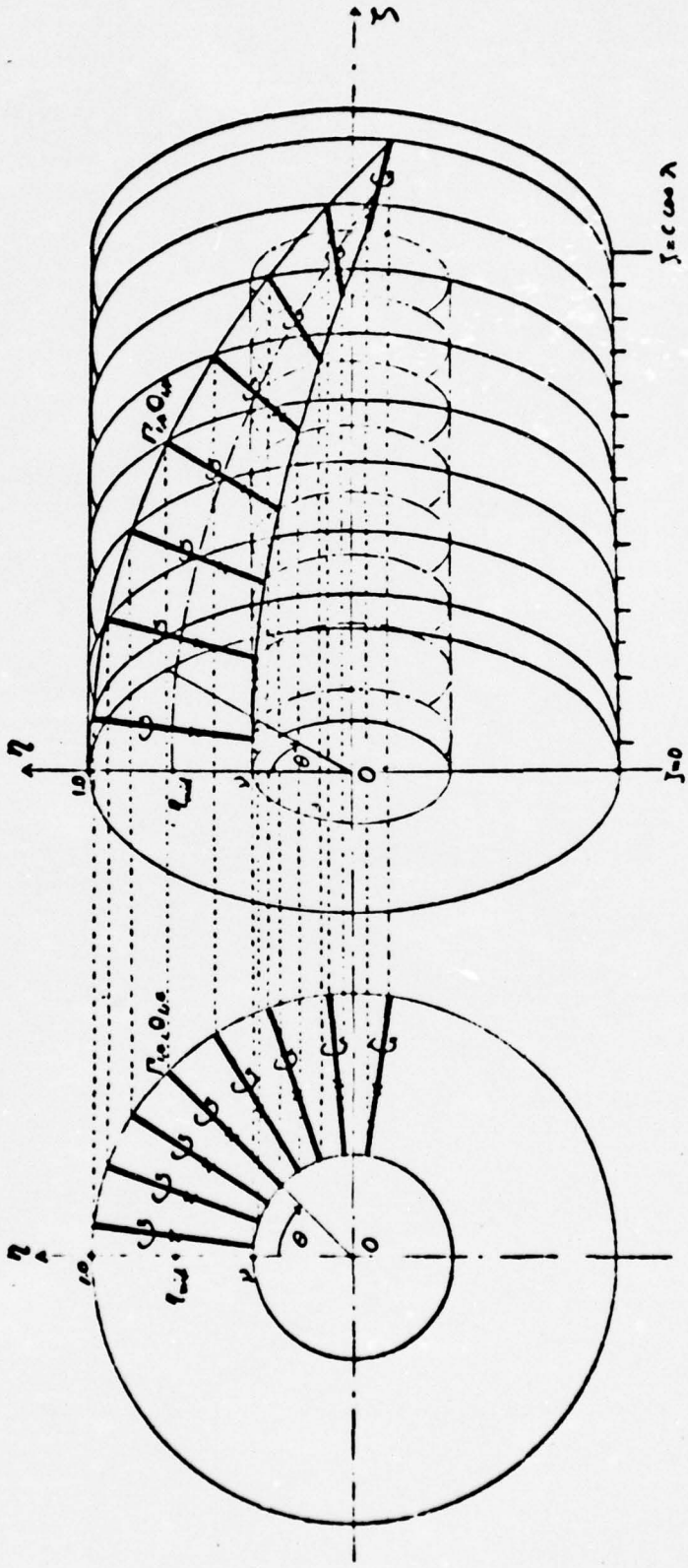

Fig. 48: Sketch of a model including 8 radial vortex and source lines.

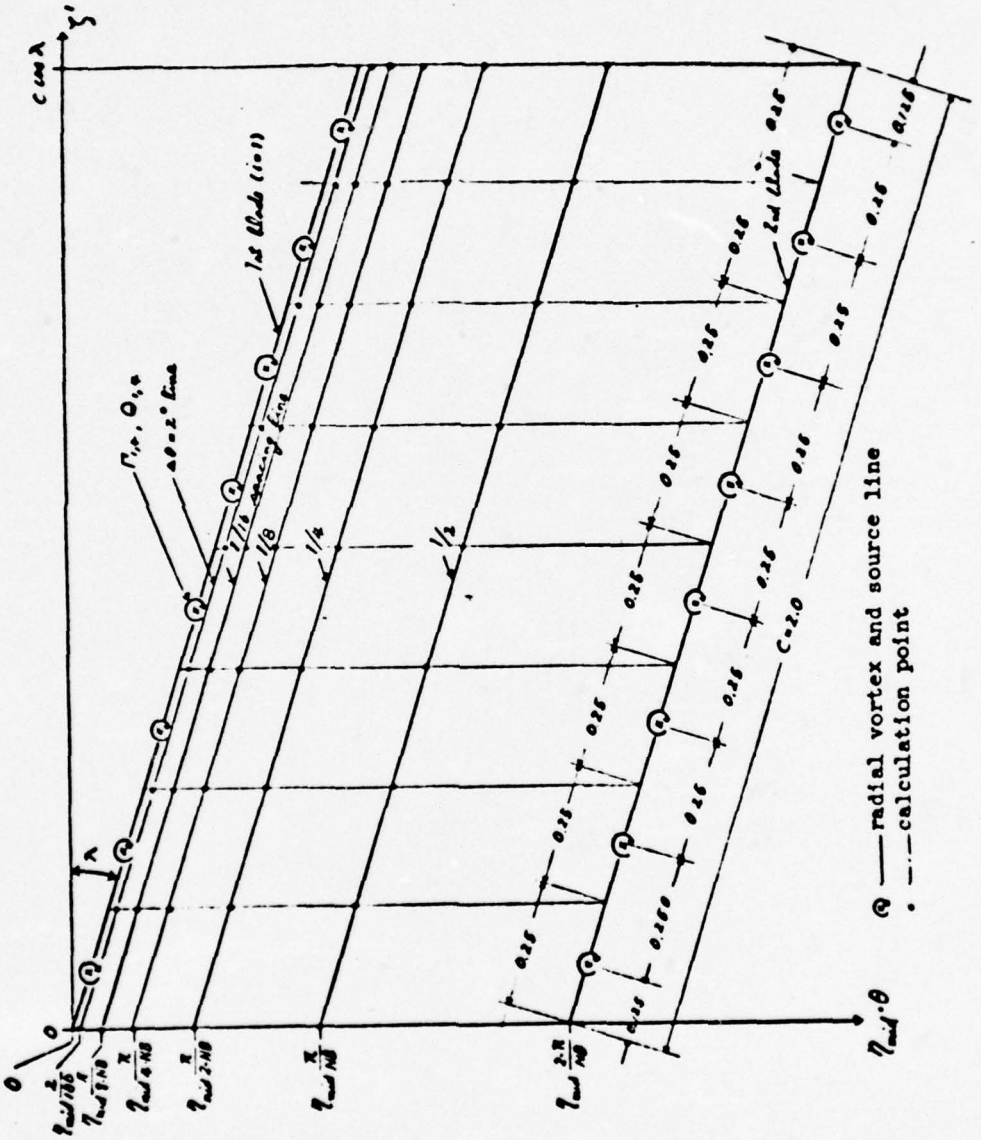


Fig. 49: Singular points and calculation points on $(\xi', \eta', 0)$-plane

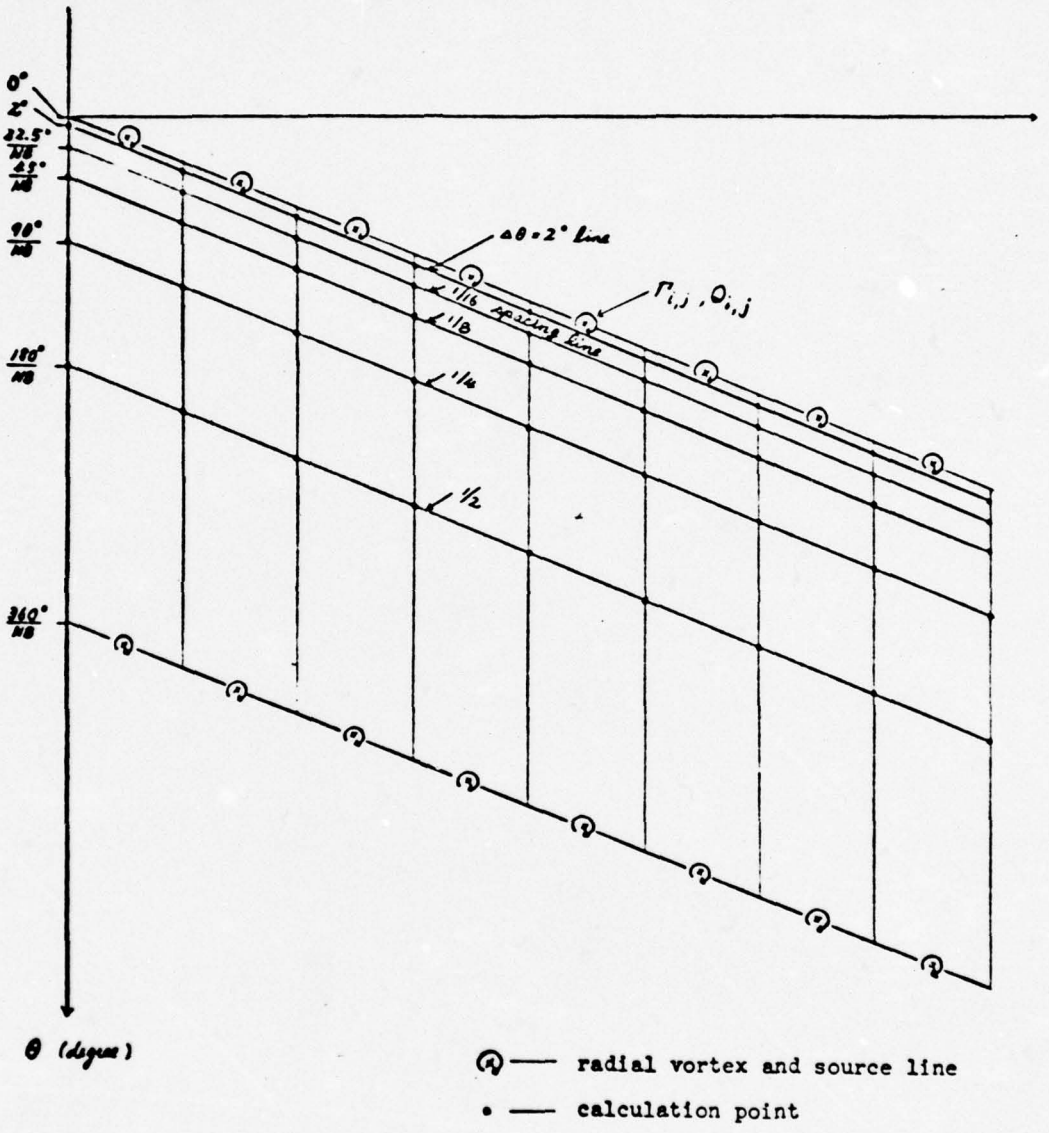


Fig. 50: Singular points and calculation points on $(r', \theta)$-plane

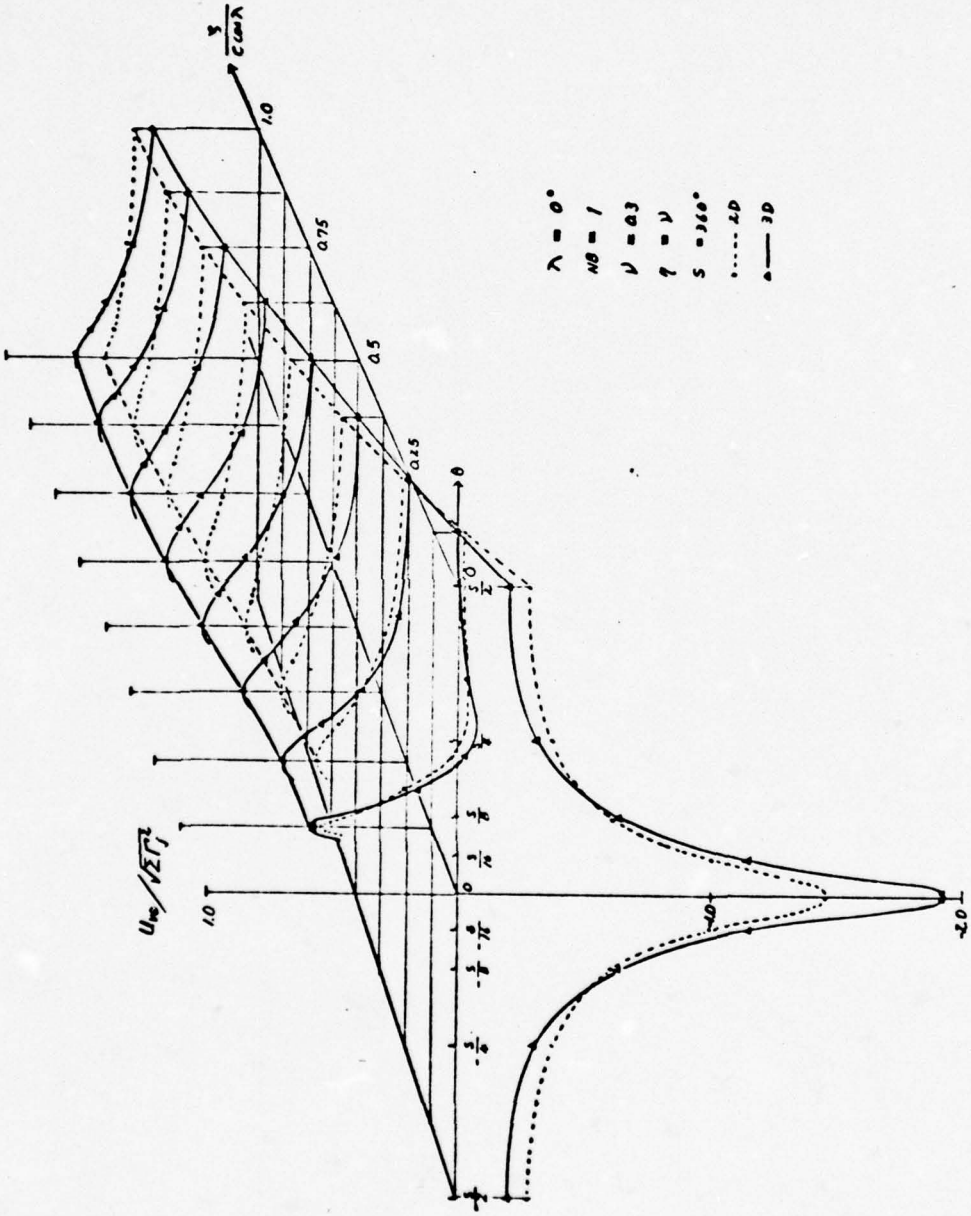


Fig.51: Distribution of the Tangential Velocities at the Hub induced by NB Series of Radial Vortex Lines of JVS=8 for $\lambda$=0°, NB=1 and $\nu$=0.3

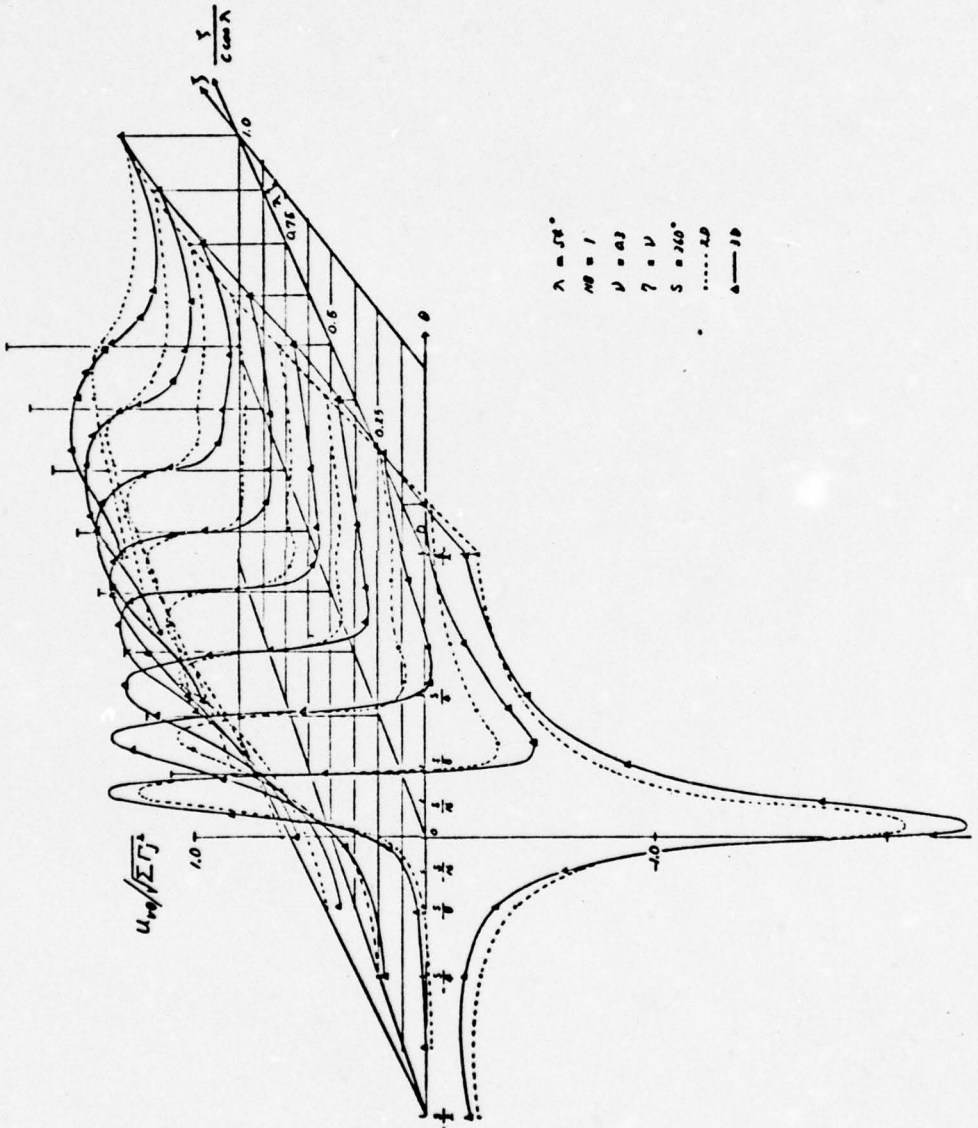

Fig.52: Distribution of the Tangential Velocities at the Hub Induced by NB Series of Radial Vortex Lines of JVS=8 for $\Lambda$=54°, NB=1 and $\nu$=0.3

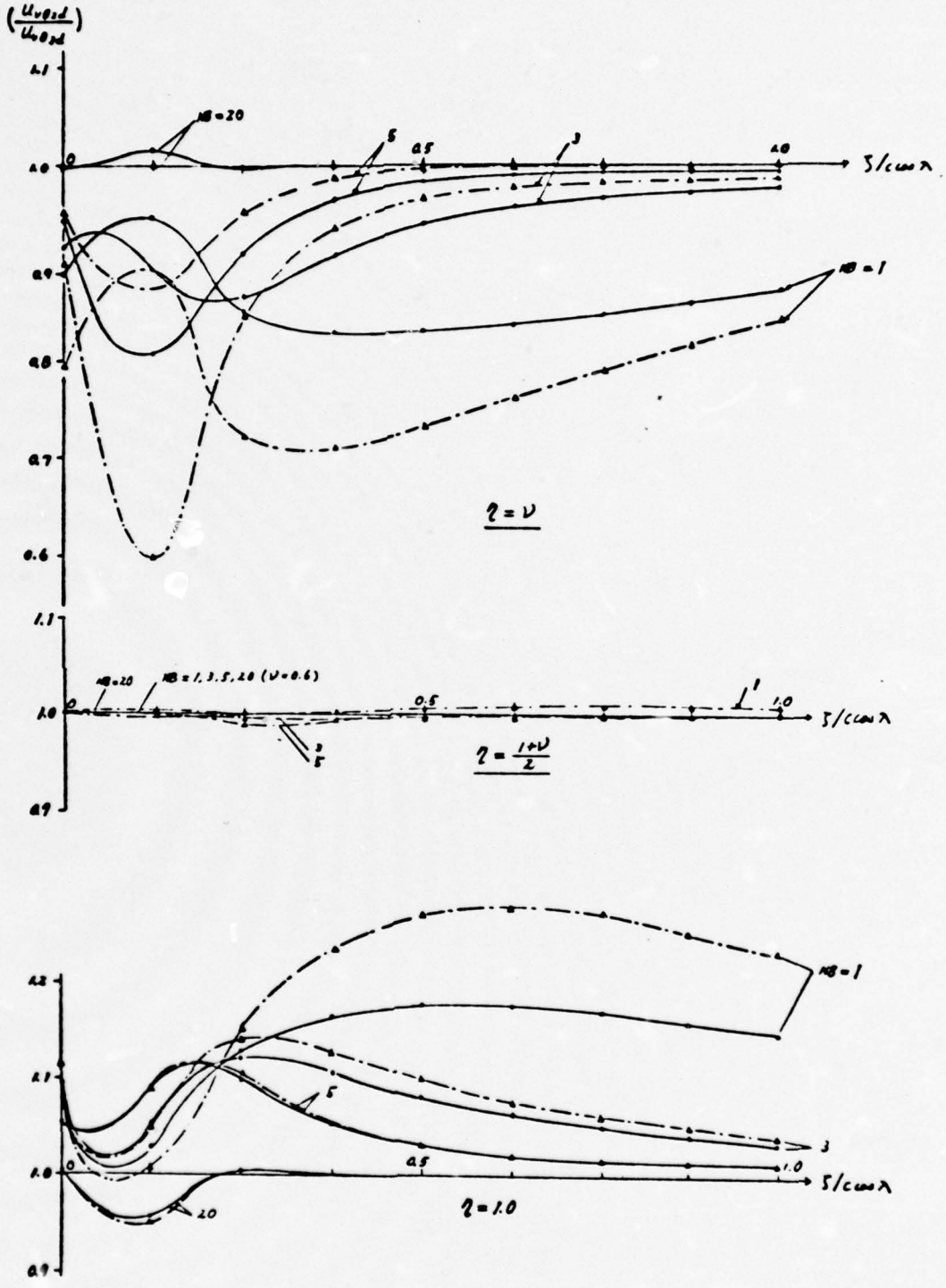


**Fig.53**: Ratio of the Tangential Velocities induced by NB Radial Vortex Lines of JVS=8 for $\Delta\theta = 2°$ at $\eta = \nu, \frac{1+\nu}{2}$ and 1.0

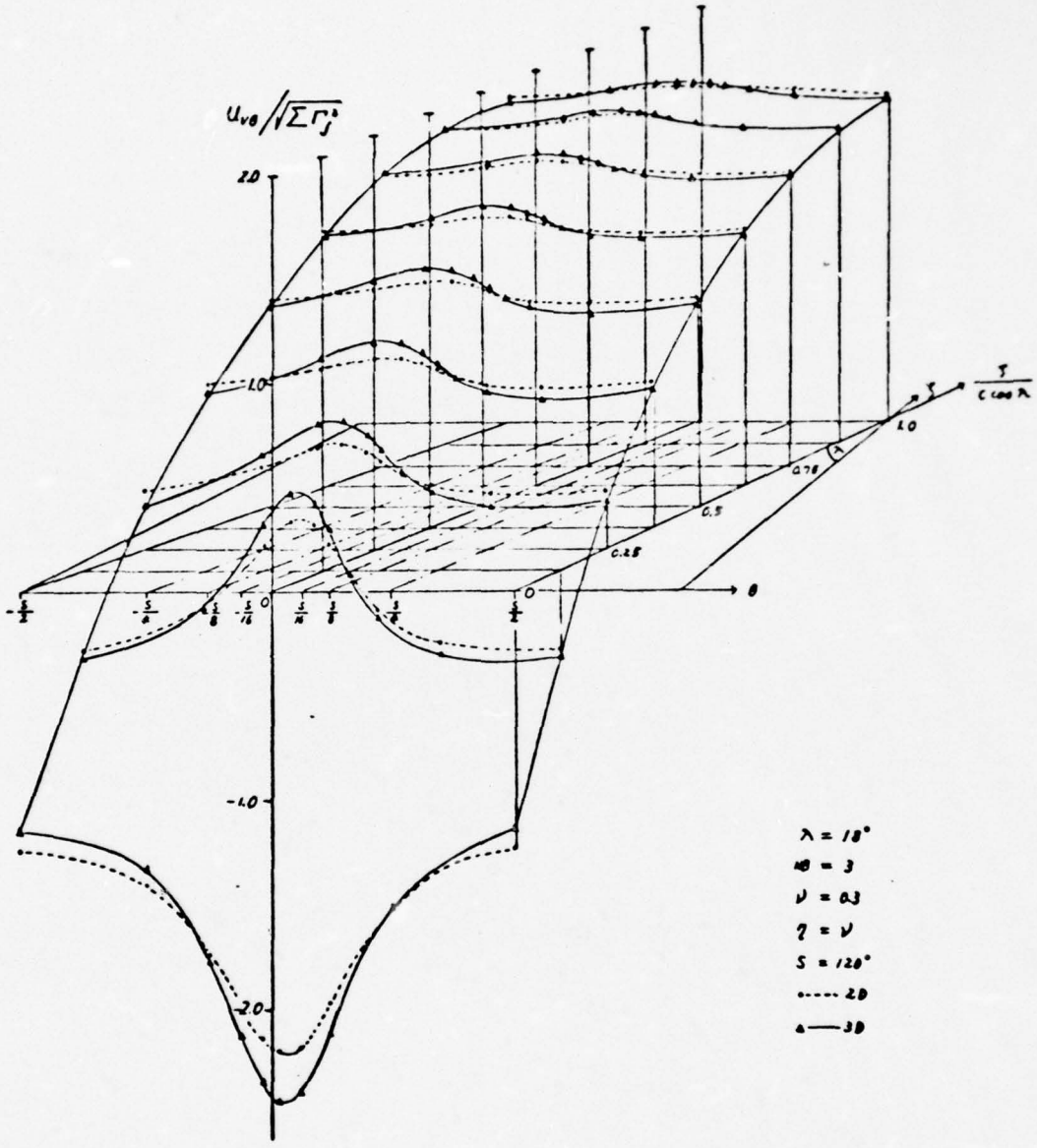


Fig.54: Distribution of the Tangential Velocities at the Hub induced by NB Series of Radial Vortex Lines of JVS=8 for $\lambda$ =18°, NB=3 and $\nu$ =0.3

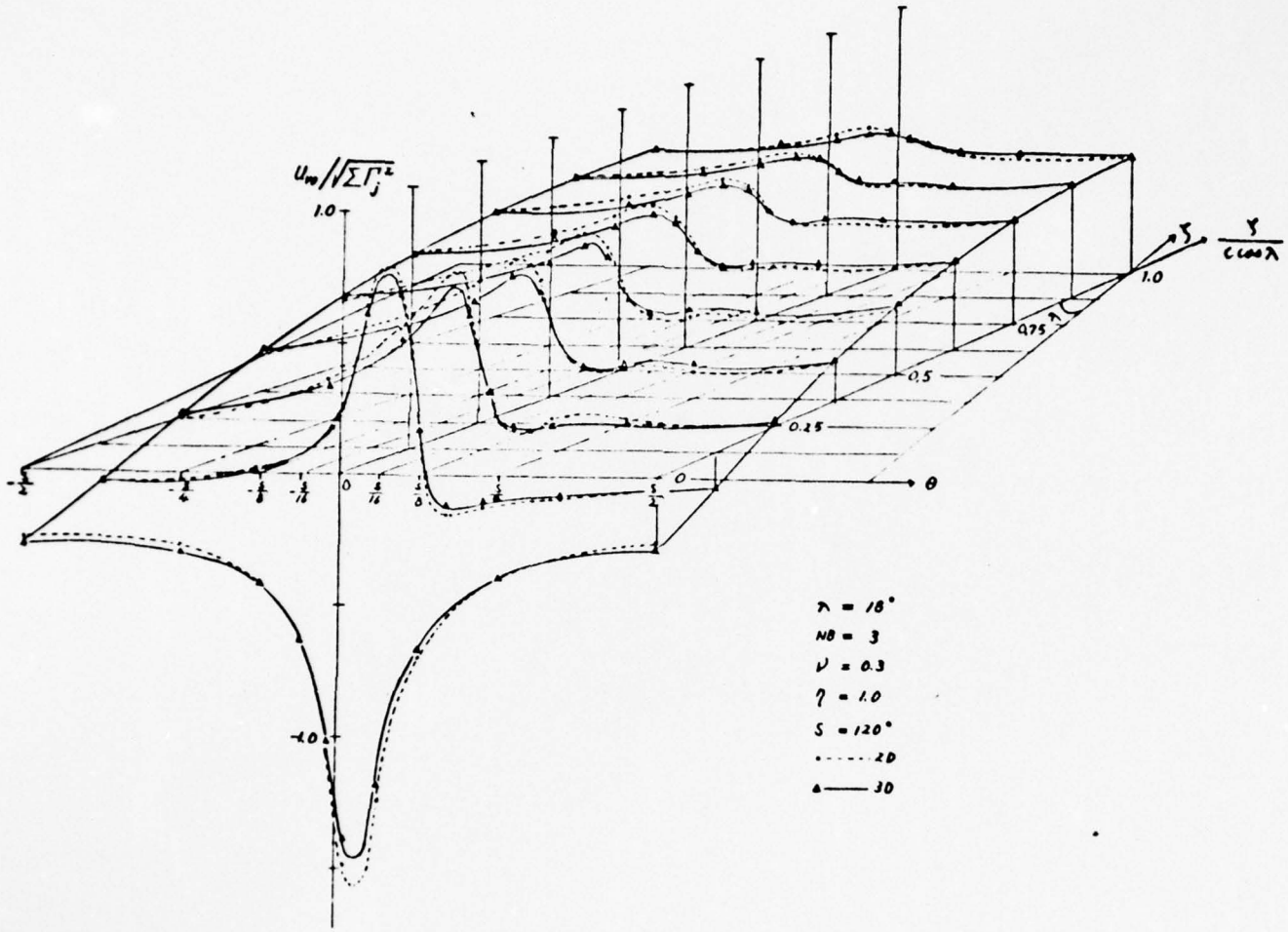


Fig.55: Distribution of the Tangential Velocities at the Tip induced by NB Series of Radial Vortex Lines of JVS=8 for $\lambda$=18°, NB=3 and $\nu$=0.3

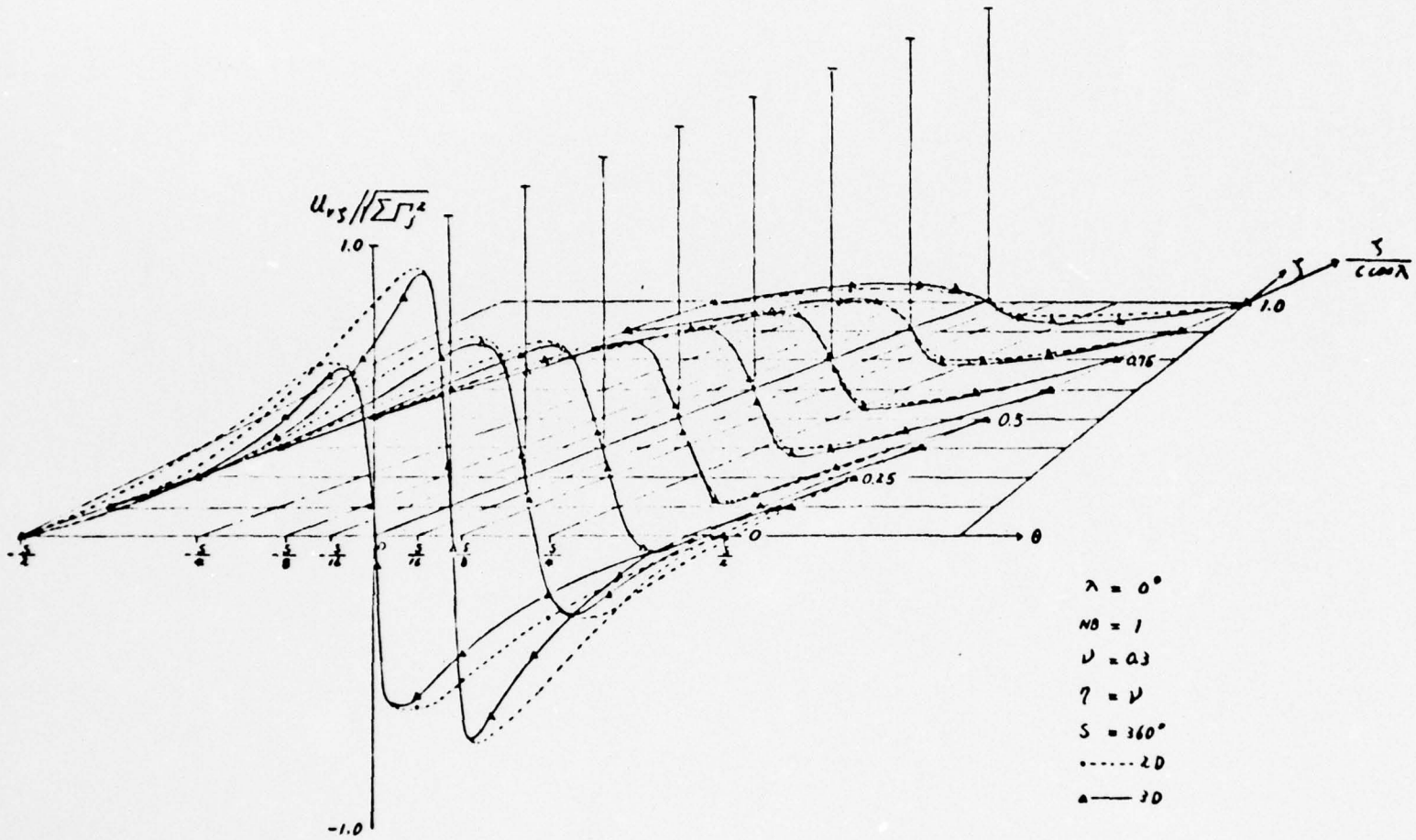


Fig.56: Distribution of the Axial Velocities at the Hub induced by NB Series of Radial Vortex Lines of JVS=8 for $\lambda = 0°$, NB=1 and $\nu = 0.3$

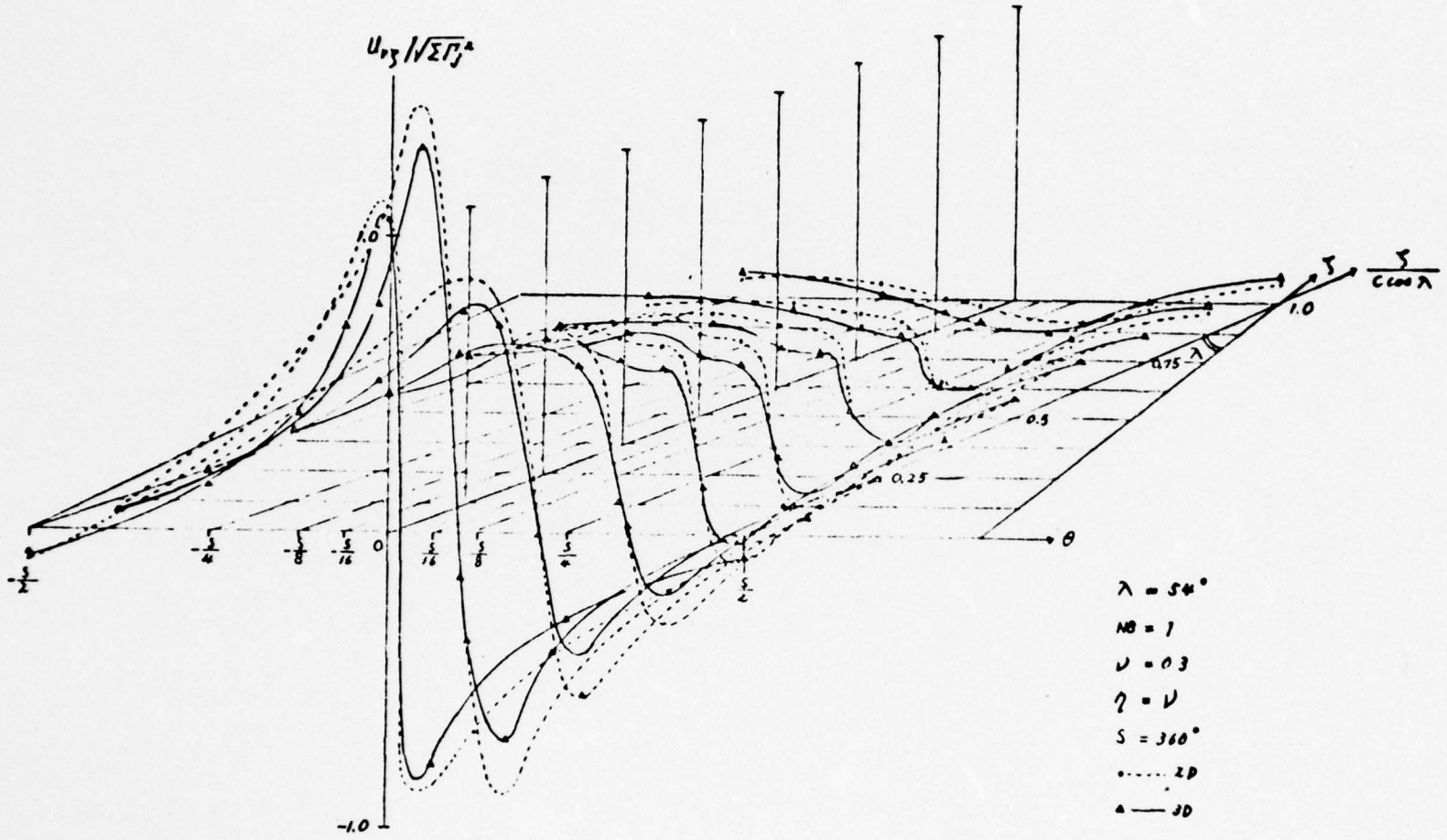


Fig.57: Distribution of the Axial Velocities at the Hub induced by NB Series of Radial Vortex Lines of JVS=8 for $\lambda=54°$, NB=1 and $\nu=0.3$

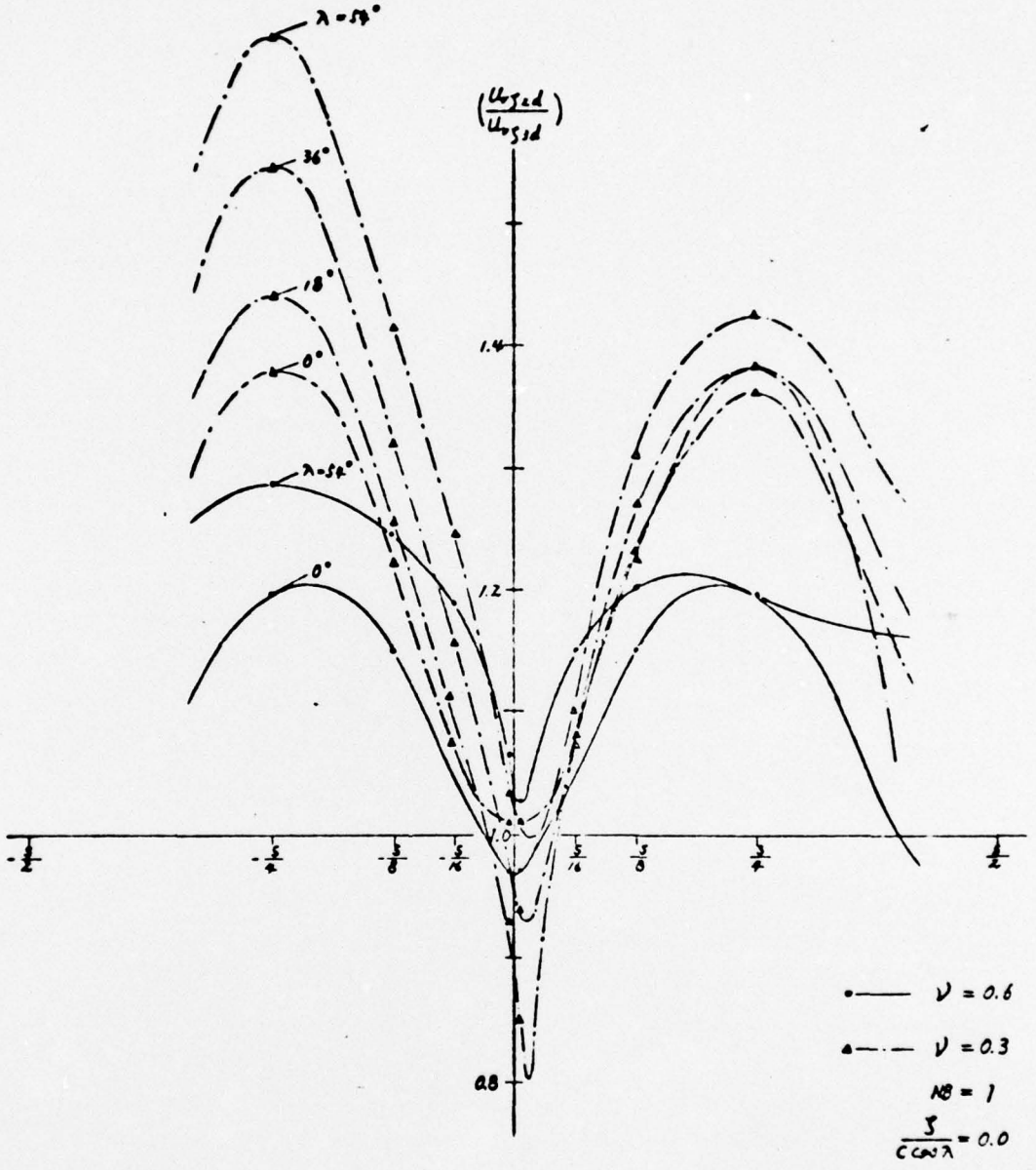


Fig.58: Ratio of the Axial Velocities at the Hub induced by NB Series of Radial Vortex Lines of JVS=8 for NB=1 at $J/c\cos\lambda = 0.0$

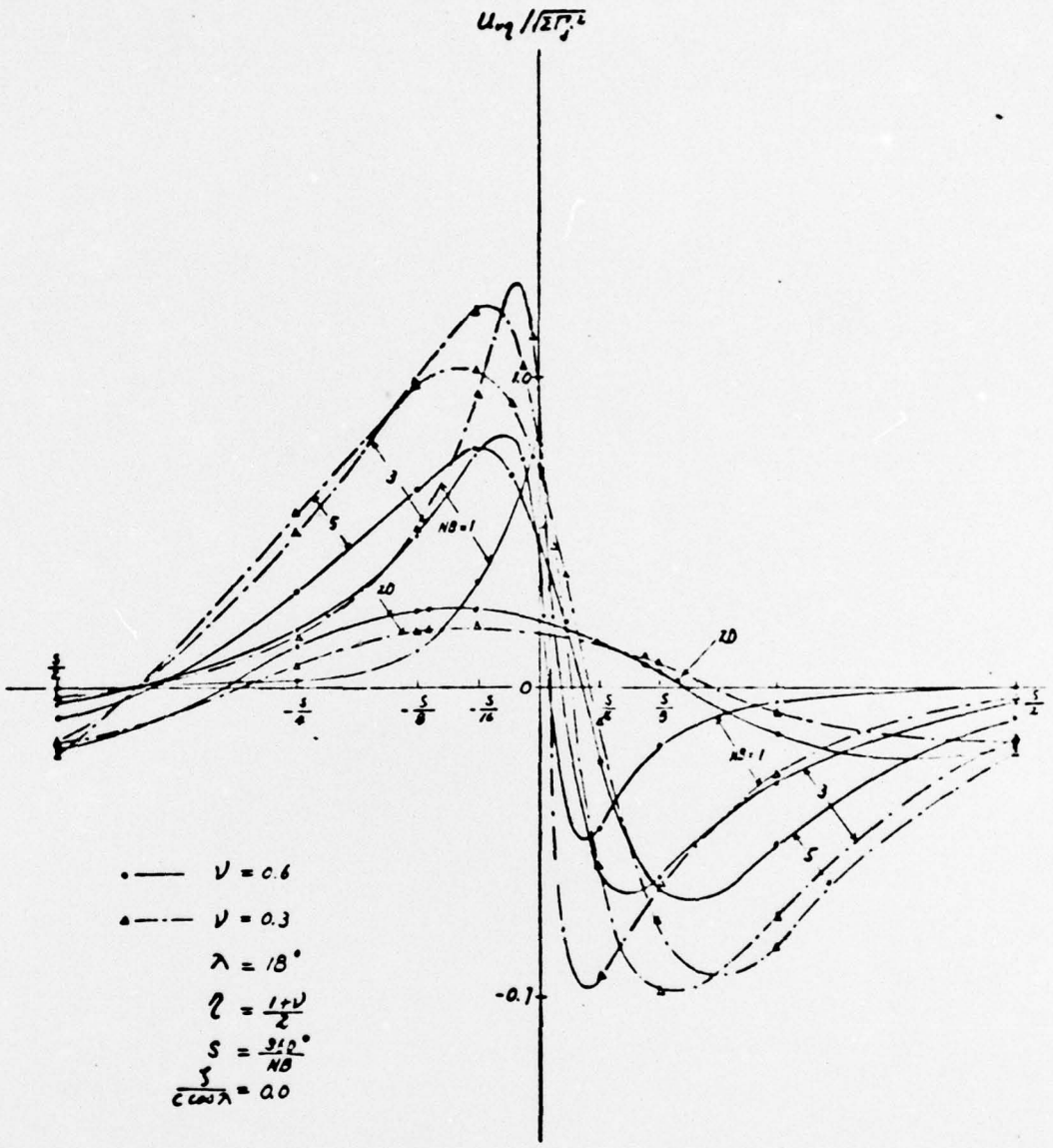


Fig.59: Distribution of the Radial Velocities at the Mid Radius Induced by NB Series of Radial Vortex Lines of JVS=8 for $\lambda$=18° at $\zeta/c\cos\lambda$ =0.0

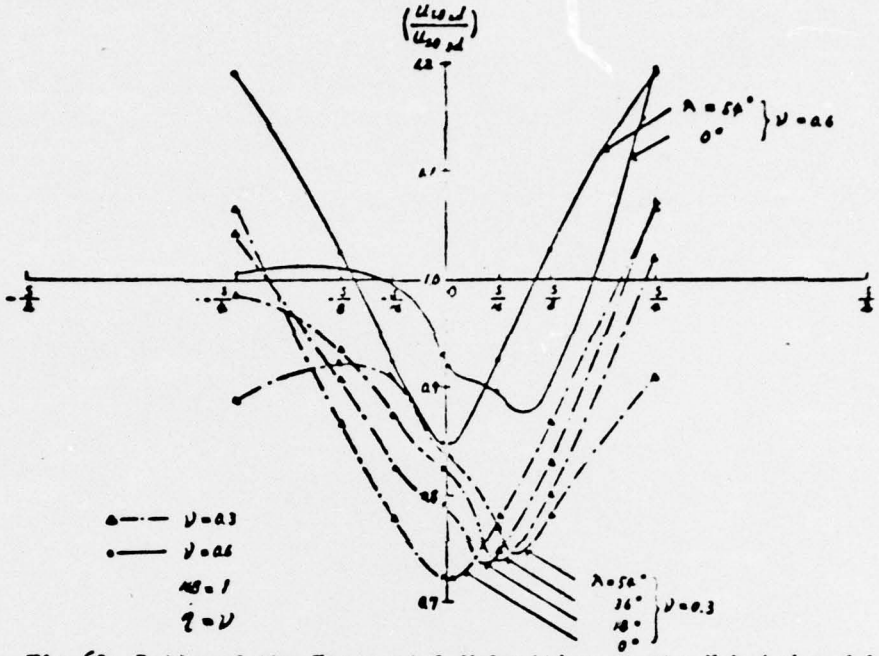

Fig.60: Ratio of the Tangential Velocities at the Hub induced by NB Series of Radial Source Lines of JVS=8 for NB=1 at $y/c\cos\lambda=0.0$

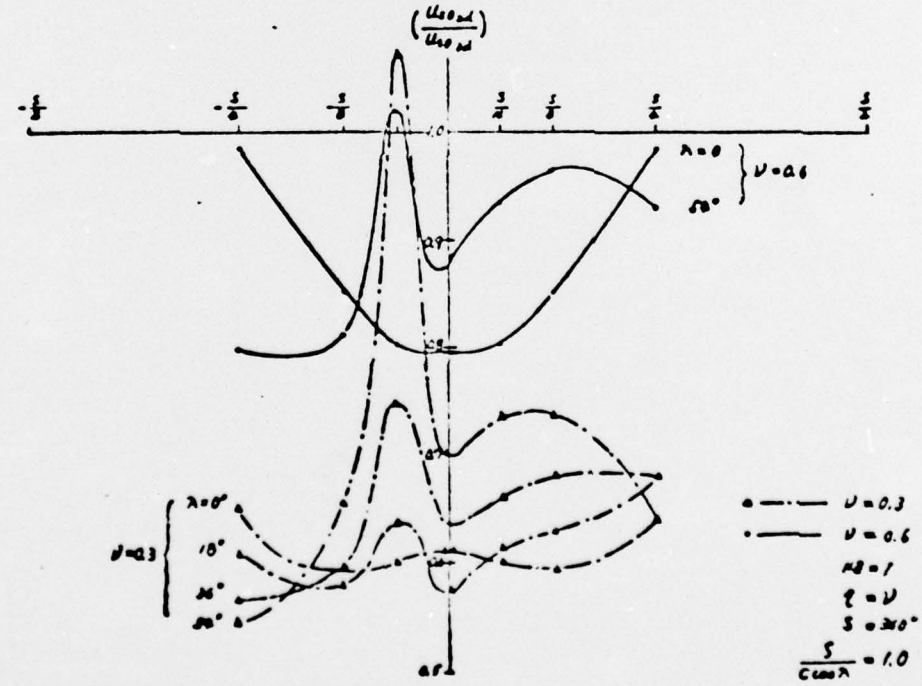

Fig.61: Ratio of the Tangential Velocities at the Hub induced by NB Series of Radial Source Lines of JVS=8 for NB=1 at $y/c\cos\lambda=1.0$

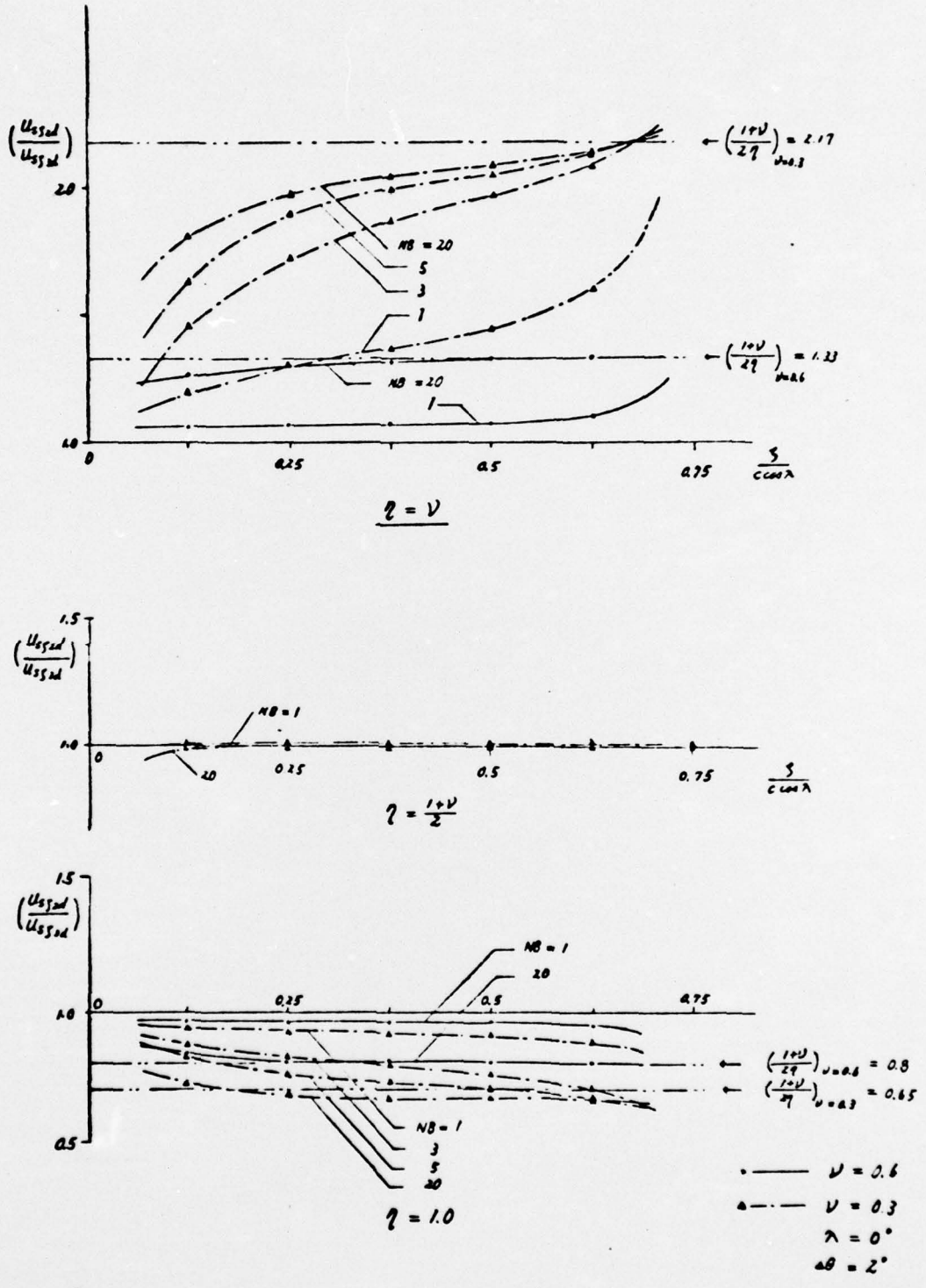


Fig.62: Ratio of the Axial Velocities induced by NB Series of Radial Source Lines of JVS=8 for $\lambda=0°$ at $\Delta\theta=2°$, $\eta=\nu$, $\frac{1+\nu}{2}$ and 1.0

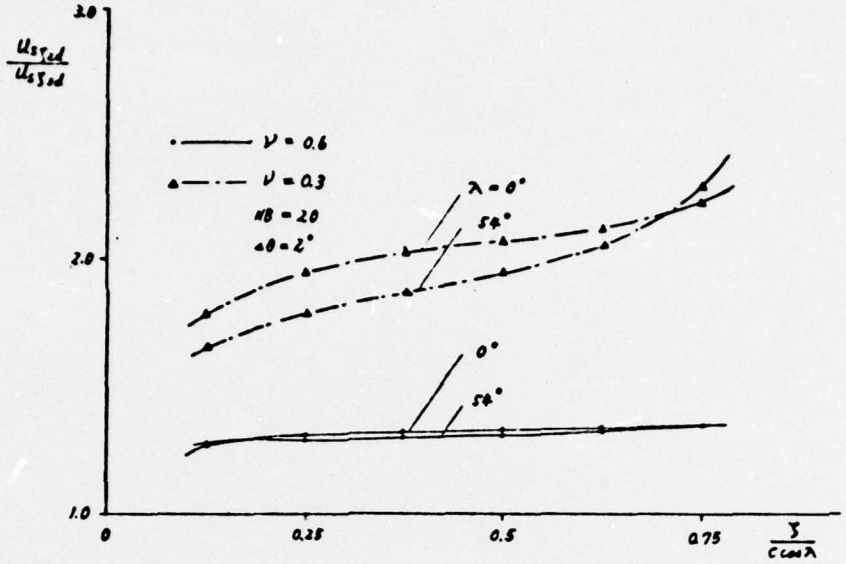


Fig.63: Ratio of the Axial Velocities at the Hub induced by NB Series of Radial Source Lines of JVS=8 for NB=20 at $\Delta\theta = 2^\circ$

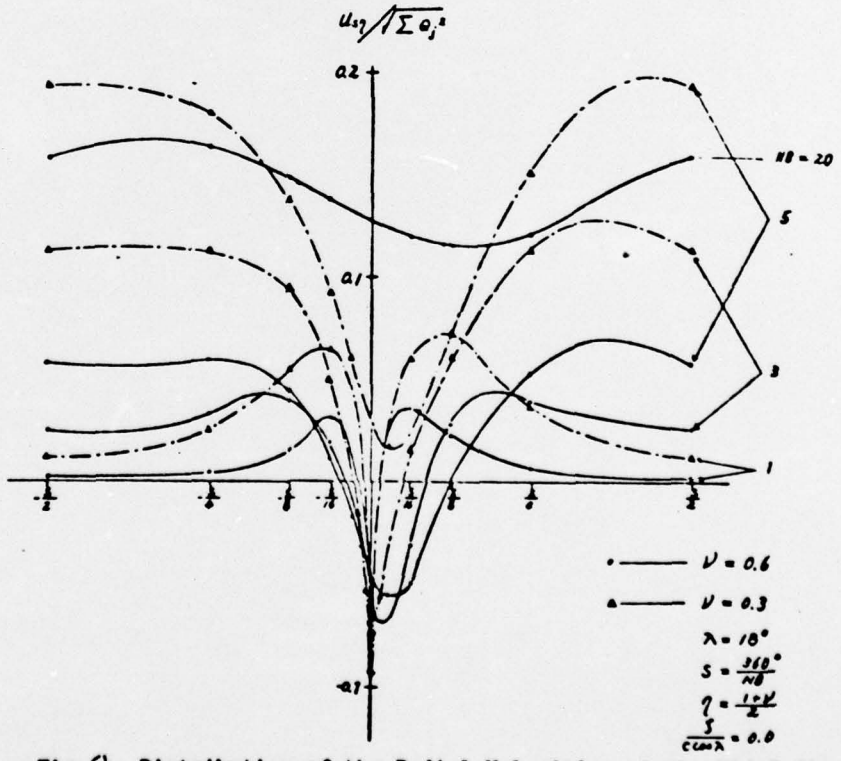


Fig.64: Distribution of the Radial Velocities at the Mid Radius induced by NB Series of Radial Source Lines of JVS=8 for $\lambda=18^\circ$ at $y/c\cos\lambda=0.0$

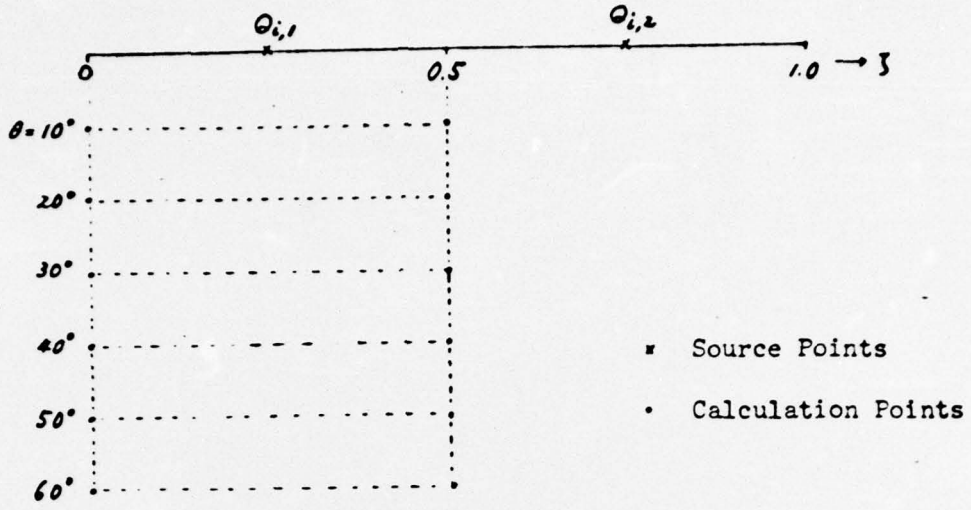


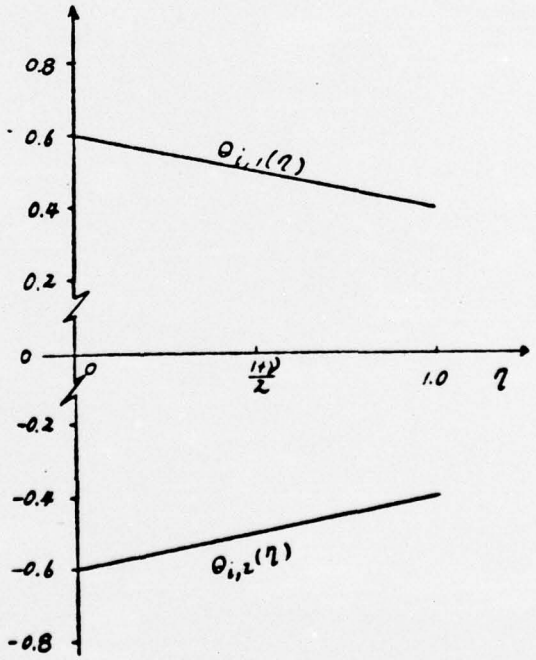


Figure 65 : Distribution of the Source of Variable Strength and Coordinate of the Singular Points and Calculation Points

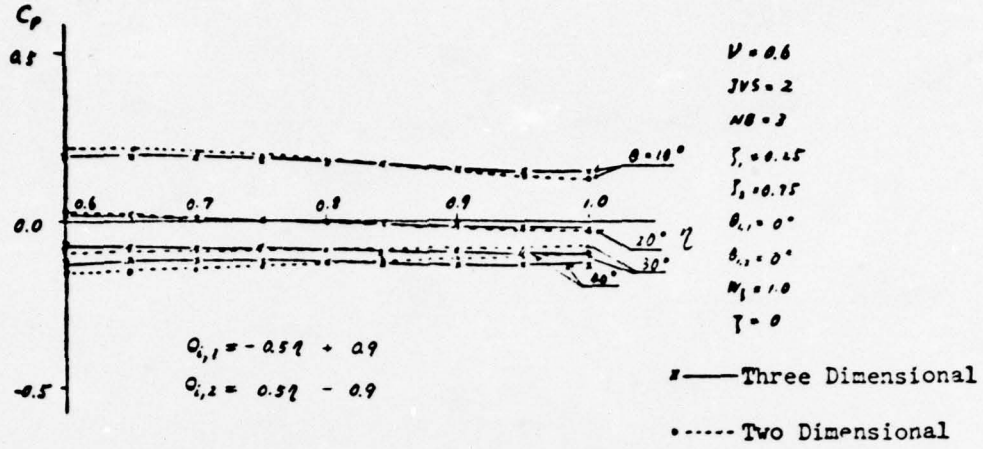


Figure66 : Pressure Distribution due to Source Lines of Variable Strength at $\zeta$=0 for NB=3 and $\nu$=0.6

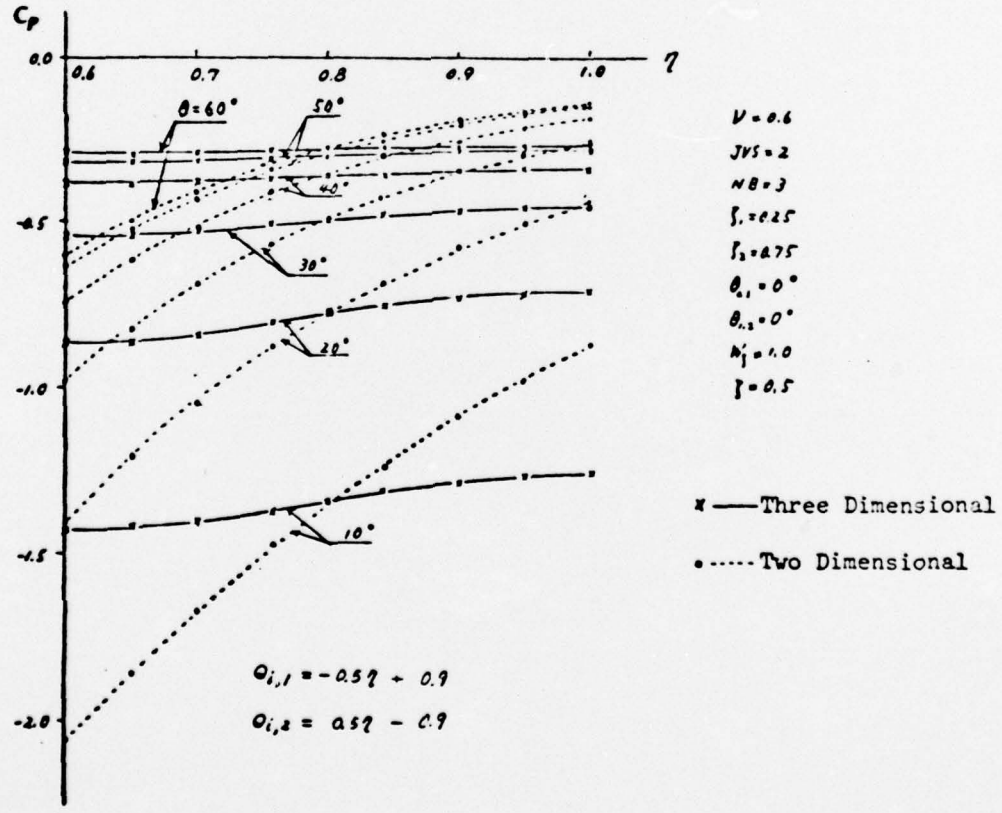


Figure67 : Pressure Distribution due to Source Lines of Variable Strength at $\zeta$=0.5 for NB=3 and $\nu$=0.6

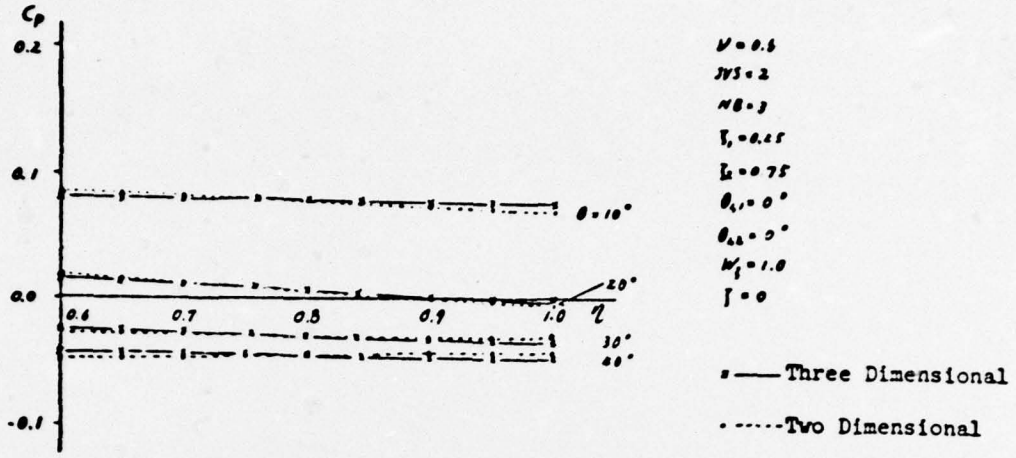


Fig.68: Pressure Distribution due to Source Line of Constant Strength $Q_{i,1}=0.2$, $Q_{i,2}=-0.2$

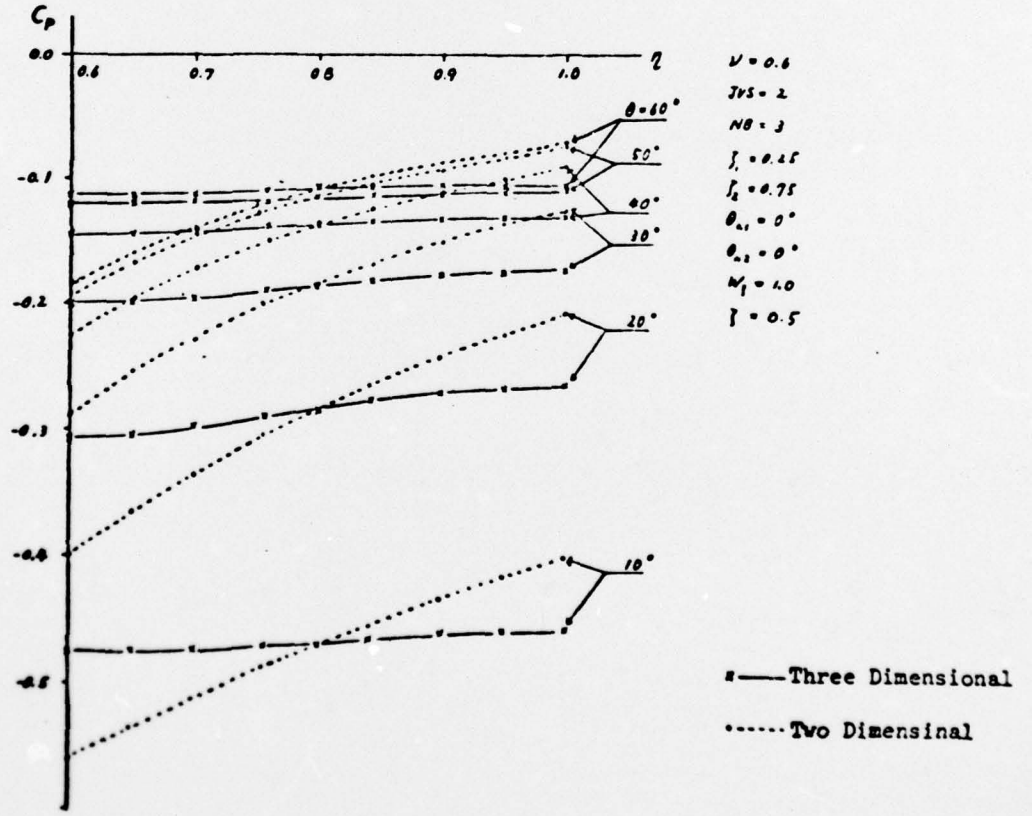


Figure 69 : Pressure Distribution due to Source Line of Constant Strength $Q_{i,1} = 0.2$, $Q_{i,2} = -0.2$ at $\gamma = 0.5$ for NB = 3, $\nu = 0.6$

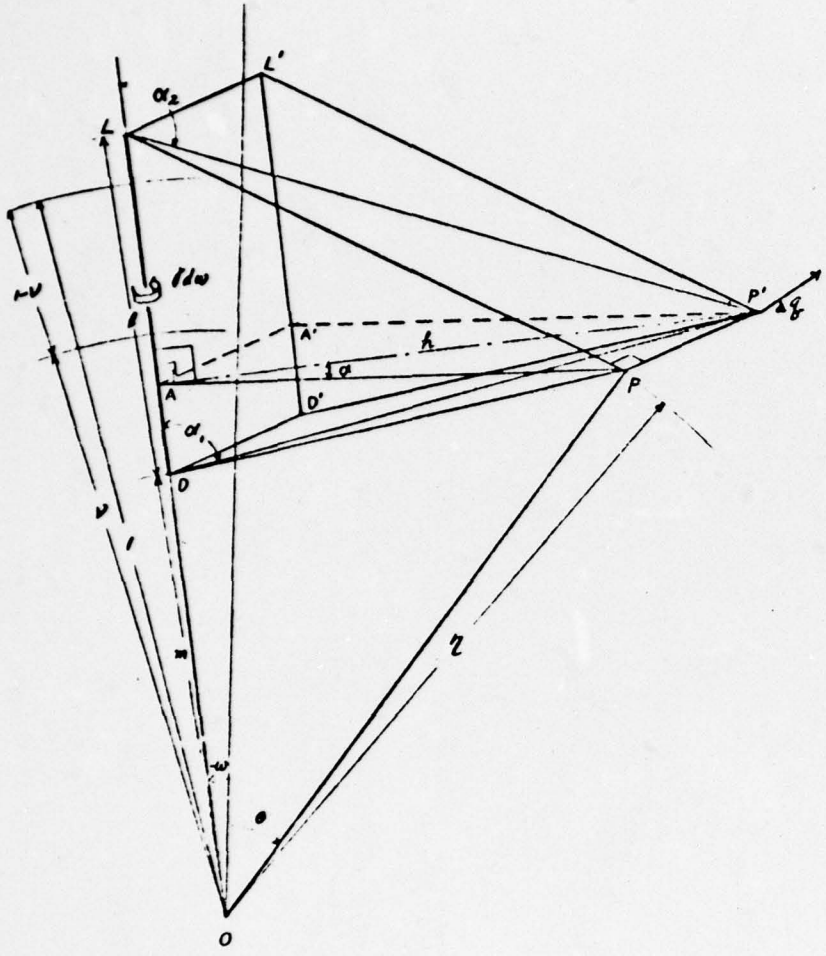


Fig.70: Split Radial Vortex Line

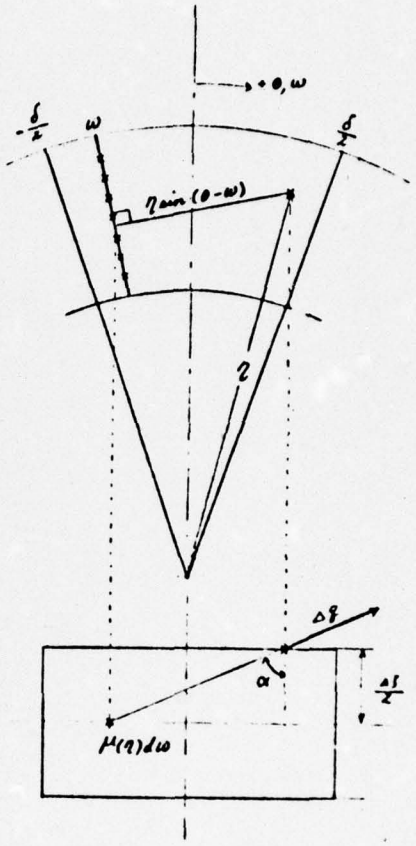


Fig.71: Split Radial Source Line

UNCLASSIFIED
Security Classification

## DOCUMENT CONTROL DATA - R & D

*(Security classification of title, body of abstract and indexing annotation must be entered when the overall report is classified)*

| 1. ORIGINATING ACTIVITY (Corporate author) | 2a. REPORT SECURITY CLASSIFICATION |
|---|---|
| Applied Research Laboratory<br>University Park, Pennsylvania | Unclassified |
| | 2b. GROUP |

3. REPORT TITLE

Three Dimensional Inviscid Effects and Limitations of Cascade Theory in Axial Flow Turbomachinery

4. DESCRIPTIVE NOTES (Type of report and inclusive dates)

M.S. Thesis, Aerospace Engineering, June 1974

5. AUTHOR(S) (First name, middle initial, last name)

A. Tamura

| 6. REPORT DATE | 7a. TOTAL NO. OF PAGES | 7b. NO. OF REFS |
|---|---|---|
| April 18, 1974 | 148 pages | 9 |

| 8a. CONTRACT OR GRANT NO. | 9a. ORIGINATOR'S REPORT NUMBER(S) |
|---|---|
| N00017-73-C-1418 | TM 74-78 |
| b. PROJECT NO. | |
| c. | 9b. OTHER REPORT NO(S) (Any other numbers that may be assigned this report) |
| d. | |

10. DISTRIBUTION STATEMENT

Approved for Public Release. Distribution unlimited.
Per NAVORD - January 30, 1974

| 11. SUPPLEMENTARY NOTES | 12. SPONSORING MILITARY ACTIVITY |
|---|---|
| | Naval Ordnance Systems Command<br>Department of the Navy |

13. ABSTRACT The general objective of the investigation reported in this thesis is to obtain a reliable understanding of the three dimensional potential flow through axial flow turbomachinery. The calculation of the three dimensional potential flow through an impeller is based on the method of distributed singularities. The blades are replaced by a series of line vortices and line sources which have their axes along the radial direction and are arranged along the blade camber surface. The basic perturbed velocity fields due to a single radial vortex line of constant strength and a single radial source line of variable strength along the radial direction are computed from a modified theory based on Tyson's and Rossow's formulation. Since the resultant perturbed flow fields are solutions of the linear Laplace equation and the boundary conditions are homogeneous, these solutions may be superimposed for a series of radial vortex lines and source lines located at arbitrary points. Eigen values and related functions are calculated for Bessel function of order m = 0 to 100, number of eigen values for each order of Bessel function n - 20, hub-to-tip ratio $\nu$ = 0.3, 0.6. A computer program to obtain the three dimensional flow field in a turbomachinery with arbitrary number of blades, number of singular points per blade, and singular points locations was developed. Examples illustrating the interference effects due to hub-to-tip ratio, stagger angle, numbers of the blades were carried out. The effects of the radial variation of the strength of the radial source line were examined. The three dimensional effects are found to be appreciable for low hub tip configuration with fewer number of blades.

DD FORM 1 NOV 65 1473 (PAGE 1) PLATE NO. 21856

S/N 0102-014-6600

UNCLASSIFIED
Security Classification

| 14. KEY WORDS | LINK A | | LINK B | | LINK C | |
|---|---|---|---|---|---|---|
| | ROLE | WT | ROLE | WT | ROLE | WT |
| AXIAL FLOW | 8 | | | | | |
| CASCADE THEORY | 8 | | | | | |
| EIGENVALUES | 8 | | | | | |
| INTERFERENCE EFFECTS | 8 | | | | | |
| INVISCID EFFECTS | 8 | | | | | |
| POTENTIAL FLOW | 8 | | | | | |
| TURBOMACHINERY | 8 | | | | | |

DISTRIBUTION LIST

Commander (ORD 632)
Naval Ordnance Systems Command
Department of the Navy
Washington, D.C. 20360 — Copies 1 and 2

Commander (ORD 34B)
Naval Ordnance Systems Command
Department of the Navy
Washington, D.C. 20360 — Copies 3 and 4

Defense Documentation Center
5010 Duke Street
Cameron Station
Alexandria, Virginia 22314 — Copies 5 through 16

Via: Commander (ORD 632)
Naval Ordnance Systems Command
Department of the Navy
Washington, D.C. 20360